Sources of spatial tuning in the dorsal subiculum

Dissertation

zur

Erlangung des Doktorgrades (Dr. rer. nat.)

der

Mathematisch-Naturwissenschaftlichen Fakultät

der

Rheinischen Friedrich-Wilhelms-Universität Bonn

vorgelegt von:

Dennis Dalügge

aus

Neuss

Bonn 2024

Angefertigt mit Genehmigung der Mathematisch-Naturwissenschaftlichen Fakultät

der Rheinischen Friedrich-Wilhelms-Universität Bonn

Gutachter/Betreuer: Prof. Dr. Martin Fuhrmann

Gutachter: Prof. Dr. Walter Witke

Tag der Promotion: 03.09.2024

Erscheinungsjahr: 2024

für Maribel, Klara, Cornelia und Martin

Contents

List of figures

Abstract

Spatial navigation is an essential behavior for all moving life-forms. A main mammalian brain structure implicated in this process is the hippocampal formation. Neuronal firing patterns in this brain region are remarkably correlated to various aspects of the animal's location and navigation. The subiculum is a primary output structure of hippocampal information processing, providing output to various cortical and subcortical areas. With this crucial position within the hippocampal formation, the primary role of the subiculum is to integrate, compress and then distribute hippocampally-processed information to the whole brain. Two major inputs to the subiculum arise from the CA1 region and the entorhinal cortex. This study investigates the individual roles of these two input streams in generating spatially correlated firing of subicular neurons.

In vivo whole cell patch clamp recordings in mice running freely on a circular track revealed that dorsal subicular neurons receive spatially tuned input. Additionally, channelrodopsin assisted circuit mapping showed, that the two major input streams target specific regions in the dendritic tree of dorsal subicular neurons. Specifically, CA1 input is located more proximal, while EC input forms synapses in the distal part of the dendritic tree of dorsal subicular neurons. Finally, individual contributions of both input streams on the spatial tuning of dorsal subicular neurons were investigated using two-photon calcium imaging in mice running on a linear treadmill. Chemogenetic inactivation of either CA1 or entorhinal cortex inputs via viral transduction of the inhibitory DREADD and local application of CNO by a small hole in the imaging window, revealed district contributions of both inputs paths: CA1 inputs are necessary for the place and velocity tuning, while EC inputs are only necessary for the place tuning of dorsal subicular neurons.

Taken together my experiments demonstrate that (I) subicular neurons receive spatial and velocity tuned input (II), that subicular neurons maintain a functional input segregation between CA1 and entorhinal cortex synapses and (III) that both input streams play differential roles in shaping the spatial tunings of subicular neurons with respect to place and movement speed. This study emphasizes the need to differentiate between the information that one brain region could potentially receive from other brain regions and the information that is actually used by the postsynaptic neuron during their input-output transformation.

1. Introduction

Spatial navigation is an essential behavior of all moving animals. One of the brain regions heavily involved in spatial navigation in mammals is the hippocampal formation. The main output region of the hippocampus is the subiculum (SUB), which distributes information to many regions of the brain. This work aims to elucidate how subicular neurons integrate hippocampally processed, spatially tuned input to generate spatially tuned output that transmits navigation- relevant information to the rest of the brain.

1.1. Spatial navigation and the hippocampal formation

In contrast to stationary organisms, spatial navigation in an environment that is constantly changing is a crucial behavior for all mobile organisms. Animals navigate to acquire food, shelter, or mating opportunities, thus imposing an evolutionary pressure to self-navigate efficiently. The information animals can use for spatial navigation may come either from the external world or from the internal state of the animal. Navigation based on external cues is called allocentric navigation, whereas spatial navigation based on internal information (e.g. distance traveled) is called egocentric navigation. One fundamental problem in neuroscience is to decrypt how the brain generates, stores, and uses internal maps of the external world for spatial navigation. The hippocampal formation is the primary brain structure associated with this process in mammals (O'Keefe and Nadel, 1978). Specifically, the dorsal region of the hippocampal formation is responsible for spatial navigation and memory, while the ventral part is associated to stress, emotions, and affect (Fanselow and Dong, 2010; O'Mara et al., 2001; Strange et al., 2014) (Figure 1).

The hippocampal formation comprises numerous interconnected sub-regions in a sequential pattern (Amaral and Witter, 1989; O'Mara, 2005; O'Mara et al., 2001) (Figure 2 B). These sub-regions include the entorhinal cortex (EC), the dentate gyrus (DG), the cornu ammonis (CA) regions CA3, CA1 and the SUB. While all these regions belong the hippcampal formation, only the DG and the CA regions form the 'hippocampus proper'. Information is conveyed from the superficial layers of the EC to the DG via the 'perforant path', which is then relayed to CA3 by DG neurons. CA3 forms efferent connections on

both the ipsilateral and contralateral CA1 regions, via Schaffer collaterals. Subsequently, CA1 neurons project to the superficial layers of the EC and to the SUB, thus completing the hippocampus-EC loop. Besides this predominantly unidirectional canonical information flow within the hippocampal formation, there are several non-canonical connectivity patterns. For instance, EC axons of the perforant path connect directly to CA3 neurons (Amaral and Witter, 1989). Furthermore, the EC projects directly to CA1 and to the SUB via the temporoammonic pathway (Witter et al., 1988). In addition to these direct projections, reciprocal connections have been described, such as CA3 to the DG (Scharfman, 2007), CA1 to CA3 (Lin et al., 2021), and SUB to CA1 (Sun et al., 2014) (Figure 2 B).

1.2. The subiculum - output region of the hippocampal formation

The SUB is the final region in the sequential connectivity of the hippocampus. As a result, it serves as the ultimate hub for hippocampal information processing and has widespread efferent projections to targets both nearby and far-reaching throughout the brain (Figure 1). Nearby, the SUB connects to deep layers of the EC. Moreover, subicular information reaches the superficial layers of EC di-synaptically via the parasubiculum and presubiculum (Amaral and Witter, 1989), which completes the hippocampal-EC loop and adds to the CA1-EC connectivity. Furthermore, the SUB projects to various cortical and subcortical regions that have highly diverse functions. Notably, there is a differentiation of SUB projection targets that involves a dorso-ventral as well as a proximo-distal axis of the SUB (O'Mara, 2005; O'Mara et al., 2009; Cembrowski et al., 2018a). Ventral SUB targets brain nuclei mostly in the hypothalamic region and the amygdala, which suggests participation in stress and fear responses (O'Mara, 2005; Witter, 2006). In contrast, the dorsal subicular (SUB) efferent projections are involved in spatial navigation and memory. These efferent connections appear to be related to the proximo-distal axis (adjacent to CA1 and presubiculum, respectively) of the SUB (Witter, 2006). The proximal SUB projects to the prelimbic, infralimbic, orbitofrontal, and perirhinal cortex. Subcortical targets such as the nucleus accumbens, lateral septum, the mamillary bodies and amygdala (Namura et al., 1994; Ding, 2013;

Witter, 2006) suggest an involvement in memory processes. In contrast, the distal SUB transmits efferences to brain regions involved in spatial navigation, including the retrosplenial cortex, presubiculum, and postrhinal cortex (Witter, 2006). The middle section of the SUB projects primarily towards the medial mammillary nucleus, nucleus reunions, and the anterior thalamic nuclei (Naber and Witter, 1998; Wright et al., 2010).

These data demonstrate that the SUB projects to a vast variety of brain areas (Figure 1). Although there are some collateral axons within these projections (Kinnavane et al., 2018; Qiu et al., 2024), the vast majority of individual subicular neurons target only one specific brain area (Naber and Witter, 1998; Namura et al., 1994; Wright et al., 2010). As a result, the SUB forms distinct parallel output pathways from the hippocampal formation to many regions of the brain. On a functional level, these parallel output pathways can be activated synchronously or asynchronously. Synchronous subicular activity can arise, for example, during hippocampal sharp wave ripples. These ripples are an oscillatory pattern generated by the hippocampal formation and are classically linked to memory consolidation and memory recall. Synchronous activity in the SUB can potentially organize brain-wide activity (Logothetis et al., 2012) but is also thought to be involved in the spread and generalization of hippocampal seizures (Engel, 2001; Stafstrom, 2005; Fei et al., 2022). In contrast, during active exploration of the animal, subicular activity is asynchronous and the different output routes of the SUB are information specific (Kitanishi et al., 2021). Different brain regions receive distinct information about the animal’s spatial navigation from the SUB (Kitanishi et al., 2021). Thus, with its numerous parallel output pathways, the SUB actively distributes distinct hippocampally processed information to specific brain regions.

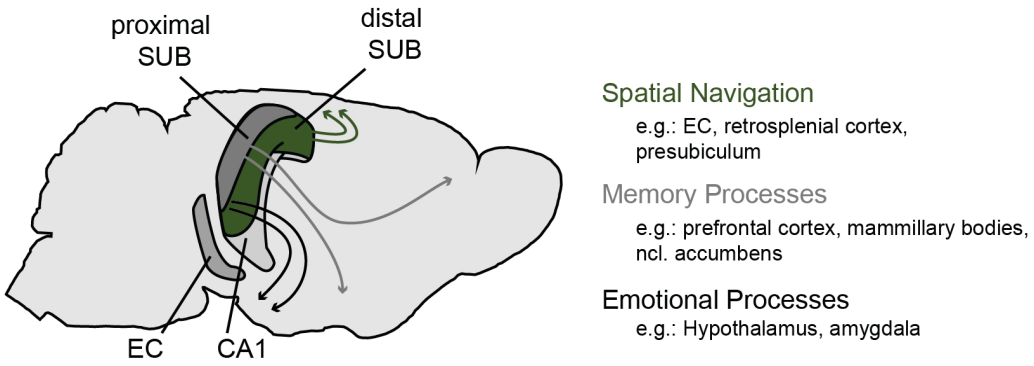

Figure 1: Parallel output routes from the subiculum

The SUB can be divided into a dorsal-ventral and a proximo-distal axis. Interestingly, these different parts of the SUB project to different brain regions. The axons of the ventral SUB form efferent connections to hypothalamic regions (black arrows). The proximal part of the dorsal SUB projects to the frontal cortex and subcortical structures involved in memory (grey arrows). The distal-dorsal SUB projects to brain areas participating in spatial navigation (green arrows). The majority of individual subicular long-range projections target only one specific brain area. Thus, the SUB forms parallel output pathways for hippocampally processed information.

1.2.1. The SUB in spatial navigation

Research has identified specific roles of individual hippocampal subfields in spatial navigation and memory, including those of the SUB (Eichenbaum et al., 1999; Moser et al., 2008; Brandon et al., 2014). The earliest evidence for the involvement of the SUB in spatial navigation and memory comes from lesion studies. These studies examined the animal's performance in the Morris Water Maze. For this test, mice have to find a hidden platform while they are swimming in a large circular pool. These experiments indicated that the SUB is involved in allocentric spatial learning (Morris et al., 1990), spatial memory (Galani et al., 1998), and the integration of geometric information during spatial navigation (Oswald and Good, 2000). Another set of studies examined the animal's radial-arm maze task performance. During testing, it was found that subicular lesions only affected the animals' efficiency in the dark when they could not detect visual landmarks, suggesting the involvement of the SUB in egocentric spatial navigation (Potvin et al., 2010). In the light, animals with subicular lesions were able to use visual cues in the radial-arm maze for spatial navigation. Nonetheless, they faced impairment when visual cues overlapped, supporting the idea that the SUB is involved in visual

pattern separation (Potvin et al., 2009).

Recently, a study using an optogenetic approach revealed a critical role of the dorsal SUB in memory retrieval and its contribution to context-dependent memory updating (Roy et al., 2017). Moreover, earlier findings that dorsal SUB is required for allocentric spatial learning, and the encoding of new spatial working memories were confirmed using chemogenetic silencing of the distal dorsal SUB (Cembrowski et al., 2018a): In these experiments proximal and distal dorsal subicular neurons were distinguished by their differential expression of the genes for Nts and Klk8. Using mouse-lines for these markers and viral transduction, selective expression of the inhibitory designer receptor exclusively activated by designer drugs (DREADD) in either proximal or distal SUB was achieved. Animals' spatial working memory was tested in the Morris Water Maze. Systemic application of the DREADD agonist clozapine-N-oxide (CNO) decreased the activity in the infected brain region. Only the reduction in the activity of distal dorsal subicular neurons had an effect on the animal's performance in the working memory task.

1.2.2. Microstructure and cell types of the SUB

From an evolutionary perspective, the hippocampus belongs to the 'archicortex' and consists of three layers: the stratum moleculare, the stratum pyramidale, and the polymorphic layer (Witter and Groenewegen, 1990; O'Mara et al., 2001; Witter and Amaral, 2004). When compared to the neighboring CA1 region, the stratum pyramidale in the SUB is larger and has looser cell packing. The large bodies of the subicular pyramidal neurons extend their top dendrites into the molecular layer and their bottom dendrites into the deeper sections of the pyramidal cell layer. Furthermore, in CA1, the stratum moleculare splits into the stratum radiatum and stratum lacunosum moleculare, which also functionally separates axons of CA3 in the stratum radiatum and axons of EC in the stratum lacunosum moleculare. This histological separation is lost in the SUB (Witter and Groenewegen, 1990; Bienkowski et al., 2018) (Figure 2).

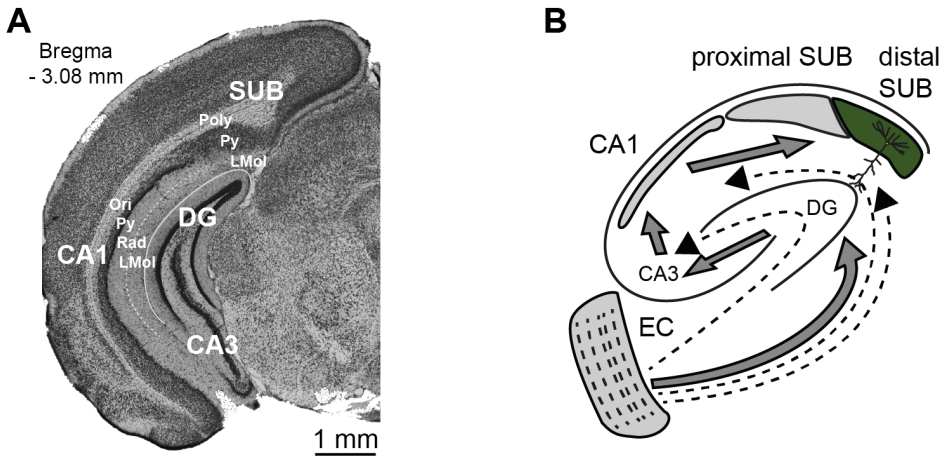

Figure 2: Subicular microstructure and information flow

A: Nissl staining of a coronal slices -3.08 mm caudal from Bregma (adapted from Franklin and Paxinos 2008) showing the different layering of hippocampal subregions. Abbreviations: Ori: stratum oriens, Py: stratum pyramidale, Rad: stratum radiatum, LMol: stratum lacunosum moleculare, Poly: polymorphic layer. Note that the division of stratum radiatum and stratum lacunosum moelculare is missing in the SUB. B: Information flow in the hippocampal formation. EC axons of the perforant path project to the DG starting the trisynaptic loop of DG -> CA3 -> CA1 that ends with the efferent connection from CA1 to the SUB (grey arrows). In addition, EC projects monosynaptically to all subregions of the hippocampal formation (black arrows).

The internal structure of the SUB is presently being evaluated. Accumulating evidence divides the SUB into a proximal (adjacent to CA1) and a distal (adjacent to presubiculum) part. This partition is primarily based on electrophysiological and gene-expression profiles, as well as projection targets (see above): distal subicular neurons are more inclined to intrinsic bursting. Most of the distal subicular neurons tend to fire upon rheobase stimulation with multiple action potentials riding on a depolarization hump (Taube, 1993; Greene and Totterdell, 1997; Harris et al., 2001; Kim and Spruston, 2012; Cembrowski et al., 2018a). Additionally, Nts, VGlut2, Cdh7 Elfn1, and Scn4b are expressed in distal subicular neurons. In contrast, proximal subicular cells are more likely to fire single action potentials and express ZnT3, Nnat, Chrna7, Nptx1, and Robo1 (Ishihara and Fukuda, 2016; Cembrowski et al., 2018b; Bienkowski et al., 2018).

As explained earlier, bursting is linked to the anatomy of the SUB. Moreover, morphological properties differ between bursting and regular spiking subicular neurons. Bursting neurons possess sparsely distributed basal dendrites and densely packed tuft

dendrites, whereas the opposite is true for regular spiking neurons in the SUB (Graves et al., 2012). Remarkably, regular-spiking neurons project unidirectionally onto bursting neurons, and within one firing type, neuronal connections are sparse (Böhm et al., 2015). Finally, sharp wave ripples differentially recruit bursting and regular-spiking subicular neurons, indicating distinct roles in the subicular microcircuit (Böhm et al., 2015).

The differentiation of cell types along the proximo-distal axis and the region-specific targeting of different brain areas suggest that these two cell classes are involved in distinct output routes of the SUB. Therefore, it is likely that these two cell classes have different functions. Indeed, a recent optogenetic study targeting pyramidal neurons in the distal and proximal SUB found that encoding in a spatial working memory task requires only distal pyramidal neurons in the dorsal SUB (Cembrowski et al., 2018a).

1.3. Input-output transformation in neurons

Neurons are functionally polarized cells that receive inputs at their dendrites, integrate them at their soma, and transmit information through their axon. These cells can integrate tens of thousands of inputs, which consist of postsynaptic potentials (PSP) spreading via passive electro-tonic propagation along the dendritic membrane (Spruston et al., 1994). On their path towards the final integration point at the axon initial segment next to the neuron’s soma, PSPs undergo passive electrical attenuation and filtering. The attenuation can be as high as 40-fold in CA1 pyramidal neurons (Golding et al., 2005). Consequently, the influence of a single synaptic input on the somatic membrane potential is restricted (Williams and Stuart, 2002). However, multiple synaptic inputs that arrive coincidentally at the same location of a dendrite can accumulate. The combined PSPs experience attenuation and filtering as they travel towards the soma. Once at the soma, the PSPs from all the dendrites converge. When the membrane potential of the connected axon initial segment depolarizes beyond the action potential threshold, the neuron generates output in the form of action potential firing through its axon to transmit information to other neurons.

In recent years, it has become clear that many dendrites do not simply collect their synaptic input, but rather actively influence and shape their PSPs (Magee, 2000;

Larkum et al., 2009; Nusser, 2009; Branco and Häusser, 2010; Major et al., 2013). The dendritic membrane incorporates voltage-gated ion channels that either increase PSP amplitude (such as Ca^{2+} channels) or decrease PSP amplitude (such as Ih or K^{+}-channels (Magee, 2000)), effectively countering passive attenuation and filtering. Additionally, the accumulation of voltage-gated cation channels in dendritic "hot spots" results in dendritic spikes (Stuart and Spruston, 2015). Similar to action potentials, dendritic depolarization must exceed a threshold to effectively initiate dendritic spikes, thus creating a computational compartment within the preceding dendrites (Williams, 2004; London and Häusser, 2005).

One prominent example of dendritic spikes in the hippocampus is located in CA1 pyramidal neurons (Figure 3). These neurons have an accumulation of Ca^{2+} channels on their apical trunk that can initiate dendritic calcium spikes. This results in two computational dendritic compartments, namely the apical tuft as well as oblique and basal dendrites. Synapses from CA3 axons are located on the basal and oblique dendrites of CA1 pyramidal neurons, while EC synapses are found at the apical tuft (Golding et al., 1999; Takahashi and Magee, 2009). EC input alone can initiate calcium spikes in the apical trunk (Tsay et al., 2007). Consequently, in CA1 pyramidal neurons, EC input can be separately integrated from CA3 input. Nevertheless, calcium spikes elicited by EC synapses significantly reduce towards the soma, leading to unreliable action potential firing. Combining EC and CA3 input or EC input with back-propagating action potentials triggers a significant Ca^{2+} spike, leading to stable action potential output and local plasticity in the apical tuft (Bittner et al., 2017; Grienberger and Magee, 2022).

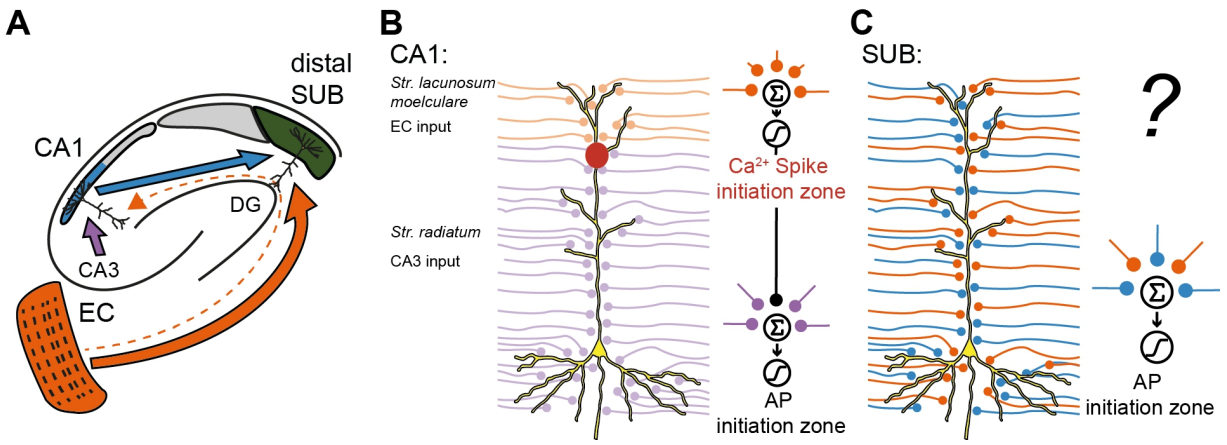

Figure 3: Input-output transformation in CA1 and SUB

A: Overview of hippocampal monosynaptic connections of CA1 and SUB: CA1 receives input from CA3 and EC whereas SUB neurons get their main hippocampal input from CA1 and EC. B: CA1 input is layered. EC synapses are located at the apical tuft and CA3 synapses are placed at the oblique and basal dendrites (left). Together with the dendritic threshold event at the Ca^{2+} spike initiation zone, EC inputs can be integrated separately from CA3 input leading to two integration compartments in the CA1 dendritic tree (right). Note that these compartments are not independent. For example, back-propagating action potentials potentiate dendritic Ca^{2+} spikes, leading to behavioral time-scale plasticity. C: Layering is absent in the SUB, suggesting that SUB dendritic trees form only one integration compartment.

One of the contributing factors to synaptic integration of various inputs is the compartmentalization of the postsynaptic neuron and the location of discerning synapses carrying specific information. As part of hippocampal information processing, subicular neurons primarily provide an accurate and noise-resistant representation of multiple spatial variables. Although much is known about synaptic integration in CA1 pyramidal neurons, it remains unclear how subicular neurons achieve their input-output transformation of spatial information (Figure 3).

1.3.1. Inputs to subicular pyramidal neurons

Subicular pyramidal neurons receive spatially tuned inputs from multiple sources, including the hippocampal formation, cortical and subcortical regions (O'Mara et al., 2001). The two main input pathways are CA1 and EC, which both converge on the same subicular cell (Cappaert et al., 2007; Gigg et al., 2000). These pathways contain distinct spatial information.

In fact, the SUB receives exceptionally dense projections from area CA1 of the hippocampus (Amaral et al., 1991; Cenquizca and Swanson, 2007; Jinno et al., 2007). This projection is topographically organized: Proximal CA1 (adjacent to CA3) projects to distal SUB, and distal CA1 fibers mainly connect to proximal subicular neurons (Amaral et al., 1991). The CA1 to SUB projection differs between bursting and regular spiking neuron (Behr et al., 2009): Low-frequency stimulation of CA1 input produces long-term depression (LTD) in bursting neurons, while low-frequency stimulation of CA1 fibers induces late-onset long-term potentiation (LTP) in regular spiking neurons (Fidzinski et al., 2008). High-frequency stimulation results in LTP of both subicular firing types (Wozny et al., 2008). The input from CA1 to SUB is mostly unidirectional (Gigg et al., 2000), with few reciprocal connections existing from SUB to CA1 (Commins et al., 2002).

Functionally, single CA1 pyramidal neurons are tuned to specific locations within their environment and fire when an animal is situated within one or a few of these corresponding place fields (O'Keefe and Dostrovsky, 1971). At the population level, the collection of place fields covers the entire environment of the animal, resulting in an internal representation of the animal's position (Eichenbaum et al., 1999). This representation is known to be highly dynamic. First, the place fields of CA1 undergo remapping in new environments on a rapid time scale (Muller and Kubie, 1987; Leutgeb et al., 2005). Second, while dorsal CA1 neurons encode spatial information (Leutgeb et al., 2005; Shan et al., 2016), they can be further adjusted to non-spatial features in the environment, such as odor (Taxidis et al., 2020), objects (Burke et al., 2011; Vandrey et al., 2021), direction (McNaughton et al., 1983; Navratilova et al., 2012), and reward (Gauthier and Tank, 2018). Third, the number of place fields for a particular location increases at the population level if it is relevant for the animal (Markus et al., 1995; Eichenbaum et al., 1999; Hollup et al., 2001; Dupret et al., 2010; Danielson et al., 2016). Therefore, place fields are not distributed equally throughout the animal's environment.

The SUB likely receives environmental information in the form of place fields from area CA1. Notably, neurons with the strongest spatial modulation were found primarily in the proximal regions of CA1 that project to the distal dorsal SUB (Henriksen et al., 2010). Additionally, CA1 neuron output is tuned to the animal's speed of locomotion (Geisler et

al., 2007; Góis and Tort, 2018; Iwase et al., 2020). Speed tuning may occur solely or together with place tuning in the same CA1 neuron.

The EC is responsible for the second major input to the SUB. The SUB can receive information from the EC either indirectly through the hippocampal trisynaptic loop or directly. The direct projection from EC to SUB is reciprocal and topographically organized (Naber et al., 2001; Kloosterman et al., 2003). More specifically, neurons in layer III of the EC are responsible for projecting to the SUB. In turn, the SUB primarily innervates the deep layers of the EC. Regarding the subicular proximo-distal axis, the lateral and medial ECs mainly project to the proximal and distal SUB, respectively (Witter et al., 2000). The direct projections from the EC to SUB are monosynaptic and glutamatergic (Behr et al., 1998). Additionally, high-frequency stimulation of afferent fibers from the EC results in LTP of these synapses in subicular neurons (Fidzinski et al., 2012). Conversely, low-frequency stimulation of EC fibers results in long-term depression. Interestingly, low-frequency stimulation of EC fibers induces disinhibition at CA1-SUB synapses, thereby facilitating CA1 input onto subicular neurons (Fidzinski et al., 2011).

Functionally, the EC provides place-related information in the form of a grid-like structure (Hafting et al., 2005), information about the animal's head direction (Giocomo et al., 2014), as well as information about locomotion speed (Hinman et al., 2016; Sargolini et al., 2006) and distance to environmental borders (Solstad et al., 2008) to the SUB. The spatial information of the EC is distinct from that of CA1 place cells. Despite grid cells realigning to new environments, they provide a global and relatively static signal of the animal's current location (Fyhn et al., 2007). In addition, boundary vector cells encode for the animals’ position in relation to environmental borders. These neurons increase their activity, when the animals reaches a specific border in its environment(Alexander et al., 2022; Cho and Sharp, 2001).

Beside hippocampal spatial information the SUB receives further cortical and subcortical input that is tuned to aspects of the animal’s movement in its environment. Spatially tuned input may come from the retrosplenial cortex (Alexander et al., 2022; Cho and Sharp, 2001) and border-and grid-tuned neurons of the parasubiculum (Boccara et al., 2010). Information about the animal’s head-direction can reach the SUB from the

retrosplenial cortex (Cho and Sharp, 2001), the nucleus reuniens (Wouterlood et al., 1990; Jankowski et al., 2014), and the anterior thalamic nucleus (Nelson et al., 2020; Frost et al., 2021). Velocity tuned input to the SUB can further arise from the nucleus of the diagonal band (Fuhrmann et al., 2015) and the retrosplenial cortex (Cho and Sharp, 2001).

1.3.2. Output of subicular pyramidal neurons

Like all subfields of the hippocampal system, a vast majority of pyramidal neurons in the SUB convey positional information (Sharp and Green, 1994; Brotons-Mas et al., 2010; Kitanishi et al., 2021). Subicular neurons are responsive to an animal's location, head direction, speed of movement, direction, and environmental boundaries (Barnes et al., 1990; Sharp, 1997; Anderson and O'Mara, 2003; Lever et al., 2009; Olson et al., 2017; Poulter et al., 2021; Ledergerber et al., 2021).

What distinguishes place-related firing in subicular neurons from that of other hippocampal subfields? First, subicular neurons tend to exhibit higher basal firing rates (Sharp, 1997). Second, the firing fields of subicular neurons are less well defined compared to those of CA1 place cells (O'Keefe and Dostrovsky, 1971; Hafting et al., 2005). Third, subicular place fields encompass larger regions of the environment, and a significant proportion of subicular neurons have multiple place fields (Sharp and Green, 1994; O'Mara et al., 2001). Fourth, subicular coding of place appears to generalize across different environments: Subicular neurons exhibit similar firing patterns in two neighboring spatially and visually distinct environments (Sharp, 1997), as well as during transitions between light and dark periods (Brotons-Mas et al., 2010). Fifth, there appears to be a gradient of place related firing along the proximo-distal axis. Compared to proximal neurons, distal dorsal subicular neurons show higher mean firing rates and higher spatial selectivity (Kim et al., 2012).

The issue of remapping in subicular cells is a current topic of debate. According to some evidence, subicular neurons maintain spatial firing fields that are consistent across different environments (Sharp, 2006). Boundary vector cells appear to be immune to environmental changes (Lever et al., 2009). However, others (Kim et al., 2012) have observed a variety of remapping in the SUB. While certain neurons undergo complete

remapping in different environments, others maintain place-related firing in the same locations. Overall, the extent of remapping in the SUB appears to be less than that in CA1.

The SUB's output is both multiplexed and conjunctive (Ledergerber et al., 2021), with single subicular pyramidal neurons combining multiple tunings. Additionally, while the overall activity of subicular neurons is higher (Kitanishi et al., 2021), their individual spatial selectivity is coarser when compared to other regions within the hippocampus (Lee et al., 2022). However, at a population level, the SUB conveys more spatial location information than CA1 (Kim et al., 2012), suggesting that the SUB compresses hippocampally processed spatial information to distribute it to multiple brain regions.

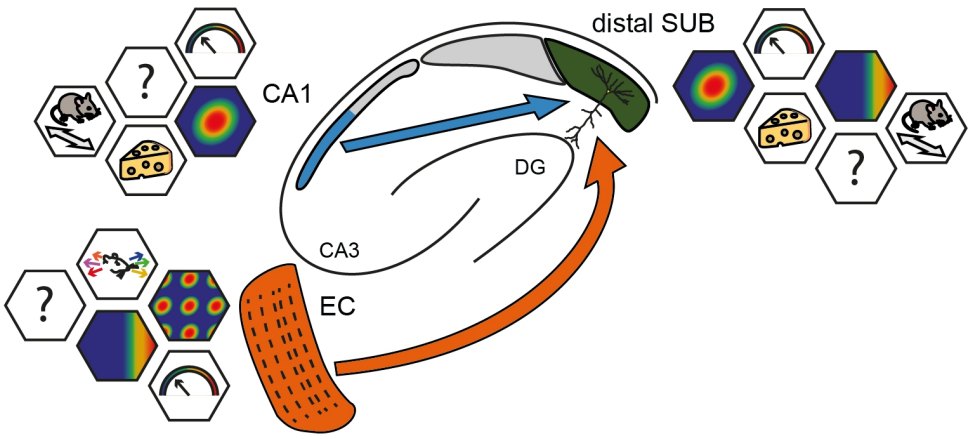

Figure 4: Tunings of subicular inputs and its output

Neurons in the hippocampal formation are tuned to different aspects of the animal's motion and environment that are used for spatial navigation. Some of these tunings are shared across regions, while others are region-specific. SUB neurons receive single-place tuned inputs from CA1. In contrast, the place-tuned input from EC is grid-like. In addition, CA1 input to SUB neurons can be reward-tuned, and EC input can be tuned to head-direction, environmental borders, or movement direction of the animal. Velocity tuned input to SUB can come from both CA1 and EC. The output of SUB can be tuned to location, boundaries, reward, and speed, as well as the animal's direction of travel.

1.4. Central hypothesis

The dorsal SUB serves as a central hub for distributing hippocampal spatial information throughout the brain. Its primary function is to integrate spatial information into a cohesive code, which provides the entire brain with navigation-related information. The majority of spatial information is received mono-synaptically by the distal-dorsal SUB from two subregions of the hippocampal formation, CA1 and EC. While some neurons in these regions are tuned to the same environmental factors, the majority of their neurons are tuned to distinct aspects of the animal's environment. The aim of this study was to investigate the functional input/output transformation of spatial information in distal - dorsal subicular pyramidal neurons, with the aim of unraveling the integration of the two major inputs to these neurons. First, if spatial information from CA1 and EC is conveyed to subicular neurons, these neurons will exhibit spatial tuning on the input level. To test this, postsynaptic currents were measured directly via whole cell patch clamp recordings while mice ran freely on an elevated circle. Second, CA1 and EC inputs converge within the same dorsal subicular neuron, and the position of their synapses is a crucial factor in determining how these inputs are integrated into the dendritic tree of the subicular neuron. The lack of anatomical layers indicates that the synapses of CA1 and EC intermingle in the dendritic tree of subicular neurons, suggesting a different mode of synaptic integration compared to CA1. I performed sub-cellular input mapping to investigate the functional synaptic distribution of both input paths. Third, both input paths are tuned to different environmental factors, which may have different effects on the spatial tuning of distal-dorsal subicular pyramidal neurons. By selectively reducing each input through chemogenetic inactivation of their synapses, this study provides novel insights into the pathway-specific contributions to the spatial tuning of distal-dorsal subicular neurons.

2. Materials and Methods

2.1. Experimental Model

Heterozygous VGluT2-Cre mice (Slc17a6tm2(cre)Lowl/J, stock number 016963, Jackson Lab, Bar Harbor, USA) and non-transgenic C57Bl/6J mice (stock number 000664, Jackson Lab, Bar Harbor, USA) of both sexes were used for this study. The animals were bred in-house and group-housed with one to five same-sex littermates in a standard plexiglass cage (Tecniplast, Buguggiate, Italy) where temperature and humidity were continuously controlled. The animals were maintained on a 12-hour light-dark cycle, which was reversed for animals during *in-vivo* experiments. Additionally, the cages were outfitted with a running wheel, and the mice had unrestricted access to food and water. All experiments complied with German animal use laws and were approved by the Landesamt für Natur, Umwelt und Verbraucherschutz in North Rhine-Westphalia, Germany (reference umber: 84-02.04.2017.A220), in accordance with the Directive of the European Communities Parliament and Council regarding the protection of animals used for scientific purposes (2010/63/EU)

2.2. Surgical procedures

2.2.1. Stereotactic viral injections

For intracranial virus injections, mice were anesthetized using an intraperitoneal injection of ketamine (0.13 mg/g) and xylazine (0.01 mg/g). The anesthesia depth was assessed based on breathing patterns and reflex responses. Further intraperitoneal injections of the aforementioned anesthetics (0.013 mg/g ketamine and 0.001 mg/g xylazine) were administered as required to maintain the anesthesia depth. Mice were immobilized using a non-punctuated head bar and nose clamp (MA-6N, Narishige), and secured in place using a motorized stereotactic frame (Luigs-Neumann, Ratingen, Germany). To maintain body temperature, a heating pad (Fine Science Tools, Heidelberg, Germany) was placed under the animal. A scalp incision was made, and the periosteum was removed. The head was then adjusted to align bregma and lambda on

the same horizontal plane.

Three brain regions were of interest in this study: the dorsal SUB, dorsal CA1 and the EC. The following stereotactic coordinates (Franklin and Paxinos, 2008) were used to target these brain regions: dorsal SUB: -3.2 mm anterior-posterior, 1.9 mm lateral, -1.5 ventral; CA1: -2 mm anterior-posterior, -2.5 mm lateral, -1.75 ventral; EC: -4.6 mm anterior-posterior, 3.3 mm lateral, -4.4 ventral. EC injections were done bilaterally, whereas the other injections were done in the right hemisphere only. After drilling (Ideal micro drill, World Precision Instruments, Sarasota, USA) a small hole through the skull above the region of interest, a 34-gauge needle and Hamilton syringe (World Precision Instruments, Sarasota, USA) was used for the injection.

For the *in vitro* experiments, two injections were performed. First, 350 nl of floxed tdTomato virus (5.9 x 10^{12} vg/ml, AAV1/CAG-Flex-tdTomato, UNC Vector Core) were injected into the dorsal subiculum of VGluT2-Cre mice. Second, 250 nl of unfloxed Chronos virus (4.5 x 10^{12} vg/ml, AAV9-Syn-Chronos-GFP, UNC Vector Core, Lot. Num.: AV6102C) were either injected into CA1 or EC. For *in vivo* experiments, two injections per animal were performed as well. First, 350 nl of a genetically encoded calcium indicator (2.96 x 10^{12} vg/ml, AAV1-Syn-Flex-GCaMP6s-WPRE-SV40, Addgene, ID: 100845) were injected in the dorsal SUB. Second, either the inhibitory hM4D Designer Receptors Exclusively Activated by Designer Drugs (DREADD) (8.6 x 10^{12} vg/ml, AAV5-hSyn-hM4D(Gi)-mCherry, Addgene, ID: 50475) or the control virus containing the structural marker mCherry (1.1x10^{13} vg/ml, AAV5-hSyn-mCherry, Addgene, ID: 114472) were either injected into CA1 (250 nl) or EC (400 nl). All injections were performed with the help of an UltraMicroPump (World Precision Instruments, Sarasota, USA) at a speed of 50 nl/min. Before withdrawal, the injection needle was kept in place for 10 min. Finally, the scalp was sewed with absorbable sutures (Vicryl Plus, Johnson & Johnson Medical GmbH, Norderstedt, Germany) and buprenorphine (0.05 mg/kg) was given intraperitoneally. In the following postoperative window of 3 days, mice recovering in their home cage were regularly monitored and received analgesia three times daily. After an expression time of at least 4 weeks, experiments were performed.

2.2.2. Hippocampal slice preparation

Mice were deeply anaesthetized with isoflurane (Forane, AbbVie Inc., Illinois, USA) and decapitated. The brain was quickly removed from the skull and placed in ice-cold choline-chloride-based cutting solution containing 110 mM choline-chloride, 2.5 mM KCl, 1.25 mM NaH_2PO_4, 25 mM $NaHCO_3$, 0.5 mM $CaCl_2$, 7 mM $MgCl_2$, and 25 mM glucose, 11.5 mM $C_6H_7NaO_6$, 3 mM $C_3H_3NaO_3$ (all chemicals purchased from Sigma Aldrich, St. Louis, USA), oxygenated with carbogen (95 % CO_2/ 5 % O_2). The olfactory bulb and the cerebellum were removed from the brain and 300 µm thick coronal slices were cut using a Leica VT-1200S vibratome (Leica Microsystems, Wetzlar, Germany). The tissue was kept in cooled and carbogenated cutting solution during slicing. Slices containing the dorsal SUB region of the hippocampus were stored in cutting solution and heated up to 35 °C for 30 minutes. Then, slices were kept in artificial cerebrospinal fluid (aCSF) consisting of: 125 mM NaCl, 2.5 mM KCl, 1.25 mM NaH_2PO_4, 25 mM $NaHCO_3$, 2.0 mM $CaCl_2$, 1.0 mM $MgCl_2$, and 20 mM glucose (all chemicals purchased from Sigma Aldrich, St. Louis, USA), continuously carbogenated at room temperature. Four slices containing dorsal SUB were available for the experiments. They were investigated for up to 5 hours after decapitation.

2.2.3. Hippocampal window surgery

For chronic imaging of neuronal activity in the dorsal SUB a hippocampal window above the SUB was implanted. This window consisted of a 1.5 mm long stainless-steel cannula (3 mm outer diameter). A round coverslip (3 mm diameter, Warner Instruments, Holliston, USA) was glued with UV curable adhesive (NOA81, Thorlabs, Dachau/Munich, Germany) to the bottom of the cannula. To locally apply the agonist for the inhibitory DREADD, a small hole was carefully drilled into the cover slip and was subsequently covered with a drop of silicon elastomer (Kwik-Sil™, World precision instruments, Sarasota, USA).

For the implantation of this window, mice were prepared for surgery as described above. In addition, mice were injected with dexamethasone (0.2 mg/kg), carprofen (5 mg/kg) and buprenorphine (0.05 mg/kg) intraperitoneally. The scalp over the parietal skull and the periosteum was removed. A craniotomy with a diameter of 3 mm was performed

over the SUB injection using a sharp dental drill (Ideal micro drill, World Precision Instruments, Sarasota, USA). Afterwards, the dura mater was removed, and the underlying cortex within the craniotomy (Broca Areas: B30.50, B27-50, SA1) was aspirated. Blood and aspirated tissue were washed out using a constant flow of 'cortex buffer' consisting of 125 mM NaCl, 5 mM KCl, 10 mM glucose, 10 mM HEPES, 2 mM $CaCl_2$, and 2 mM $MgCl_2$ (all chemicals purchased from Sigma Aldrich, St. Louis, USA). Intracranial aspiration was continued until the mediolateral fibers of the external capsule were clearly visible. The hippocampal window was gently fit into the craniotomy until the glass was in contact with the capsular fibers. Then, the hippocampal window and the craniotomy were sealed using dental cement (Gradia Direct Flo, GC Corporation, Tokyo, Japan). For awake head-fixation a small metal-bar (Luigs-Neumann, Ratingen, Germany) was placed paramedian on the skull and fixed with the dental cement. After surgery, animals were continuously monitored until they recovered. In the postoperative window of 3 days following surgery, mice recovered in their home cage and were regularly monitored and received buprenorphine (0.05 mg/kg) as analgesic twice a day.

2.2.4. Surgery for *in vivo* patch clamp recordings

To perform *in vivo* patch clamp recordings, a part of the animal's skull had to be removed. Therefore, my colleague, Dr. Kaneko prepared the mice for the surgery as described above. A craniotomy of approximately 2 mm in diameter was performed over the dorsal SUB (AP -3.2 mm, ML: +1.9 mm from bregma). A small hole for the ground electrode was drilled in the skull above the cerebellum, and a metal bar (Luigs & Neumann, Ratingen, Germany) was placed for head fixation and secured with dental cement. To prevent infection, the craniotomy and small hole were covered with silicone elastomer (Kwik-Cast, World Precision Instruments, Sarasota, USA). Mice received post-surgery care as described above.

2.3. Behavioral training

Head-fixed mice were trained to run on a custom-built self-propelled linear treadmill (Luigs-Neumann, Ratingen, Germany) while two-photon calcium imaging was performed (Fuhrmann et al. 2015). The linear treadmill belt was 7 cm wide and 3.6 m

long. It was subdivided into 6 x 60 cm long parts with different visuo-tactile patterns on them. Belts were not shared between animals. The linear treadmill was placed in a dark and noise-reduced environment. In addition, animals received a drop of condensed milk in a defined reward zone on the belt (Barnstedt et al. 2023).

Animals underwent the following training schedule before the start of imaging experiments: one week after the implantation of the hippocampal window, animals were handled by the experimenter for 10 minutes daily over the course of five days. Then, the animals were introduced to the linear treadmill for 3 days. In the following 3 days, they were habituated to the fixation with the head holder and received a liquid condensed milk reward whenever they started to run on the linear treadmill. In the following days, the reward was only given in the defined reward zone. Each mouse was trained until it was able to reliably run at least 10 rounds in 10 minutes.

In addition to the training program, mice were food restricted. The initial weight of each animal was determined for one week before the hippocampal window implantation. Over the time of handling the animal, the amount of food presented to the animals was decreased by 80% of their measured daily food intake. Each mouse's body weight was controlled daily and decreased to 85 - 90% of its pre-restriction weight. This body weight was maintained until the end of the experiment. Mouse body weight and its general health status were being closely monitored throughout.

Animal's performance on the linear treadmill was recorded via an optical sensor (Luigs & Neumann, Ratingen, Germany) measuring the rotation of the treadmill cylinder underneath the mouse. In addition, lick signals were measured by an analog piezo sensor. All signals were collected at 10 kHz by an I/O board (USB-6212 BNC, National Instruments, Austin, USA) and recorded using custom-written Python software. All running traces and lick signals were stored on a hard disk and analyzed offline.

For *in vivo* electrophysiology, mice were habituated to Dr. Kaneko and the experimental setup two weeks after surgery. On the first and the second day, mice were exposed to the experimenter and placed on the hand for 30 minutes. From the third to the fifth day, mice were placed on the circular track for 30 minutes each day to acclimate to the environment. The circular track was 8 cm wide with an outer diameter of 70 cm placed in a cylinder with distant landmarks (Figure 7 A). The mice were not overtrained to

prevent mice from running at high speeds on the track and allow for a stable whole-cell recording.

2.4. Data Acquisition

2.4.1. Patch clamp recordings in hippocampal slices

For patch clamp recordings, hippocampal slices were placed in a recording chamber on an upright light microscope (SliceScope, Scientifica Ltd., Uckfield, United Kingdom) and continuously super-perfused with carbogenated aCSF. In addition, aCSF was heated to a temperature of 35 ± 0.5 °C (Bath controller V, Luigs & Neumann, Ratingen, Germany). Recordings were obtained from either red fluorescent ($VGluT2^+$) or non-fluorescent neurons visualized by infrared differential interference contrast (DIC) (TH4-200 Halogen lamp, Olympus, Tokyo, Japan; IR-1000 Infrared CCD Monochrome Video Camera, DRAGE-MIT, Michigan, USA) and fluorescence microscopy for tdTomato identification (BX-RFA, Olympus, Hamburg, Germany). Whole-cell current-clamp recordings were performed using a Dagan BVC-700A amplifier (Minneapolis, USA) and digitalized at 50 kHz or higher sampling rates using an ITC-18 interface board (HEKA Elektronik, Lambrecht, Germany) controlled by custom-written scripts in IgorPro software (v6.2, WaveMetrics, Portland, USA). The recording pipettes with a resistance of 4-6 MΩ were filled with intracellular solution containing 115 mM K-gluconate, 20 mM KCl, 10 mM HEPES-acid, 10 mM phosphocreatine, 2 mM Mg_2ATP, and 0.3 mM NaGTP, and 4% biocytin (all chemicals purchased from Sigma Aldrich, St. Louis, USA). Recording pipettes were placed on the soma (PatchStar Micromanipulator, Scientifica Ltd., Uckfield, United Kingdom) of identified subicular neurons and Giga-seals (resistance > 1.5 GΩ) between membrane and pipette were established. Pipette capacitance was compensated accordingly for each recording. Whole-cell-patch-clamp configuration was achieved by applying negative pressure to the micropipette. The series resistance was also compensated in all recordings using bridge balance in current clamp mode. Series resistance compensation was carefully monitored and controlled during the recordings; series resistance values were determined after break-in and did not exceed 30 MΩ. Recordings were not corrected for liquid junction potential. Recordings were saved on a hard disk and analyzed off-line.

2.4.2. Electrophysiological characterization

Electrophysiological characterization of subicular neurons was based on membrane potential responses to step current injections lasting 500 ms with various amplitudes. First, for passive properties, currents of -30 pA, -20 pA, -10 pA, 10 pA, 20 pA and 30 pA were injected. For subthreshold properties in the hyperpolarising direction, negative current injections were applied until the maximum deflection of the membrane potential was -50 mV. Next, the rheobase was determined as the minimum amount of current necessary to elicit an action potential. For subthreshold properties in the depolarizing direction, 10 pA lower than the rheobase were injected. Furthermore, firing properties were calculated from membrane potential responses to current injections of three times the rheobase.

2.4.3. Channelrhodopsin-assisted circuit mapping

For channelrhodopsin-assisted circuit mapping (CRACM), either CA1 or EC axons that expressed the opsin Chronos (Figure 5 A) were activated by a 473 nm diode laser (LuxX 473-80, Omicron Laserage, Rodgau-Dudenhofen, Germany). The photo-stimulation was performed through the objective with a laser control system (488 nm; Rapp OptoElectronics, Wedel Germany). The spot size of laser stimulation was 35 µm and the inter-spot distance was 50 µm. A grid of 16 x 18 spots was stimulated covering 600 µm horizontally and 800 µm vertically (Figure 5 C). Each spot was illuminated for 3 ms while the post synaptic responses at the soma were recorded in current clamp mode. During these mapping experiments, bath-application of 1 µM TTX (Torcis Bioscience, Cat. No. 1069, Bristol, United Kingdom) and 100 µM 4-AP (Sigma Aldrich, Cat. No. A7840, St. Louis, USA) blocked action potential generation and increased axonal excitability. Thus, transmitter release was facilitated, and di-synaptic membrane potential responses were prevented. In addition, GABAergic transmission was blocked by bath-application of 10 µM SR-95531 (Torcis Bioscience, Cat. No. 1262, Bristol, United Kingdom) and 1 µM CGP-52432 (Torcis Bioscience, Cat. No. 1246, Bristol, United Kingdom). Each spot was stimulated pseudo-randomly 5 times. At the end of the experiment, the glutamatergic blockers 10 µM NBQX (Torcis Bioscience, Cat. No. 1044, Bristol, United Kingdom) and 50 µM D-AP5 (Torcis Bioscience, Cat. No. 0106 Bristol,

United Kingdom) were applied to the bath to confirm the glutamatergic nature of the postsynaptic potentials elicited with the stimulation (Figure 5 D). The fluorescent dye Alexa Fluor™ 594 (100 µM, Thermo Fisher Scientific, Massachusetts, USA) were added to the recording pipette to allow for visualization of soma and primary trunk under the microscope. Pictures of the recorded neurons were taken, and the direction of the primary trunk was used to align the input maps of several subicular neurons (Figure 5 E).

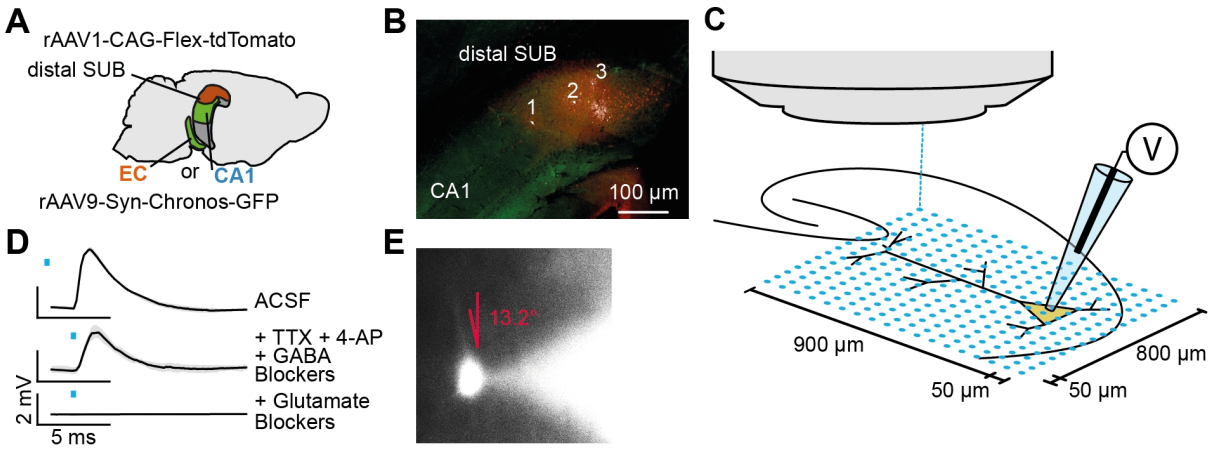

Figure 5: Channelrhodopsin assisted subcellular input mapping

Experimental design of channelrhodopsin assisted subcellular circuit mapping. A: AAV9-Syn-Chronos-GFP were injected locally in either CA1 or EC. In addition, Cre-dependent expression of subicular VGluT2^{+} neurons was achieved by injection of AAV1/CAG-Flex-tdTomato in dorsal SUB of VGluT2-Cre mice. B: Confocal image confirming the expression of GFP (green) in axons and tdTomato (red) in VGluT2^{+} subicular neurons. Furthermore, during whole cell patch clamp recordings, neurons were filled with biocytin. Counterstaining of biocytin with streptavidin-'Alexa Fluor 647' enabled me to find the recorded neurons (white). C: Whole cell patch clamp recordings of tdTomato positive subicular neurons in acute coronal slices. The opsin Chronos was locally activated with a 35 µm spot of laser light (488 nm) in a grid of 50 µm x 50 µm, covering 900 µm x 800 µm around the patched neuron. D: Simultaneously, PSPs were measured. To capture only monosynaptic excitatory PSPs, TTX and 4-AP as well as GABAergic blockers (SR-95521 and CGL-52432) were bath applied. After each mapping experiment, the glutamatergic nature of the PSP was confirmed with bath application of NBQX and DAP-5. E: The resulting input maps of different neurons were aligned to the position of the trunk in the slice.

2.4.4. Staining of patched neurons

After the experiment, brain slices were fixated in 4% paraformaldehyde (PFA, Roti-Histofix, Carl Roth, Karlsruhe, Germany) solution for 24h at 4 °C and subsequently washed twice in phosphate-buffered saline (PBS, No. P4417, Sigma Aldrich, St. Louis, USA) for 10 min each time. Free-floating sections were permeabilized for 15 min in Tris-buffered saline (TBS, Sigma Aldrich, St. Louis, USA) + 0.5% Trition X-100. Afterwards, slices were incubated with streptavidin (Alexa Fluor 647, Life Technologies, S21374, 1:500) in TBS + 2% normal donkey serum (NDS, Sigma Aldrich, St. Louis, USA) for 5 h at room temperature. Slices were then washed twice with PBS for 10 min and mounted with Aqua-Poly/Mount (18606-20, Polysciences, Inc., Warrington, USA) on glass slides.

Biocytin-filled cells were identified at 10× magnification (Plan-Apochromat 10×/0.45, Zeiss, Jena, Germany) using a confocal laser microscope (LMS 700, Zeiss, Jena, Germany). Tile-stacks of entire cells were acquired with a high numerical-aperture 20× objective (Plan-Apochromat 20×/0.8, Zeiss, Jena, Germany) and automatically stitched by the acquiring software ZEN (Zeiss, Jena, Germany). Recorded neurons were checked for an intact dendritic arbor reaching the bottom end of the molecular layer (Figure 5 B).

2.4.5. *In vivo* patch clamp recordings

My colleague Dr. Kaneko performed the *in vivo* patch clamp recordings. Three weeks after surgery, mice were head-fixed on a short treadmill (46 cm length), and the silicone covering the craniotomy was carefully removed. A silver-chloride wire was inserted into the small hole above the cerebellum for grounding, allowing the electrode tip to contact the brain surface. A patch pipette (3 cm long) with a resistance of 5 - 7 MΩ was filled with intracellular solution containing 140 mM K-gluconate, 5 mM KCl, 0.5 mM MgCl2, 5 mM HEPES, 0.16 mM EGTA, 5 mM Na-phosphocreatine (for voltage clamp recording) or 140 mM K-gluconate, 7 mM KCl, 0.5 mM $MgCl_2$, 5 mM HEPES, 0.16 mM EGTA, 5 mM Na-phosphocreatine (for current clamp recordings). To prevent neurons from firing, the intracellular solution for voltage clamp recordings contained 1 mM QX-314, and 4% biocytin. Patch pipette and pipette holder, attached to a manipulator by a magnet, were positioned slightly above the brain surface through a sapphire cylinder placed on a

metal ring plate attached to a metal rod. Light-curing dental cement (Gradia Direct Flo, GC Corporation, Tokyo, Japan) was applied between the sapphire cylinder and the metal ring plate. The patch pipette was then lowered under high positive pressure (500-700 mbar) until it reached the SUB cell layer, 1.0 mm from the brain surface. A self-developed algorithm in Igor Pro (v8, WaveMetrics, Portland, USA) was used for automatic cell search, while the patch pipette lowered through the cell layer (1.0 - 1.4 mm from brain surface). All electrophysiological signals were amplified with an ELC-03XS amplifier (npi electronic, Tamm, Germany) and digitized with a LIH-8+8 interface (HEKA Elektronik, Lambrecht, Germany). After establishing the whole-cell configuration, step currents (500 ms, -200 and +300 pA) were injected, and only cells showing firing activity were selected for further experiments. After the adhesive was cured with blue light, the pipette holder was detached from the manipulator by electrically removing the magnetic force (Figure 8 A). The mouse was then led into the arena, where either membrane currents in voltage clamp-mode (holding potential at -70 mV) or membrane potentials in current clamp-mode were recorded while the mouse moved freely. Mouse behavior was recorded with a Kinect (Microsoft, Seattle, USA) or with a Basler Camera (Model: acA2040-90umNIR, Basler, Ahrensburg, Germarny) at 30 or 60 fps from above, respectively.

2.4.6. Two-photon calcium imaging with CNO application

An upright resonant scanning microscope (TrimScope II, LaVision BioTec; Bielefeld, Germany) was used for two-photon calcium imaging of dorsal VGluT2^{+} subicular neurons. Two-photon excitation was provided by a Ti:sapphire excitation laser (Chameleon Ultra II, Coherent, Santa Clara, USA) tuned to optimal fluorescence excitation of GCaMP6s at a wavelength of 920 nm. GCaMP6s fluorescence emission was isolated using a band-pass filter (525/40, Semrock, Rochester, USA) and detected using a GaAsP PMT (H7422-40, Hamamatsu, Herrsching am Ammersee, Germany). With a 16× water immersion objective (N16XLWD-PF, Nikon, Düsseldorf, Germany), image series of around 800 × 800 µm were acquired with 1024 × 1024 pixels at 15.3 Hz. The whole microscope was controlled using Imspector software (LaVision BioTec, Bielefeld, Germany). The acquisition signal for each imaging frame was recorded by an I/O board (USB-6212 BNC, National Instruments, Austin USA) to align imaging with

behavioral recordings.

Mice were habituated to the imaging apparatus during the training period. For the experiment, the silicon plug of the hippocampal window was carefully removed with fine forceps (Figure 6 A). Then, mice were placed on the linear treadmill and head-fixed. Cortex buffer (heated to 36 °C) was used to fill the space between objective and the glass floor of the hippocampal window. After an initial round of imaging for 10 minutes, standard cortex buffer was replaced with cortex buffer containing 0.003 mM (Stachniak et al., 2014) Clozapin-N-Oxid (CNO; Figure 6 B; Sigma Aldrich, Cat. No. C0832, St. Louis, USA). In the following 30 minutes mice were left head-fixed on the linear treadmill were they were able to move but did not receive any reward. Then the same field of view was imaged for an additional 10 minutes. After the experiment, the hole in the imaging window was closed with silicon and mice were transferred back into their home cages.

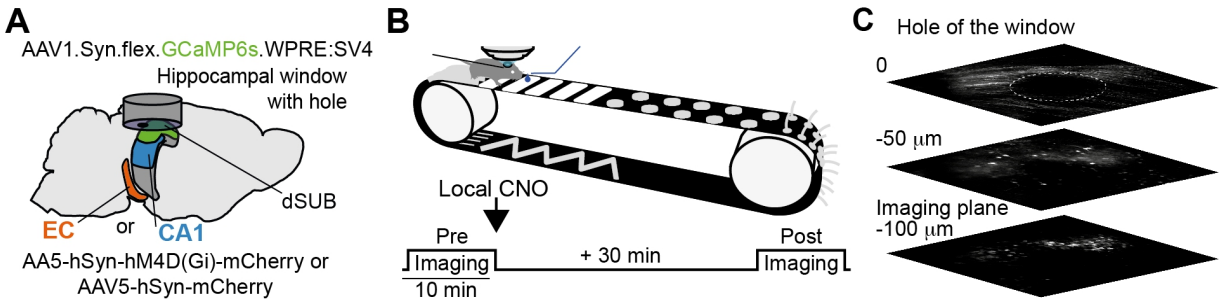

Figure 6: *In vivo* two-photon calcium imaging with chemo-genetic reduction of inputs

A: For two photon calcium imaging in VGluT2$^+$ subicular neurons, VGluT2-cre mice were injected with AAV1.Syn.flex.GCaMP6sWPRE:SV4. In addition, either neurons of CA1 or EC were virally transfected with the inhibitory DREADD hM4D(Gi). B: Calcium activity of VGluT2+ subicular neurons were recorded trough a hippocampal window with two-photon imaging, while mice were running on a linear track. After an initial (Pre Imaging) recording, the DREADD-agonist CNO was applied through the perforation in the imaging window. After 30 minutes the calcium activity of subicular VGluT2$^+$ neurons was recorded again (Post Imaging). C: Z-projection from the bottom of the hippocampal window until the imaging plane showing the perforation of the imaging window. Subicular neurons were imaged at least 100 µm from the glas bottom of the imaging window.

2.4.7. Transcardial perfusion fixation and confocal slice microscopy

After completing the in-vivo experiments, I extracted the brain tissue of each animal to check for the injection sites of the inhibitory DREADD and the calcium indicator. Therefore, I anesthetized the animal with a lethal dose and opened the thorax. The pericardium was removed and the left ventricle was pierced with an injection needle for perfusion. Perfusion of PBS (Sigma Aldrich, St. Louis, USA) was carried out at a rate of 5 ml/min using a peristaltic pump (PeriStar Pro, World Precision Instruments, Sarasota, USA) after incising the right atrium. Once the perfusion solution was free of blood, it was switched to 4% PFA (Roti-Histofix, Carl Roth, Karlsruhe, Germany) and perfused for 15 minutes. Subsequently, the brain was removed from the skull. The tissue was stored in 4% PFA for 1 hour at room temperature or overnight at 4°C to improve fixation efficiency before being transferred into PBS.

For microscopic imaging, the brain tissue embedded in 2% agarose (No A6877, Sigma Aldrich, St. Louis, USA) was sliced into 100 µm thick sections using a Leica VT-1200S vibratome (Leica Microsystems, Wetzlar, Germany). Free-floating slices washed twice in PBS (PBS, No. P4417, Sigma Aldrich, St. Louis, USA) and stained with 300 nM DAPI (4′,6-diamidino-2-phenylindole, Cat. No. D1306, Thermo Fisher Scientific, Massachusetts, USA) for 5 min. Then slices were washed again twice with PBS and mounted with Mowiol 4-88 (Calbiochem®, Merck, Darmstadt, Germany) and stored at 4 °C. High-resolution images were acquired using an upright laser scanning confocal microscope (Leica TCS SP8, Leica Microsystems, Wetzlar, Germany) using a 40x oil immersion objective (HC PL APO CS2 40X, Leica Microsystems, Wetzlar, Germany).

2.5. Data Analysis

All analyses described were done with custom written Python scripts (version 3.7).

2.5.1. Analysis of electrophysiological profiles

The electrophysiological profiles of dorsal subicular neurons were generated based on sub- and suprathreshold membrane potential responses to step current injections lasting 500 ms with various stimulation intensities (Sosulina et al., 2006; Prönneke et al., 2015; Justus et al., 2017; Komendantov et al., 2019).

To quantify subthreshold membrane properties, the following parameters were calculated: input resistance, membrane time constant (τ), sag index at hyperpolarization (Hypo Sag Index), sag index (Depo Sag Index) and rebound hyperpolarization (Depo Rebound Index) with depolarizing current injections. Input resistance and tau were calculated from current injections of -30 pA to +30 pA. Input resistance was calculated as the slope of the relationship of the injected current and the steady state voltage response. Tau was estimated as the time from current pulse onset to 63% of the maximal membrane response. To calculate sag indices, the difference between the maximal membrane potential response (between stimulus onset and 300 ms) and the steady state response (100 ms before stimulus offset) was divided by the amplitude of the maximal membrane potential response. This procedure was done for membrane potential responses to just-subthreshold current injection (Depo Sag Index) and current injection with a membrane response of -50 mV (Hypo Sag Index). For the Depo Rebound Index, the amplitude of rebound hyperpolarization after the stimulus offset was divided by the steady state response to the depolarizing stimulation.

Action potential (AP) properties were calculated from current injections with rheobase stimulations. Rheobase was defined as the minimum amount of current needed to elicit action potential firing. The number of action potentials at rheobase (Num Aps) was determined. The AP threshold (Threshold) was measured as the membrane potential where the derivative of the membrane potential reached 10% of the maximum slope of the action potential. Action potential amplitude was measured from baseline. Time to Peak was calculated from Threshold. The mean instantaneous firing frequency was

calculated from current injections three times the rheobase.

For identification of electrophysiological subtypes in subicular neurons, hierarchal clustering on the parameters described was performed. First, values were normalized, and the squared Euclidean distance was calculated. Then, unsupervised clustering with Ward's method was performed (Halabisky et al., 2006; Perrenoud et al., 2013; Sosulina et al., 2006). Finally, VGluT2 identity was mapped onto the classified neurons and Fisher's exact test was performed to estimate whether the distribution of VGluT2 marker is not random among electrophysiological subtypes of subicular pyramidal neurons.

In vivo electrophysiological characterisation was performed on step current injections lasting 500 ms with an amplitude of 300 pA. Neurons were classified as bursting, when two or more action potentials were riding on a depolarisation hump. In addition, pyramidal neurons were distinguished from fast-spiking interneurons by the action potential half-width, which was higher than 4.5 ms (Cea-del Rio et al., 2011; Péterfi et al., 2012).

2.5.2. Analysis of input maps

For the analysis of CRACM experiments, individual whole cell membrane potential traces were tested for the appearance of a PSP after light stimulation. To this end, the following function was fitted:

$$f(t) = scale * \left(1 - e^{-\frac{t}{\tau_{ON}}}\right)^5 * \left(e^{-\frac{t}{\tau_{OFF}}}\right) \quad (1)$$

to the baseline-substracted membrane potential (Magee and Cook, 2000). τ_{on} and τ_{off} represent the time constants for the rise and the decay of the PSP, respectively. The fit was only accepted if the coefficient of determination (R^2) was higher than 0.9. One stimulation spot was classified as responsive when at least 3 out of 5 repetitions elicited a somatic PSP. The mean amplitude of the successful stimulations was calculated for each stimulation spot.

To quantify the distribution of the PSP as a function of the stimulation spot, input maps were created from the normalized amplitudes of the postsynaptic membrane potential for each neuron. Two separate approaches were used to summarize these input maps

for each of the two input streams coming from CA1 or EC. First, the input maps were corrected for the angle of the primary trunk for each neuron and superimposed. Then, the mean amplitudes of the PSPs were calculated for each stimulation spot. The horizontal and vertical distributions of postsynaptic potentials were compared. Second, the following 2D-Gaussian function was fitted:

$$f(x,y) = scale * \exp\left(-\frac{(x-x_0)^2}{2*\sigma_x^2} - \frac{(y-y_0)^2}{2*\sigma_y^2}\right) \quad (2)$$

to the individual input maps (Manu and Baccus, 2011; Neef et al., 2018). Here, the coefficient x_0, y_0 is the center, and σ_x, σ_y are the widths of the distribution in x and y. Again, these parameters were compared between the two input streams.

2.5.3. Analysis of locomotion

On the linear treadmill, the position of the animal was tracked by an optical sensor (Luigs & Neumann, Ratingen, Germany) measuring the rotation of the treadmill cylinder underneath the mouse. The animal's spontaneous locomotion speed was computed as the first derivative of the animal's position. The locomotion speed signal was then noise compensated with a Kalman filter:

$$V = f'(Position) \quad (3)$$

$$V = \lim_{x_1 \to x_0} \frac{f(x_1) - f(x_0)}{x_1 - x_0} \quad (4)$$

$$V = \lim_{\Delta x \to 0} \frac{\Delta y}{\Delta x} \quad (5)$$

The position of the freely moving animal on the elevated circular track was extracted from top-down videos using DeepLabCut (Mathis et al., 2018). 5 points of the mouse body (left and right ear, nose, tail, center) were manually annotated in 50 frames per video. The network (ResNet-50) was trained up to 10^6 iterations. The center of mass (COM) was calculated from the average of the five coordinates for each mouse's body part. Outlying positions of single points of the mouse body (> 5 times standard deviation) were neglected from the COM. The animal's position was linearized as the angle of the COM in the circular track. This angle was then converted to the distance from the rightmost part of the circle and the instantaneous movement speed of the animal was calculated as first derivative of the position (Figure 7 B). The noise of this signal was compensated with a Gaussian moving average filter (window size: 10 frames). Immobility or resting were defined as time points with a velocity slower than 0.1 cm/s, while running is considered as velocities faster than 2 cm/s.

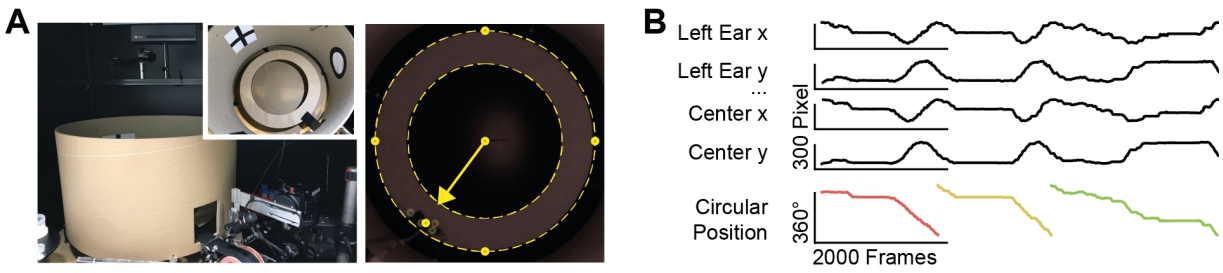

Figure 7: Movement tracking on the elevated circle

A: Experimental setup for electrophysiological recordings in freely moving mice. Mice were running freely on an elevated circle placed inside an open tube with landmarks. Using DeepLabCut we tracked 5 points of the mouse body (right image: bottom left; images provided by Dr. Kaneko). B: The animal's position was taken from the average of these five points and aligned to the center of the circle as circular position. Colors indicate different laps on the circular track.

2.5.4. Analysis of *in vivo* patch clamp recordings

For whole-cell voltage-clamp recordings, putative movement artifacts identified by membrane currents exceeding 10 times the standard deviation of the whole recording were omitted from further analysis. The baseline of the voltage clamp recordings was calculated using a LOWESS filter (fraction: 1%; delta of 1 second) (Seabold and

Perktold, 2010; Chew et al., 2022). Then, the baseline was subtracted from the recording. To account for all inward currents and to increase the signal to noise ratio of the recording, a Hilbert transform was applied to the inward currents of the recording. The resulting envelope of the excitatory currents was used for further analysis. For *in vivo* membrane potential recordings, the baseline was calculated with the LOWESS filter and subtracted from the recording. The Hilbert-transformed membrane current recordings and the baseline-corrected membrane potential recordings were correlated with the animal's position and velocity on the circular track (Figure 8 B).

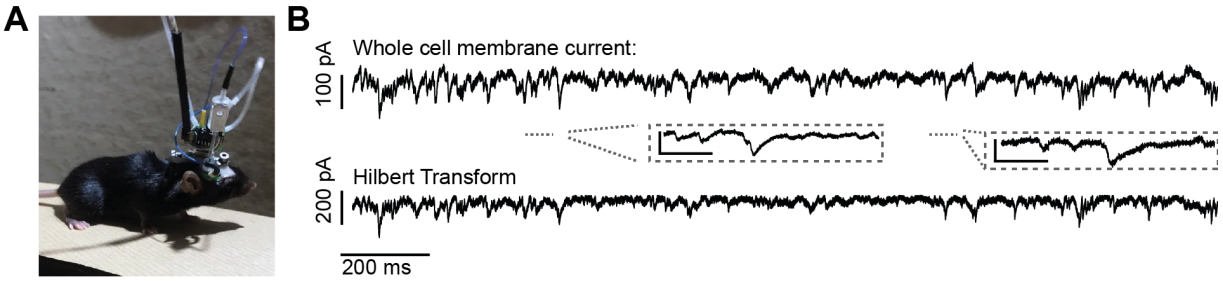

Figure 8: *In vivo* whole cell voltage clamp recordings

A: Experimental setup for whole cell patch clamp recordings in freely moving mice. After whole cell patch clamp configuration was achieved, a miniaturized headstage was fixed to the animal's head. Then, the animal was released onto the elevated circle and could freely move there. B: Exemplary whole cell membrane current recording (top) with two examples of excitatory PSPs (middle, scale bars: 100 pA and 20 ms). The whole cell membrane current recordings were processed with a Hilbert-transform (bottom) before being correlated to the animal's position and its velocity on the elevated circle. Image and data provided by Dr. Kaneko.

2.5.5. Calcium signal processing

Two-photon calcium imaging data was processed by Dr. Barnstedt using custom-written software in Python, largely based on CaImAn (v1.6.2) (Giovannucci et al., 2019). First, green channel 16-bit TIFF stack files (1024×1024 pixels times 9,000 frames) were resampled to 1 px/µm. Then, the image series was motion-corrected using NormCorre piecewise rigid (parameters: max_shifts = 40, num_frames_split = 2000, overlaps = 46, splits_els = 4, strides = 255). Furthermore, non-negative matrix factorization (CNMF) was used for cell segmentation. Resulting calcium traces were detrended and the ΔF/F

was calculated by normalizing all values to the median of the background fluorescence. Built-in CaImAn quality criteria were used to automatically filter spatio-temporal components based on spatial footprint consistency, trace signal-to-noise ratio, and shape of components analyzed by a CNN-based classifier. Finally, I performed identity- and behavior-blind manual inspection of the remaining calcium traces. Cell segmentation was performed separately on both the pre- and post-imaging sessions. The CaImAn function "register_ROIs" was employed to identify identical neurons in both sessions (parameters: threshold cost = 0.7, maximum distance = 10), followed by manual inspection of the paired ROIs (Figure 6 D, E).

2.5.6. Analysis of subicular tunings

Behavioral data (animal's position and velocity) were either downsampled to match the sampling rate of the two-photon calcium imaging or upsampled to match the sampling rate of the whole cell patch clamp recording. The following tunings for subicular neurons were calculated: For the spatial tuning of subicular neurons, the continuous belt positions were divided into 45 bins of 8 cm length each. During running episodes, the mean neuronal activity per bin was taken to calculate the spatial information (SI) as follows (Skaggs et al., 1993):

$$SI = \sum_i o_i \cdot a_1 * \log_2 \frac{a_i}{a_{All}} \quad (6)$$

where i is the i-th spatial bin, o_i is the animal's occupancy at the spatial bin i, a_i is the mean neuronal activity at spatial bin i and a_{All} denotes the overall mean neuronal activity. This calculated SI was compared to 100 random shuffles of the neuronal activity. For each shuffle the neuronal activity was cut into episodes of at least 500 frames that were randomly aligned with the animal's position trace. The mean neuronal activity per position-bin was taken to calculate the SI for each shuffle. When the observed SI was higher than the 95th percentile of the 100 randomly position-shuffled SI values the neuronal activity was considered spatially tuned.

As a second measure of spatial tuning, the average activity per spatial bin was transformed to polar coordinates, where q was the track position and r was the average activity amplitude at that position. The two-dimensional COM of the points was computed (Gauthier and Tank, 2018). Neurons were considered spatially tuned when the distribution of the activity passed the Rayleigh test ($p < 0.05$) indicating a non-homogeneous distribution of activity around the spatial bins (Sharif et al., 2021). As a measure of the tuning's magnitude, the vector length to the COM was calculated.

For velocity correlation, the instantaneous velocity was binned into 1 cm/s bins starting from 2 up to 30 cm/s. Neuronal activity was averaged correspondingly and the linear regression of the average activity amplitude as a function of the velocity bins was calculated. Neuronal activity was considered velocity tuned, when the regression was significant ($p < 0.05$) and the slope of the regression indicated the strength of velocity tuning (Kropff et al., 2015).

To test whether neuronal calcium activity was tuned to the animal's licking behavior, I plotted calcium activity on a logarithmic scale for time points when the animal licked and when it did not. We calculated the median difference from these distributions as the Lick Index. I then used the Wilcoxon signed-rank test to determine if there was a significant difference between the two distributions. Neurons were classified as 'lick-tuned' if there was a significant difference in calcium activity during licks compared to non-lick time points.

2.6. Statistical analysis

The experimenter was not blind to subject treatments and no statistical methods were employed to predetermine sample size. Custom-written Python scripts utilizing the pingouin package (ver. 0.5.3) (Vallat, 2018) or GraphPad Prism (ver. 8.0; GraphPad Software Inc, Boston, USA) were employed to analyze the data. Normality of data distribution was tested using the Shapiro-Wilk test, and two groups were compared utilizing either the parametric student t-test or non-parametric Wilcoxon signed-rank test. Comparison of three non-normally distributed groups was analyzed with the Kruskal-Wallis test followed by Dunn's multiple comparison test. Furthermore, repeated measures two-way ANOVA followed by Sidak's multiple comparison tests were used in

this study. In addition to classical statistical testing, I used estimation statistics for some of the analysis utilizing the Python package DABEST (Ho et al., 2019). The main text, figures, and figure legends provide detailed information regarding statistical tests and sample size. Mean ± standard deviation is used to represent normally distributed data. Non-parametric variables were presented as medians and interquartile ranges within the 25^{th} to 75^{th} percentile. Statistical analyses were performed using two-tailed tests, with an alpha level of $p < 0.05$. P-values were expressed in the following way: * $p < 0.05$, ** $p < 0.01$, *** $p < 0.001$, **** $p < 0.0001$.

3. Results

3.1. Place- and locomotion speed-tuned input in subicular neurons

The output of the dorsal subicular neuron conveys information about an animal's spatial navigation in its environment (Sharp and Green, 1994; Lever et al., 2009; Olson et al., 2017; Ledergerber et al., 2021). Subicular neurons' action potential firing is mainly tuned to the animal's position and its locomotion speed. My first objective was to ascertain whether this representation of position and movement speed occurs already at the input level in these neurons. To accomplish this, my colleague, Dr. Kaneko, conducted whole-cell patch-clamp recordings of mice freely navigating on a circular track before I analyzed the resulting data.

3.1.1. *In vivo* recordings reveal two electrophysiological cell types in the dorsal SUB

Whole-cell patch-clamp recordings were conducted by targeting the SUB with stereotactic coordinates through the intact cortex (Figure 9a, see Materials and Methods). To evaluate the firing attributes of each patched cell, step current injections were performed in current-clamp mode immediately after initiating the whole-cell patch-clamp configuration, where minimal diffusion of the pipette solution into the neuron is to be expected (Figure 9 A). Cells that did not exhibit any action potential firing were excluded from further recordings. Among the cells that showed action potential firing, two distinct action potential firing patterns could be detected, namely, regular spiking (Figure 9 B) and bursting (Figure 9 C). These firing types have been demonstrated earlier in *in vitro* recordings (Taube, 1993; Behr et al., 1996; Jarsky et al., 2008; Graves et al., 2012; Böhm et al., 2015; Cembrowski et al., 2018a). Regular spiking neurons (n = 17) were differentiated by a single action potential. On average, they had an action potential amplitude of 64.0 ± 10.5 mV and an action potential half-width of 0.7 ± 0.2 ms. Single-spiking neurons with an action potential half-width less than 4 ms (n = 3) were considered putative fast spiking interneurons and subsequently excluded from further

experiments. The second firing pattern observed was bursting. Bursting neurons (n = 48) were identified as having two or more action potentials riding on a depolarization hump. On average, their first action potential had an amplitude of 66.8 ± 11.2 mV and an action potential half-width of 0.8 ± 0.2 ms.

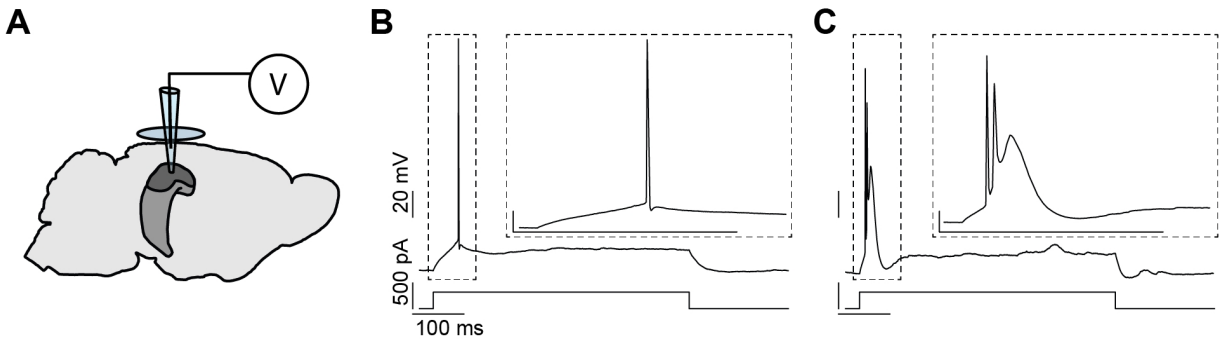

Figure 9: Electrophysiological cell types in the SUB *in vivo*

A: *In vivo* whole-cell patch-clamp recordings were performed through the intact cortex using the following stereotactic coordinates: AP -3.2 ± 0.5 mm, ML: +1.9 ± 0.5 mm from bregma. B, C: Two types of action potential firing were found in the dorsal SUB: regular spiking (B) and bursting (C). Bursting is characterized by two or more action potentials riding on a depolarizing hump (C inlet). Data were acquired by Dr. Kaneko.

3.1.2. The cumulative input of subicular pyramidal neurons is tuned to place and locomotion speed

After evaluation of the firing properties of a patched subicular patched neuron, the mouse was released onto an elevated circular track in a cued environment (Materials and Methods, Figure 7 A). The radial position of the circle was used to linearize the mouse position (Figure 7 B), and in a small number of recordings (n = 7), it was correlated with the somatic membrane potential (Supplementary Figure 1 A). I computed the spatial information score/ Place Score (PS), which indicated place tuning of the somatic membrane potential (Materials and Methods) for each of the 7 recording. One subicular pyramidal neuron showed significant place tuning of its membrane potential (Place Score: 0.0437 bits/s, 100th percentile of shuffled distribution, Supplementary Figure 1 B). Furthermore, the membrane potential recordings were

correlated with the animal's locomotion speed (Supplementary Figure 1 C), and a linear regression analysis revealed speed tuning of the somatic membrane potential (slope: 0.03 mV/(cm/s), p = 0.0002) in the same subicular pyramidal neuron which was also place-tuned (Supplementary Figure 1 D).

While it is already known that action potential firing of subicular neurons can be tuned to the spatial position and the animal’s movement speed (Sharp and Green, 1994; Ledergerber et al., 2021), it is still unclear to what extent the subthreshold synaptic input of a subicular neuron is correlated to these parameters. To directly investigate whether synaptic input of subicular pyramidal cells is tuned to spatial position and the locomotion speed of mice, the main set of experiments was performed in somatic voltage-clamp configuration. Following cell identification in current-clamp shortly after achieving whole cell configuration, the recording was switched to voltage clamp configuration (Figure 10) and whole cell membrane currents of subicular neurons, at a holding potential of -70 mV were measured while mice were freely moving on the circular track. For subsequent analysis, somatic membrane current recordings were processed using a Hilbert transform to enhance the signal-to-noise ratio. Then, each recording (n = 17) was correlated with the animal's position and movement speed.

First, whole-cell membrane current recordings were correlated to the circular position of the animal (Figure 10 A). For thus, the circular track was divided into spatial bins of 8 cm length and the average membrane current per bin was calculated. Subsequently, the spatial information score analysis showed that the somatic membrane currents were spatially tuned (Figure 10 B) in 4 out of 17 recordings (Figure 10 C).

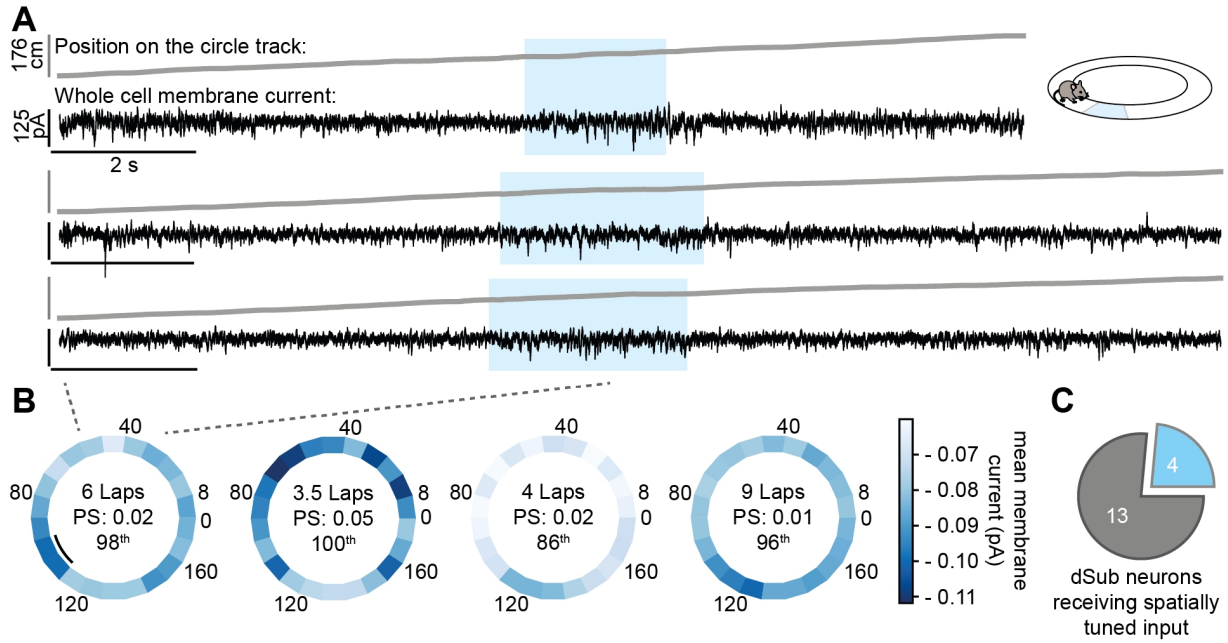

Figure 10: Cumulative input to subicular neurons is tuned to spatial locations

A: Representative raw somatic membrane current recording during freely moving behavior on a circular track showing membrane current (in black) synchronized to the animal's position (in grey) for three consecutive laps, taken from the first recording in B (indicated by dashed lines). Note the increased inward currents when the animals traverses a specific location (shaded in blue, B: black line). B: Color-coded mean membrane current over all laps for each spatial bin of the circular track. Center: Number of rounds, Place Score (PS) and the percentile of the Place Score in shuffled distribution. C: Spatially tuned input was detected in 4 out of 17 subicular neurons. Recordings provided by Dr. Kaneko.

Second, whole cell current clamp recordings were correlated to the animal's movement speed (Figure 11 A). For this, the animal's velocity was divided into 1 cm/s bins, and the average median current per bin was calculated. A linear regression analysis confirmed that the somatic membrane currents are correlated to the animal's velocity (Figure 11 B) in 4 out of 17 recordings (Figure 11 C).

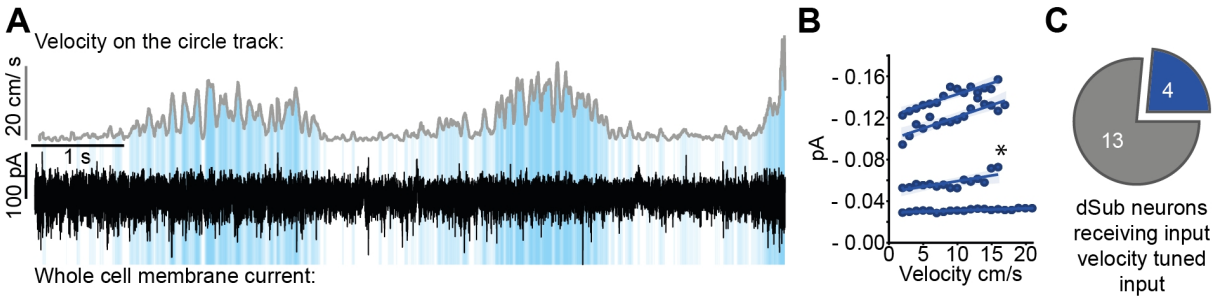

Figure 11: Cumulative input to subicular neurons is velocity tuned

A: Representative recording of raw somatic membrane currents during free behavior on a circular track showing membrane current (in black) correlated to the animal's movement speed (in grey). Blue shades indicate velocity bins with the same velocity. B: Median membrane current as function of the velocity bin. Linear regression identified four subicular neurons with membrane currents significantly ($p < 0.02$) correlated to the animal's movement speed (C). Recordings provided by Dr. Kaneko.

As shown above, somatic membrane currents of subicular neurons can be tuned to the animal's position in its environment as well as to the animal's movement speed. These tunings were observed in individual subicular neurons and did not overlap across individual neurons. Interestingly, exclusively the somatic membrane currents of bursting subicular neurons showed these tunings (Figure 12).

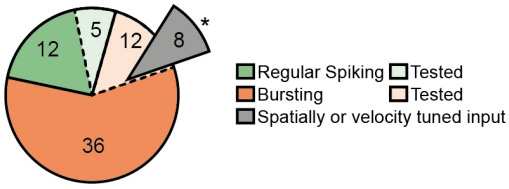

Figure 12: Cumulative input is tuned only in bursting subicular neurons

A: Numbers of electrophysiological cell types in the *in vivo* recordings. 65 subicular neurons were recorded. 17 of these neurons had a sufficient recording duration and spatial area coverage by the freely moving mice to allow for a deeper analysis of tuning parameters. All 8 subicular neurons with either spatially or velocity tuned input were identified as bursting neurons (Fisher's exact test, $p = 0.0294$).

3.2. VGluT2 is a molecular marker for bursting in dorsal subicular pyramidal neurons

Pyramidal neurons in the SUB exhibit two distinct action potential output modes: regular spiking and bursting, as corroborated by previous studies (Taube, 1993; Behr et al., 1996; Jarsky et al., 2008; Graves et al., 2012; Böhm et al., 2015; Cembrowski et al., 2018a). These modes were also observed in my *in vivo* electrophysiological recordings. Notably, place and speed tuning were exclusively identified in bursting subicular neurons. The distal part of the dorsal SUB is known to be rich in bursting pyramidal neurons (Cembrowski et al., 2018a). Moreover, both single-cell RNA sequencing and in-situ hybridization indicate VGluT2 as a molecular marker specific to the distal part of the dorsal SUB (Cembrowski and Spruston, 2019). Finally, previous findings (Wozny et al., 2018) linked bursting activity with VGluT2 expression. To confirm that VGluT2 is a molecuar marker for bursting in subicular neurons in our mice, I selectively expressed floxed tdTomato in VGluT2-positive neurons using AAV-mediated transduction in VGluT2-Cre mice, followed by visually guided patch clamp recordings of both VGluT2-positive and VGluT2-negative neurons in acute subicular slices (Figure 13 A). Each neuron underwent comprehensive electrophysiological profiling using both hyperpolarizing and depolarizing, sub- and supra-threshold step current injections (Figure 13 B).

3.2.1. Dorsal subicular neurons comprise two electrophysiological cell types *in vitro*

In vitro, I identified two distinct types of action potential firing in the pyramidal neurons of the dorsal SUB. The first type fired a single action potential upon stimulation with the minimum current required to elicit an action potential (rheobase stimulation, Figure 13 Ba). The second type exhibited two or more action potentials, which were superimposed on a depolarization hump (Figure 13 Bb). To verify these observations, I employed hierarchical clustering based on the electrophysiological parameters, which confirmed the division of firing types into two distinct electrophysiological classes. The clustering results revealed two separate clusters: Cluster one primarily consisted of regular spiking pyramidal neurons (Figure 13 C, D; green), while cluster two was predominantly made

up of bursting neurons (Number of APs RS: 1 (1, 1), Number of APs Burst: 2 (2, 3), Mann-Whitney U-Tests: $p < 0.0001$).

Notably, the differences between the two clusters extended beyond their firing waveforms. In terms of subthreshold parameters, bursting pyramidal neurons exhibited a lower input resistance (Input Resistance $_{Cluster\ 1}$: 80.1 (median) (64.0 (25^{th} percentile), 115,7(75^{th} percentile)) MOhm, Input Resistance $_{Cluster\ 2}$: 52.9 (43.4, 63.23) MOhm, Mann-Whitney U-Tests: $p < 0.0001$), a reduced membrane time constant ($\tau_{Cluster\ 1}$: 17.1 (12.2, 23.7) ms, $\tau_{Cluster\ 2}$: 12.6 (10.0, 20.7) ms, Mann-Whitney U-Tests: $p = 0.001$), and higher Sag indices in both hyperpolarizing (Hypo Sag Index $_{Cluster\ 1}$: 16.9 (14.1, 20.8) %, Hypo Sag Index $_{Cluster\ 2}$: 21.3 (16.6, 26.5) %, Mann-Whitney U-Tests: $p = 0.0001$) and depolarizing directions (Depo Sag Index $_{Cluster\ 1}$: 7.5 (-0.2, 15.6) %, Depo Sag Index $_{Cluster\ 2}$: 22.9 (15.2, 29.8) %, Mann-Whitney U-Tests: $p < 0.0001$). In addition, rebound hyperpolarisation after the stimulus offset was increased in bursting neurons (Rebound Index $_{Cluster\ 1}$: -5.4 (-2.7, -10.1) %, Rebound Index $_{Cluster\ 2}$: -15.3 (-9.3, -21.7) %, Mann-Whitney U-Tests: $p < 0.0001$).

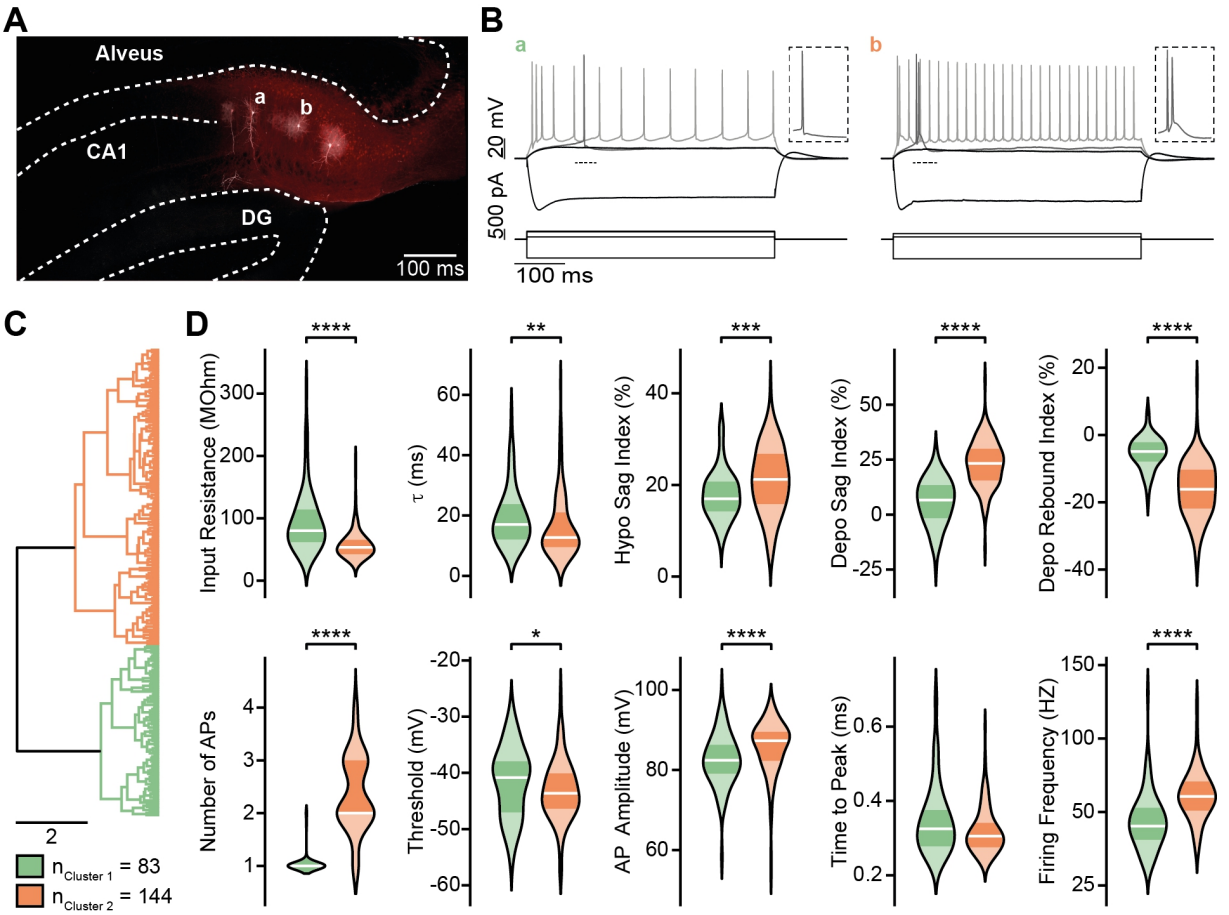

Figure 13: Electrophysiological cell types in the SUB *in vitro*

A: Confocal image of the dorsal SUB in a coronal slice. VGluT2+ neurons selectively expressed tdTomato (red). During whole-cell patch-clamp recordings neurons were filled with biocytin and later identified by streptavidin staining (white). B: Exemplary traces of subicular neurons from coronal slice in A. Action potential waveforms are highlighted in the dotted box. I identified two types of action potential firing in subicular pyramidal neurons, namely regular spiking (a) and bursting (b). C: Dendrogram of the hierarchical clustering on electrophysiological properties revealed two electrophysiological clusters (scale bar indicates squared Euclidian distance). D: The two electrophysiological cell types differ in subthreshold (input resistance $p < 0.0001$; τ $p = 0.0011$; hyperpolarization sag index $p = 0.0002$; depolarization sag index $p < 0.0001$; rebound index $p < 0.0001$) and suprathreshold (Number of action potentials $p < 0.0001$; Threshold $p = 0.0182$; Amplitude $p < 0.0001$; Time to Peak $p = 0.0281$; Firing Frequency $p < 0.0001$; Mann-Whitney U-Tests) properties. Note that cluster one only fires one action potential at rheobase stimulation and cluster two fires more than one action potential. n Cluster 1 = 83, n Cluster 2 = 144, Data represented as violin plot with median (white) and 25th to 75th percentile (shaded area). All data tested with Mann-Whitney U-Tests (*p<0.05, **p<0.01, ***p<0.001, ****p<0.0001).

Regarding suprathreshold parameters, bursting neurons showed a lower action potential threshold (Threshold $_{\text{Cluster 1}}$: -40.3 (-44.9, -37.8) mV, Threshold $_{\text{Cluster 2}}$: -44.3 (-46.8, -40.5) mV, Mann-Whitney U-Tests: $p = 0.0001$) and a higher action potential amplitude (Amplitude $_{\text{Cluster 1}}$: 82.3 (-79.1, 85.6) mV, Amplitude $_{\text{Cluster 2}}$: 87.9 (82.8, 90.0) mV, Mann-Whitney U-Tests: $p < 0.0001$). Both clusters did not differ in the time to peak (Time to Peak $_{\text{Cluster 1}}$: 0.32 (0.28, 0.37) ms, Time to Peak $_{\text{Cluster 2}}$: 0.31 (0.28, 0.34) ms, Mann-Whitney U-Tests: $p = 0.1767$). Furthermore, bursting neuron had a higher mean firing rate when stimulated with three times rheobase stimulation (Firing Frequency $_{\text{Cluster 1}}$: 44.9 (33.3, 55.2) Hz, Firing Frequency $_{\text{Cluster 2}}$: 60.3 (51.0, 70.7) Hz, Mann-Whitney U-Tests: $p < 0.0001$).

3.2.2. VGluT2 is a marker for bursting neurons of the SUB

To corroborate earlier findings (Wozny et al., 2018), which linked bursting activity with VGluT2 expression, I conducted an analysis of VGluT2 expression within the two electrophysiological clusters previously identified (Figure 14 A). This analysis demonstrated a significant disparity in VGluT2 expression between the two clusters (Fisher's exact test, $p = 0.0066$). Notably, the cluster comprising bursting neurons contained three times as many VGluT2$^+$ cells ($n_{\text{VGluT2}^+\text{ bursting}}$: 60 vs. $n_{\text{VGluT2}^+\text{ regular spiking}}$: 17; Figure 14 B). This finding suggests that VGluT2 expression is predominantly associated with bursting neurons in the dorsal SUB.

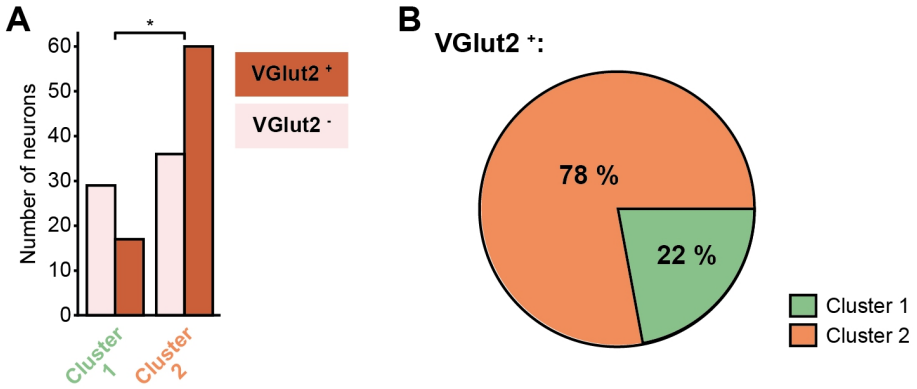

Figure 14: Distribution of VGluT2 on electrophysiological clusters

A: Distribution of VGluT2$^+$ neurons between electrophysiological clusters (Figure 13). Cluster 2

contains significantly more VGluT2$^+$ neurons (Fisher's exact test, p = 0.0066). B: Percentage of bursting (orange) and regular spiking (green) VGluT2$^+$ neurons.

Collectively, these findings demonstrate that subicular pyramidal neurons are comprised of two distinct electrophysiological clusters. Additionally, VGluT2 has emerged as a marker predominantly for the cluster containing bursting neurons. Consequently, the subsequent experiments were specifically focused on VGluT2-positive neurons in the dorsal SUB.

3.3. Hippocampal input separates in the dendritic tree of subicular pyramidal neurons

The two major hippocampal inputs to subicular neurons originate from the CA1 region and the EC. Histologically, the axons of both regions are intermingled in the SUB and do not present a clear separation in layers, like in the adjacent CA1 region (O'Mara et al., 2001; Bienkowski et al., 2018). Since synaptic position is one major factor in how information is integrated in neurons (DeBello et al., 2014), I wanted to understand the spatial organization of these two major input streams across the dendritic tree of subicular pyramidal neurons. To investigate the synaptic organization within subicular neurons, I applied CRACM (Petreanu et al., 2009; Morgenstern et al., 2016) at a subcellular level. This involved expressing the opsin Chronos in either the CA1 region or the EC using AAV-mediated transduction (Supplementary Figure 2). In acute subicular slices, I selectively activated synapses expressing Chronos from either CA1 or EC. This activation was performed using a laser spot arranged in a grid pattern, which spanned a 900 µm by 800 µm area, with each spot spaced 50 µm apart. Concurrently, I recorded postsynaptic potentials (PSPs) in a whole-cell current-clamp configuration (Materials and Methods, Figure 5).

My primary focus was on understanding the spatial organisation of glutamatergic synapses of CA1 and EC synapses in the dendrtic tree of subicular bursting pyramidal neurons. To exclusively capture excitatory monosynaptic potentials, I bath applied of TTX, 4-AP, as well as GABAergic blockers (SR-95531 and CGP-52432). Upon completion of the experiment, bath application of NBQX and DAP-5 confirmed the

glutamatergic nature of the previously recorded PSPs (Materials and Methods; Figure 5). Additionally, the initial electrophysiological profile allowed for focused examination of bursting subicular pyramidal neurons (Figure 15, bottom right). Biocytin filling was conducted during the recording, and subsequent morphological reconstruction of neurons confirmed the presence of an intact dendritic tree. I observed that excitatory synapses originating from area CA1 preferentially target the proximal regions of the dendritic arbor in subicular pyramidal neurons (Figure 15 A). In contrast, EC inputs seemed to specifically target distal regions of subicular pyramidal neuron dendritic trees (Figure 15 B).

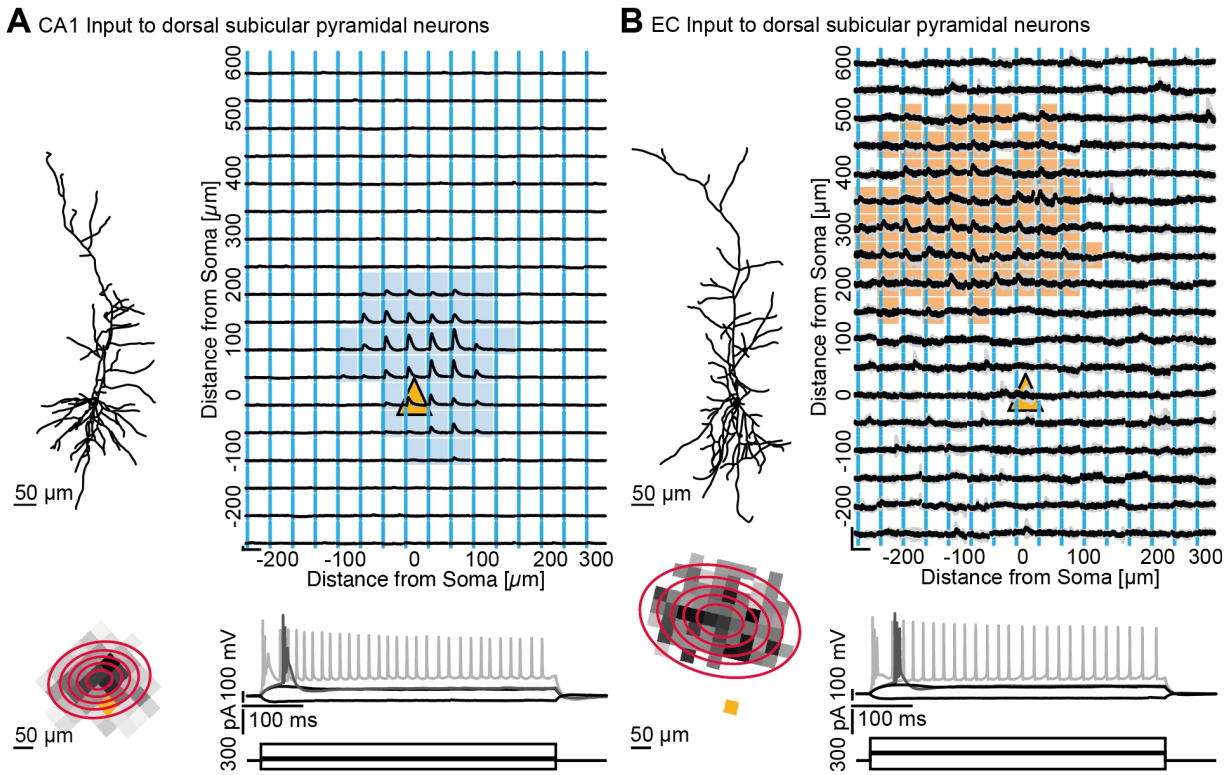

Figure 15: CA1 and EC synapses target distinct regions in the dendritic tree of subicular pyramidal neurons

Representative examples of CA1 (A) or EC (B) monosynaptic input maps onto individual dorsal subicular pyramidal neurons (right). Each sub-panel displays the average ± SD of somatic membrane potential from at least three simulations (stimulation time indicated by blue lines) in the same location (scale bar represents 0.5 mV and 50 ms). The sub-panels are arranged according to the stimulation distance from the soma (yellow triangle). Colored shadings indicate EPSPs at the respective

stimulation spot. Mapping experiments were carried out only on bursting subicular neurons after electrophysiological characterization (bottom right). Furthermore, recorded neurons were verified to have a complete dendritic tree using biocytin filling during the recording and post-hoc reconstruction (top left). Mean amplitude of the detected EPSPs were aligned to the stimulation spot (bottom left). The position of the soma is indicated as orange pixel. Then, a 2D Gaussian function (red circles) was fitted to the resulting image.

The consistency of this observation was further affirmed when aligning the input distributions (n CA1 Input = 8, n EC Input = 9) according to the primary trunk's direction, as described in Materials and Methods, and then superimposing them (Figure 16 A). Then, I averaged the normalized EPSP amplitude per row (Figure 16 B). The peak of EC input was located 250 µm away from the soma, whereas CA1 input was most pronounced in the vicinity of the soma (RM two-way ANOVA: Distance x Input Stream interaction, $F(17,255) = 13.41$, $p < 0.0001$; Sidak's multiple comparison test). This indicates that the synapses from both input streams target different areas of the subicular pyramidal dendritic tree. Additionally, I calculated the average normalized EPSP amplitude for each column (Figure 16 C). The EPSP amplitudes for both input streams overlapped and did not exhibit any horizontal separation (RM two-way ANOVA: Distance x Input Stream interaction, $F(15,255) = 0.92$, $p = 0.55$).

To corroborate this finding, I applied a 2-D Gaussian function to the amplitude maps for each subicular pyramidal neuron (Figure 16 A bottom left). The vertical displacement of these fit centers confirmed that EC input terminates more distally in the dendritic tree of subicular pyramidal neurons (Figure 16 E; CA1: 56 ± 41 µm vs. EC: 233 ± 66 µm; t-test: $p < 0.0001$). Moreover, monosynaptic EPSPs from CA1 were more vertically confined (Figure 16 G, CA1: 2.5 (2, 3) Bins vs. EC: 3 (3, 4) Bins; Mann-Whitney U-Test: $p < 0.0001$). The horizontal displacement of the fit centers (Figure 16 D; CA1: 39 ± 55 µm vs. EC: 44 ± 41 µm; t-test: $p = 0.8411$), as well as the horizontal scale (Figure 16 F, CA1: 2 (2, 3.25) Bins vs. EC: 3 (3, 4) Mann-Whitney U-Tests: $p = 0.1795$), were similar between both input streams. Collectively, these experiments reveal that, despite the absence of a laminar structure in the dorsal SUB, hippocampal input streams are spatially segregated within the dendritic tree of subicular pyramidal neurons.

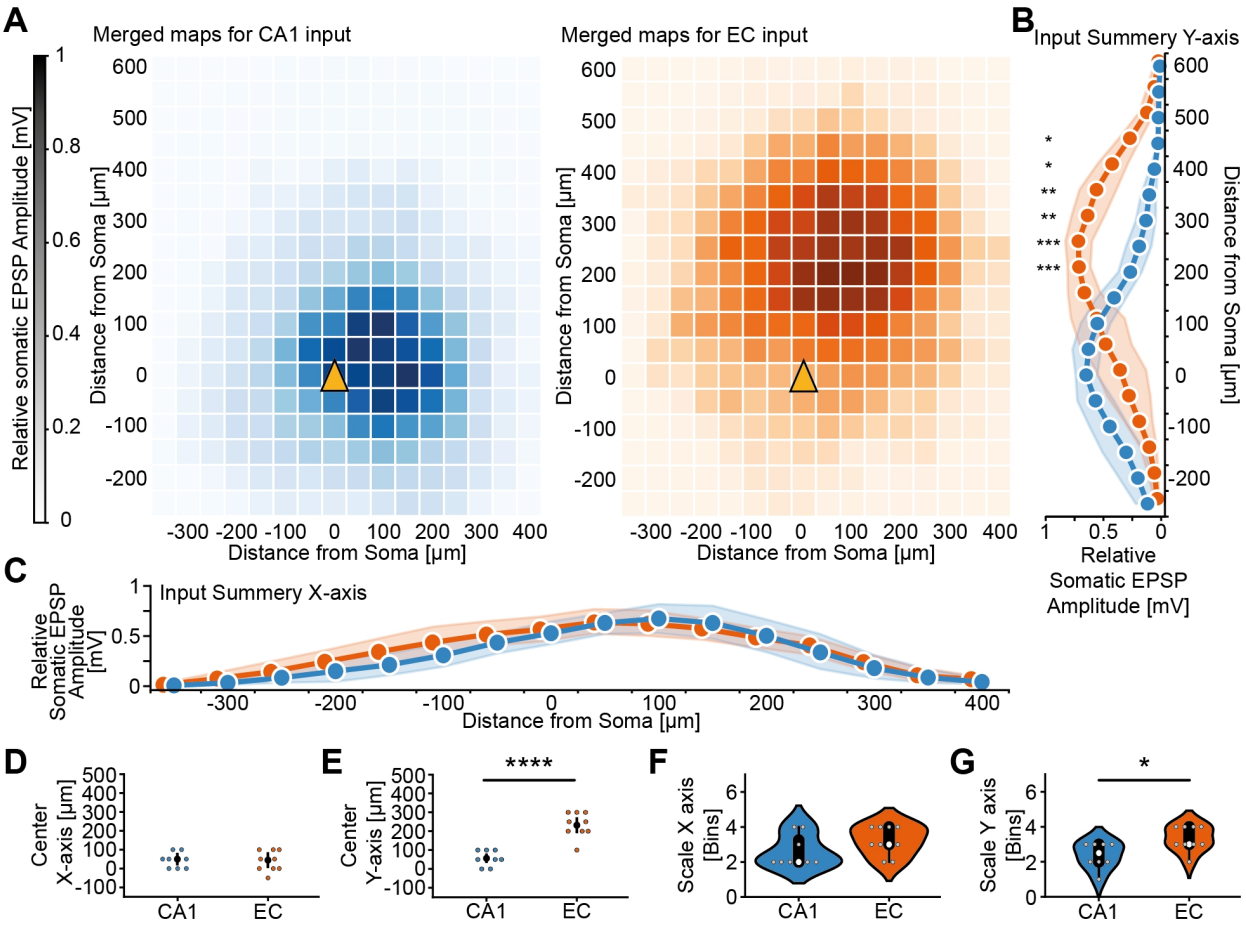

Figure 16: Input segregation in bursting dorsal subicular pyramidal neurons

A: Superimposed amplitude maps from CA1 (left, n = 8 input maps) and EC (right, n = 9 input maps) input to dorsal subicular neurons. Prior to merging, the input maps were aligned to the neuron's trunk orientation (Figure 5, Materials and Methods) and their amplitudes were normalized. B: Input summery in vertical direction. EPSP amplitudes were average for each row of the merged input maps. EC input was located more distally in subicular neurons (RM two-way ANOVA: Distance x Input Stream interaction, $F(17,255) = 13.41$, $p < 0.0001$; Sidak's multiple comparison test, * $p < 0.05$, ** $p < 0.01$, *** $p < 0.001$). C: Input summery in horizontal direction, EPSP amplitudes were average for each column of the merged input maps. Results showed no difference between both input streams (RM two-way ANOVA: Distance x Input Stream interaction, $F(15,255) = 0.92$, $p = 0.55$). D-G: The input maps of each recording were fitted with a 2-D Gaussian function. D: Center displacement in horizontal direction (x-axis) did not vary between the input streams (t-test, $p = 0.8411$). E: Center displacement of the 2-D Gaussian fit in vertical direction (y-axis) showed EC input located more distally in the dendritic tree of subicular pyramidal neurons (t-test: $p < 0.0001$). F: Scale of the 2-D Gaussian fit in horizontal direction did not differ between input streams (t-tests: $p = 0.1795$). G: Scale of the 2-D Gaussian fit in vertical direction indicated that EC input is more dispersed. (t-test: $p = 0.0157$).

3.4. Different contribution of CA1 and EC input streams to the tuning of subicular VGluT2$^+$ neurons

As demonstrated, dorsal subicular bursting neurons receive spatially tuned input. Additionally, both major input streams, namely CA1 and EC, consist of neurons whose output is spatially tuned (Brandon et al., 2014). Thus, I next investigated the contribution of these two major input streams to the output tuning of subicular neurons. To do this, I monitored the spatial and velocity tuned output of a population of dorsal subicular VGluT2$^+$ neurons with single-cell resolution, using two-photon imaging of GCaMP6s activity, while selectively inhibiting synaptic input from either CA1 or EC. For this, I injected the inhibitory DDREAD (hm4D(Gi)) either in CA1 or EC (Figure 6 A, Control: mCherry; Supplementary Figure 3). During the task, mice ran on a linear treadmill and received a food reward for each lap. Thirty minutes after the initial recording of subicular activity (Figure 6 middle), I locally reduced synaptic transmission in the SUB by applying the DREADD agonist clozapine N-oxide (CNO) through a miniature hole in the imaging window (Material and Methods, Figure 6). I tracked individual subicular VGluT2$^+$ neurons across both imaging sessions (Figure 17 A). This approach allowed me to directly compare the spatial and velocity tunings of individual subicular neurons both with and without selectively reduced inputs from CA1 and EC.

I was able to track 2879 subicular VGluT2$^+$ neurons across both imaging sessions. 1407 neurons were imaged from six mice under control conditions. For the control condition three mice each were injected with the structural marker mCherry in either CA1 or EC. Changes in place and velocity tunings for these neurons did not differ in regard to the location of the injections of the control virus (Supplementary Figure 4) so that these neurons were pooled together. 664 neurons were imaged from five mice injected with the inhibitory DREADD in CA1 and 808 neurons were imaged from six mice injected with the inhibitory DREADD in EC. To calculate the tunings of these cells, the raw $\Delta F/F$ had to be normalized, because the signal decreased between both imaging sessions (Figure 17 B, n = 1670 neurons, $\sum \Delta F/F_{\text{Pre CNO}}$ = 3260 (2588, 3904) vs. $\sum \Delta F/F_{\text{Post CNO}}$ = 3145 (2533, 3887); Wilcoxon signed rank test: $p < 0.0001$).

Animals were trained to run uniformly on the linear treadmill throughout the experiment

(Supplementary Figure 5). Therefore, the animals were overtrained and food restricted. I did not detect any difference in the animals' running behavior as indicated by the number of laps (Supplementary Figure 5 A) and the median velocity (Supplementary Figure 5 B) the animals ran between the two imaging sessions. In addition, the number of licks the animals performed during the imaging sessions was comparable (Supplementary Figure 5 C). However, the variance between the animals' behavior was large in the experiments, which might account for the absence of significant difference in the change of tuning parameters per animal (Supplementary Figure 6).

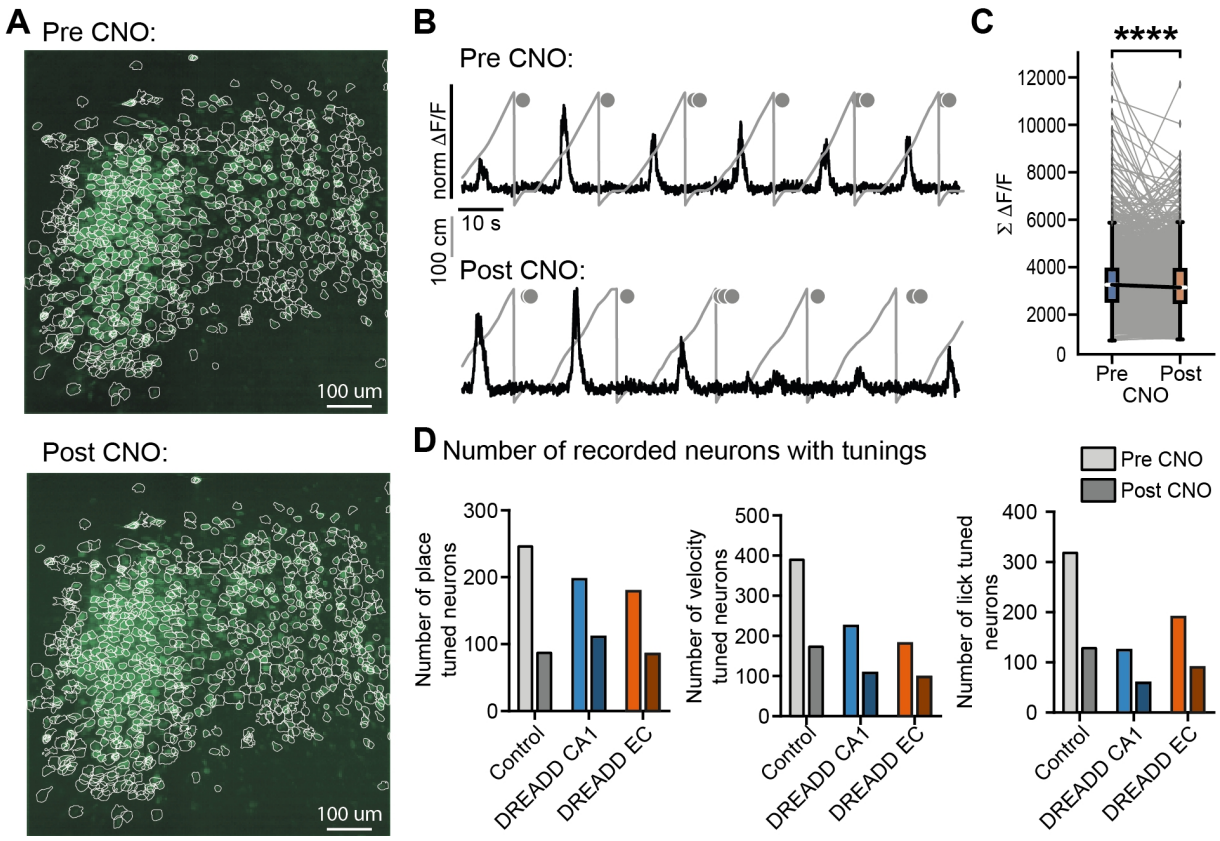

Figure 17: Two-photon calcium imaging of dorsal subicular VGluT2⁺ neurons

A: Maximum intensity projection of the first 100 imaging frames for Pre- and Post-CNO imaging. Single cell calcium activity extraction and cell-matching between Pre- and Post-CNO imaging (white lines) was performed using custom written scripts based on CaImAn (v1.6.2). B: Exemplary single-cell calcium activity (black lines) and the animal's position of the linear track (grey lines) for Pre- (up) and Post-CNO (bottom) imaging. In addition, the animal's licking behavior was recorded (grey dots). Single-cell calcium activity was correlated to the animal's position, velocity and licking behavior on the

linear track to quantify spatial tunings of VGluT2$^+$ dorsal subicular neurons. C: Sum of the ∆F/F activity for each recorded neuron that showed tuning to either place, locomotion velocity and/or lick behavior in the Pre-CNO condition. On average, the calcium activity decreased from the Pre- to the Post-CNO imaging (n = 1670 neurons, Wilcoxon signed rank test: $p < 0.0001$) . D: Overview of the tuned neurons in the Pre-CNO condition (light colors) and the remaining tuned neurons in the Post-CNO condition (dark colors). VGluT2$^+$ subicular neurons were tested for tuning to place (left), locomotion velocity (middle) and licking behavior (right).

3.4.1. CA1 and EC inputs for spatial tuning

Spatial tuning properties were quantified in two ways. Firstly, I calculated the spatial information score of subicular activity referred to as the 'Place Score' (Figure 18 A) from the average raw ∆F/F calcium activity per spatial bin over all laps the animal ran during a 10 minutes recording. An individual subicular neuron's output was considered spatially tuned if the Place Score exceeded the 95th percentile of the bootstrap distribution of Place Scores (see Material and Methods). A total of 248 subicular VGluT2+ neurons were initially found to be spatially tuned in the control condition (comprising pooled subicular VGluT2$^+$ neurons from three mice, each injected in either CA1 or EC; Supplementary Figure 4 A, B). Additionally, 199 subicular VGluT2$^+$ neurons in mice injected with the inhibitory DREADD in CA1 were spatially tuned at the beginning of the experiment. In mice injected with the inhibitory DREADD in EC, 179 subicular VGluT2$^+$ neurons were initially spatially tuned.

Thirty minutes post-application of CNO through the imaging window the number of neurons that were classified as spatially tuned decreased under all three conditions (Figure 17 D left). In addition, there was a decrease in the Place Score of subicular VGluT2$^+$ neurons (Figure 18 A right), as indicated by the diminished contrast between spatial bins with high and low calcium activity. This decrease in Place Score was observed in all three experimental groups (Figure 18 B; Control $_{Pre\ CNO}$: 0.07 (0.04, 0.15) bits/s vs. Control $_{Post\ CNO}$: 0.04 (0.01, 0.11) bits/s, DREADD CA1 $_{Pre\ CNO}$: 0.12 (0.07, 0.19) bits/s vs. DREADD CA1 $_{Post\ CNO}$: 0.07 (0.03, 0.13) bits/s, DREADD EC $_{Pre\ CNO}$: 0.1 (0.06, 0.16) bits/s vs. DREADD EC $_{Post\ CNO}$: 0.05 (0.02, 0.11) bits/s; RM two-way ANOVA: Pre/Post CNO x Experiment interaction, $F(2, 623) = 4.003$, $p = 0.0187$; Sidak's multiple comparison test Pre/Post CNO: Control: $p = 0.0090$, DREADD CA1: $p < 0.0001$,

DREADD EC: $p < 0.0001$). However, comparing the change in Place Score between the experimental groups and control group, the decrease in Place Score was greater when the input from CA1 and EC to subicular neurons was reduced (Figure 18 C; Δ Place Score $_{Control}$ -0.02 (-0.06, 0.01) bits/s vs. Δ Place Score $_{DREADD\ CA1}$ -0.05 (-0.11, 0.02) bits/s or Δ Place Score $_{DREADD\ EC}$ -0.04 (-0.09, 0) bits/s; Kruskal-Wallis test: $H(3,626) = 8.918$, $p = 0.0116$; Dunn's multiple comparisons test: Control vs. DREADD CA1: $p = 0.0174$, Control vs. DREADD EC: $p = 0.0310$). I further substantiated this observation using estimation statistics. For this, I calculated the median differences between the control condition and the application of the inhibitory DREADD in either CA1 or EC, across 5000 bootstrapped resamples (Figure 18 D). The median differences showed a significant decrease of the Place Score for both, CA1 and EC, input reductions (median difference between Δ Place Score $_{Control}$ and Δ Place Score $_{DREADD\ CA1}$: -0.0240 [95%CI -0.0354, -0.0127] two-sided permutation t-tests: $p = 0.0012$; median difference between Δ Place Score $_{Control}$ and Δ Place Score $_{DREADD\ EC}$: -0.0148 [95%CI -0.0285, -0.0018] two-sided permutation t-tests: $p = 0.0136$).

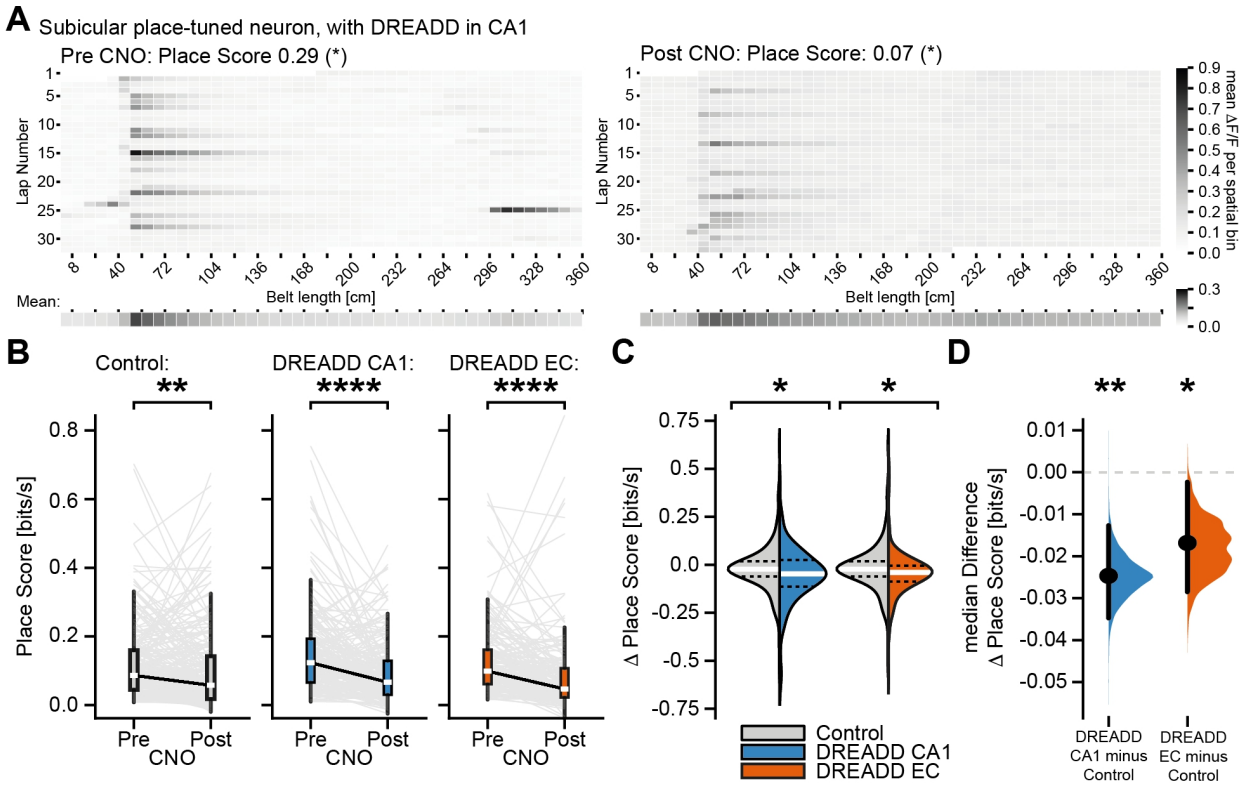

Figure 18: CA1 and EC input contribute to spatial information score in dorsal subicular VGluT2⁺ neurons

A: Exemplary color-coded mean calcium activity for one VGluT2⁺ subicular neuron spatial bin for all laps with CA1 input (Pre CNO, left) and with reduced CA1 input (Post CNO, right). Spatial bins were averaged over all laps the animal ran during the 10 minutes of recording. Spatial information score (Place Score) was calculated from the mean calcium activity per spatial bin over the whole recording. Note, that the contrast between bins with high and low calcium activity was decreased with reduced CA1 input leading to a smaller Place Score. B: Place Score of initially place tuned VGluT2⁺ subicular neurons with (Pre CNO) and with reduced (Post CNO) CA1 (middle, $n_{DREADD\ CA1}$: 199 neurons) or EC (right, $n_{DREADD\ EC}$: 179 neurons) input as well as the control condition (left, $n_{Control}$: 248 neurons). Place score decreased significantly, when either CA1 or EC input was chemo-genetically reduced ($F(2, 623) = 4.003$, $p = 0.0187$; Sidak's multiple comparison test Pre/Post CNO: Control: $p = 0.0090$, DREADD CA1: $p < 0.0001$, DREADD EC: $p < 0.0001$). C: Differences of Place Score between Pre and Post CNO for each recorded subicular VGluT2⁺ neuron comparing both input stream reductions to the control condition. Reduction in both inputs streams results in a significant decrease of the Place Score in subicular neurons (Kruskal-Wallis test: $H(3,626) = 8.918$, $p = 0.0116$; Dunn's multiple comparisons test: Control vs. DREADD CA1: $p = 0.0174$, Control vs. DREADD EC: $p = 0.0310$). D: Cumming estimation plot showing the median difference for the change in Place Score comparing both input stream reductions to the control condition for 5000 bootstrapped resamples (two-sided permutation t-tests: Dreadd CA1 minus Control: $p = 0.0012$, DREADD EC minus Control: $p = 0.0136$).

As an additional measure of place tuning in subicular neurons, the spatial vector strength, termed ‘Rho’, was calculated (Sharif et al., 2021). For this analysis, the calcium activity for each spatial bin was plotted radially (Figure 19 A), and the COM was determined (Materials and Methods). The length of the vector pointing to the COM was taken as Rho for all subicular VGluT2^{+} neurons that were considered spatially tuned from the Place Score analysis. Like the Place Score, Rho decreased 30 minutes after the application of CNO (Figure 19 B; Control $_{\text{Pre CNO}}$: 0.28 (0.13, 0.54) a.u. vs. Control $_{\text{Post CNO}}$: 0.20 (0.10, 0.46) a.u., DREADD CA1 $_{\text{Pre CNO}}$: 0.47 (0.26, 0.75) a.u. vs. DREADD CA1 $_{\text{Post CNO}}$: 0.26 (0.14, 0.59) a.u., DREADD EC $_{\text{Pre CNO}}$: 0.34 (0.17, 0.59) a.u. vs. DREADD EC $_{\text{Post CNO}}$: 0.21 (0.1, 0.39) a.u.; RM two-way ANOVA: Pre/Post CNO x Experiment interaction, $F(2, 623) = 3.477$, $p = 0.0315$; Sidak’s multiple comparison test Pre/Post CNO: Control: $p = 0.0364$, DREADD CA1: $p < 0.0001$, DREADD EC: $p = 0.0001$). Comparison of the reduction in Rho between the control condition and both experimental groups showed a significant decrease only when CA1 input was inhibited. (Figure 19 C; Δ Rho $_{\text{Control}}$ -0.05 (-0.22, 0.12) a.u. vs. Δ Rho $_{\text{DREADD CA1}}$ -0.14 (-0.36, 0.06) a.u. or Δ Rho $_{\text{DREADD EC}}$ -0.07 (-0.28, 0.06) a.u.; Kruskal-Wallis test: $H(3,626) = 9.248$, $p = 0.0098$; Dunn's multiple comparisons test: Control vs. DREADD CA1: $p = 0.0047$, Control vs. DREADD EC: $p = 0.3193$). Calculating the median difference between Control and both experimental groups for 5000 bootstrapped resamples (Figure 19 D) confirmed, that only a chemo-gentic inactivation of CA1 input resulted in a marked decrease of Rho (median difference between Δ Rho $_{\text{Control}}$ and Δ Rho $_{\text{DREADD CA1}}$: -0.0910 [95%CI -0.1536, -0.0375] two-sided permutation t-tests: $p = 0.0012$; median difference between Δ Rho $_{\text{Control}}$ and Δ Rho $_{\text{DREADD EC}}$: -0.0181 [95%CI -0.0706, 0.0217] two-sided permutation t-tests: $p = 0.267$).

Collectively, these findings indicate that local chemogenetic inactivation of CA1 or EC inputs had distinct effects on the spatial tuning of subicular VGluT2^{+} neurons. Diminishing CA1 inputs to subicular neurons led to reductions of both Place Score and Rho, whereas diminishing EC inputs resulted only in a decrease of Place Score.

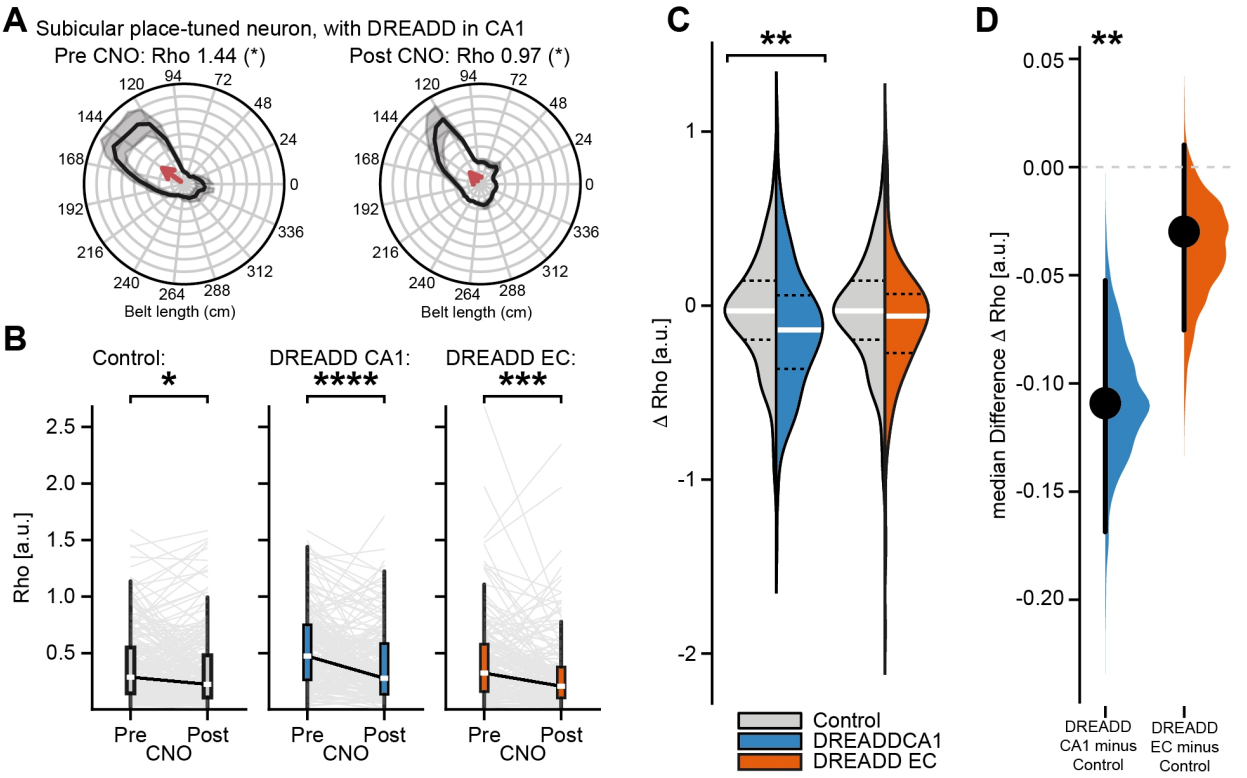

Figure 19: CA1 input contributes to spatial vector strength in dorsal subicular neurons

A: Mean and SD of radially plotted mean calcium activity per bin. The length of the vector pointing to the center of mass (red arrow) was calculated as spatial vector strength Rho. A right: Upon reduction of CA1 input the subicular VGluT2⁺ neuron still classified as spatially tuned although Rho decreased. B: Rho of initially place tuned VGluT2⁺ subicular neurons with (Pre CNO) and with reduced (Post CNO) CA1 (middle, $n_{DREADD\ CA1}$: 199 neurons) or EC (right, $n_{DREADD\ EC}$: 179 neurons) input as well as the control condition ($n_{Control}$: 248 neurons). Rho decreased significantly, compared between Pre and Post CNO (RM two-way ANOVA: Pre/Post CNO x Experiment interaction, $F(2, 623) = 3.477$, $p = 0.0315$; Sidak's multiple comparison test Pre/Post CNO: Control: $p = 0.0364$, DREADD CA1: $p < 0.0001$, DREADD EC: $p = 0.0001$). C: Differences of Rho between Pre and Post CNO for each recorded subicular VGluT2⁺ neuron, comparing both input stream reductions to the control condition. Only the reduction in the CA1 inputs stream results in a significant decrease of Rho in subicular neurons (Kruskal-Wallis test: $H(3,626) = 9.248$, $p = 0.0098$; Dunn's multiple comparisons test: Control vs. DREADD CA1: $p = 0.0047$, Control vs. DREADD EC: $p = 0.3193$). D: Cumming estimation plot showing the median difference for the change in Rho comparing both input stream reductions to the control condition for 5000 bootstrapped resamples with 95% confidence interval (two-sided permutation t-tests: DREADD CA1 minus Control: $p = 0.0012$, DREADD EC minus Control: $p = 0.267$).

3.4.2. CA1 and EC input for velocity tuning

Velocity tuning in subicular neurons was assessed through a linear regression analysis

of velocity-binned (1 cm/s bin) mean calcium activity for each subicular VGluT2$^+$ neuron. The slope of this regression served as an indicator of the neurons' velocity tuning strength (Figure 20 A). In control animals, 390 VGluT2$^+$ subicular neurons exhibited significant velocity tuning (comprising pooled subicular VGluT2$^+$ neurons from three mice, each injected in either CA1 or EC; Supplementary Figure 4 C). Additionally, among animals injected with the inhibitory DREADD in CA1 and EC, velocity tuning was observed in 228 and 181 VGluT2$^+$ subicular neurons, respectively. Thirty minutes after CNO application, there was a decrease in velocity tuning in subicular VGluT2$^+$ neurons across all conditions (Figure 20 B; Control$_{\text{Pre CNO}}$: 0.13 (0.07, 0.21) 10^{-3} (ΔF/F)/(cm/s) vs. Control$_{\text{Post CNO}}$: 0.04 (-0.05, 0.15) 10^{-3} (ΔF/F)/(cm/s), DREADD CA1$_{\text{Pre CNO}}$: 0.19 (0.12, 0.3) 10^{-3} (ΔF/F)/(cm/s) vs. DREADD CA1$_{\text{Post CNO}}$: 0.07 (-0.09, 0.2) 10^{-3} (ΔF/F)/(cm/s), DREADD EC$_{\text{Pre CNO}}$: 0.17 (0.1, 0.3) 10^{-3} (ΔF/F)/(cm/s) vs. DREADD EC$_{\text{Post CNO}}$: 0.06 (-0.04, 0.16) 10^{-3} (ΔF/F)/(cm/s); RM two-way ANOVA: Pre/Post CNO x Experiment interaction, $F(2, 662) = 5.127$, $p = 0.0062$; Sidak's multiple comparison test Pre/Post CNO: All: $p < 0.0001$). However, when comparing changes in velocity tuning, it was evident that the decrease in animals injected with inhibitory DREADD in CA1 was more pronounced than that in the control condition (Figure 20 C; Δ Velocity correlation $_{\text{Control}}$ -0.1 (-0.2, 0) 10^{-3} (ΔF/F)/(cm/s) vs. Δ Velocity correlation $_{\text{DREADD CA1}}$ -0.16 (-0.33, 0) 10^{-3} (ΔF/F)/(cm/s) or Δ Velocity correlation $_{\text{DREADD EC}}$ -0.11 (-0.29, 0.01) 10^{-3} (ΔF/F)/(cm/s); Kruskal-Wallis test: $H(3,799) = 13.25$, $p = 0.0013$; Dunn's multiple comparisons test: Control vs. DREADD CA1: $p = 0.0006$, Control vs. DREADD EC: $p = 0.1700$). Calculating the median differences between the Control and both experimental groups across 5000 bootstrapped resamples (Figure 20 D) confirmed that only chemogenetic inactivation of CA1 input led to a significant decrease in velocity tuning (median difference between Δ Velocity correlation $_{\text{Control}}$ and Δ Velocity correlation $_{\text{DREADD CA1}}$: -0.0006 [95%CI -0.0011, -0.0002] two-sided permutation t-tests: $p = 0.0002$; median difference between Δ Velocity correlation $_{\text{Control}}$ and Δ Velocity correlation $_{\text{DREADD EC}}$: -0.0001 [95%CI -0.0005, 0.0001] two-sided permutation t-tests: $p = 0.2172$). Taken together, these results demonstrate, that only a reduction of CA1 input lead to a reduced velocity tuning of VGluT2$^+$ subicular neurons.

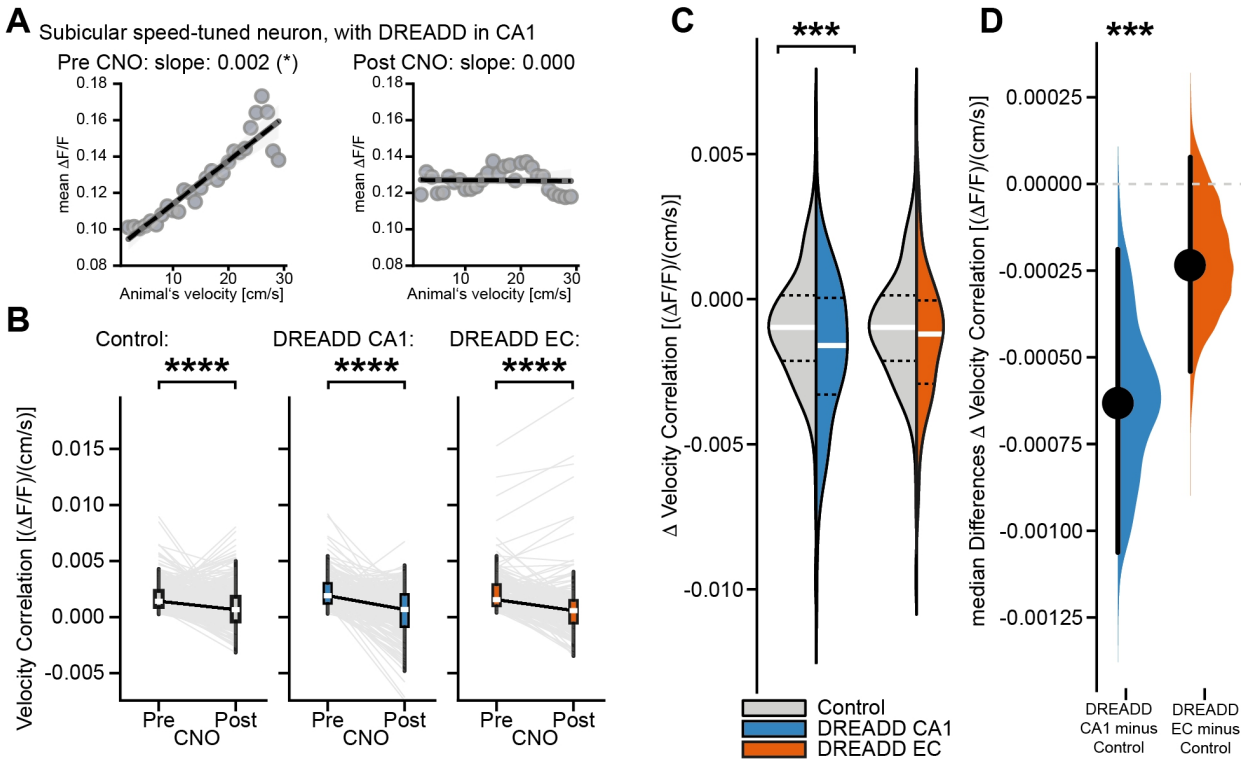

Figure 20: CA1 input contributes to the speed tuning of dorsal subicular neurons

A: Exemplary mean calcium activity per 1 cm/s velocity bin for initially speed tuned VGluT2⁺ subicular neuron Regression analysis showed significant velocity correlation (left) that is lost upon reduction of CA1 input (right). B: Slope of the velocity correlation of initially speed tuned VGluT2⁺ subicular neurons with (Pre CNO) and with reduced (Post CNO) CA1 (middle, $n_{DREADD\ CA1}$: 228 neurons) or EC (right, $n_{DREADD\ EC}$: 181 neurons) input as well as the control condition ($n_{Control}$: 390 neurons). Slope of the velocity correlation decreased significantly, when either CA1 or EC input was chemo-genetically reduced (RM two-way ANOVA: Pre/Post CNO x Experiment interaction, $F(2, 662) = 5.127$, $p = 0.0062$; Sidak's multiple comparison test Pre/Post CNO: All: $p < 0.0001$) as well as in the control condition. C: Differences of the slope of the velocity correlation between Pre and Post CNO for each recorded subicular VGluT2⁺ neuron comparing both input stream reductions to the control condition. Only the reduction in the CA1 inputs stream results in a significant decrease of the slopes of the velocity correlation in subicular neurons (Kruskal-Wallis test: $H(3,799) = 13.25$, $p = 0.0013$; Dunn's multiple comparisons test: Control vs. DREADD CA1: $p = 0.0006$, Control vs. DREADD EC: $p = 0.1700$). D: Cumming estimation plot showing the median difference for the change in the slope of the velocity correlation comparing both input stream reductions to the control condition for 5000 bootstrapped resamples with 95% confidence interval (two-sided permutation t-tests: DREADD CA1 minus Control: $p = 0.0002$, DREADD EC minus Control: $p = 0.2172$).

3.4.3. CA1 and EC input for lick tuning

To quantify whether or not subicular VGluT2$^+$ neurons are tuned to the animals' licking behavior (Gauthier and Tank, 2018), I calculated a Lick Idx, as difference between median calcium activity in time points were the animal licked and at time points were the animal did not lick. Thus, a higher significant Lick Idx indicates more calcium activity, when the animal licks (Materials and Methods, Figure 21 A). In the initial, Pre-CNO imaging I was able to observe lick tuning in 316 subicular VGluT2$^+$ neurons in control condition. Furthermore, 127 and 190 subicular VGluT2$^+$ neurons were initially lick-tuned from animals with inhibitory DREADD injection in either CA1 or EC, respectively. Overall, decrease in lick tuning was observed in subicular VGluT2$^+$ neurons in all conditions after 30 minutes of CNO application. (Figure 21 B; $Control_{Pre\ CNO}$: 0.14 (0.09, 0.27) log(ΔF/F) vs. $Control_{Post\ CNO}$: 0.07 (0, 0.16) log(ΔF/F), DREADD $CA1_{Pre\ CNO}$: 0.13 (0.08, 0.22) log(ΔF/F) vs. DREADD $CA1_{Post\ CNO}$: 0.08 (0, 0.23) log(ΔF/F), DREADD $EC_{Pre\ CNO}$: 0.17 (0.12, 0.28) log(ΔF/F) vs. DREADD $EC_{Post\ CNO}$: 0.1 (0.01, 0.19) log(ΔF/F); RM two-way ANOVA: Pre/Post CNO x Experiment interaction, $F(2, 570) = 3.724$, $p = 0.0247$, Sidak's multiple comparison test Pre/Post CNO: Control: $p < 0.0001$, DREADD CA1: $p = 0.0469$, DREADD EC: $p < 0.0001$). However, these changes in lick tuning did not differ from the control condition (Figure 21 C; Δ Lick $Idx_{Control}$ -0.08 (-0.18, 0) log(ΔF/F) vs. Δ Lick $Idx_{DREADD\ CA1}$ -0.06 (-0.17, 0.07) log(ΔF/F) or Δ Lick $Idx_{DREADD\ EC}$ -0.1 (-0.2, 0.01) log(ΔF/F); Kruskal-Wallis test: $H(3,633) = 4.008$, $p = 0.1348$), further strengthened by estimation statistics (Figure 21 D, median difference between Δ Lick $Idx_{Control}$ and Δ Lick $Idx_{DREADD\ CA1}$: 0.0232 [95%CI -0.0162, -0.0738] two-sided permutation t-tests: $p = 0.2308$; median difference between Δ Lick $Idx_{Control}$ and Δ Lick $Idx_{DREADD\ EC}$: -0.02 [95%CI -0.0525, 0.0195] two-sided permutation t-tests: $p = 0.3172$). I conclude that in the experiments presented, lick tuning is not effected by either reducing CA1 or EC input to dorsal subicular VGluT2$^+$ neurons.

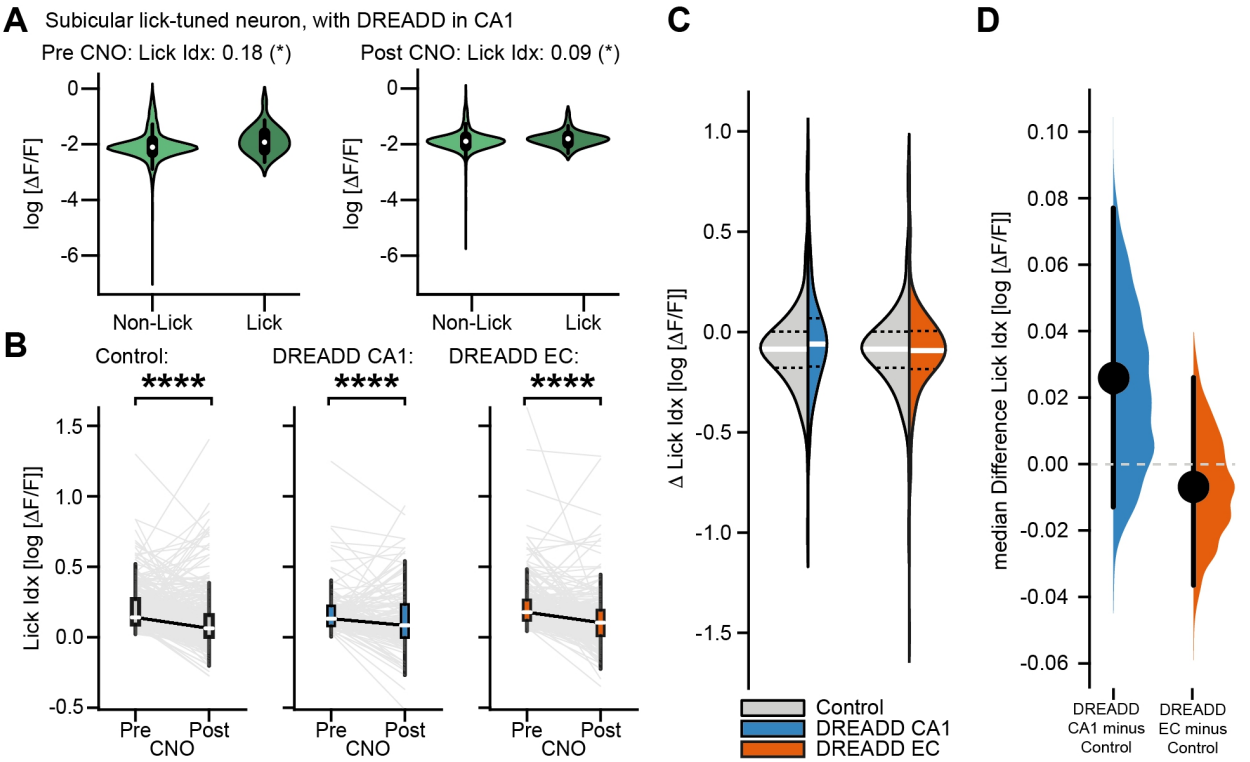

Figure 21: CA1 and EC input do not contribute the lick tuning of dorsal subicular neurons

A: Exemplary quantification of lick tuning for VGluT2⁺ subicular neuron for the initial imaging (Pre CNO, left) and the imaging 30 minutes after CNO application (Post CNO, right). Calcium values were plotted on a logarithmic scale for time points where the animal licked and time points where the animal did not lick (non-lick). The lick index quantifies the median difference between Calcium values in both situations (Materials and Methods). B: Decrease in Lick Idx for the control (n = 316 neurons) and both experimental groups ($n_{DREADD\ CA1}$ = 127 neurons, $n_{DREADD\ EC}$ = 190 neurons; RM two-way ANOVA: Pre/Post CNO x Experiment interaction, $F(2, 570) = 3.724$, $p = 0.0247$, Sidak's multiple comparison test Pre/Post CNO: Control: $p < 0.0001$, DREADD CA1: $p = 0.0469$, DREADD EC: $p < 0.0001$). C: Changes in Lick Idx between both experimental group and the control group does not show any difference (Kruskal-Wallis test: $H(3,633) = 4.008$, $p = 0.1348$). D: Cumming estimation plot showing the median difference for the change in the Lick Idx comparing both input stream reductions to the control condition for 5000 bootstrapped resamples with 95% confidence interval (two-sided permutation t-tests: DREADD CA1 minus Control: $p = 0.2308$, DREADD EC minus Control: $p = 0.3172$).

In conclusion, the findings from these experiments reveal that while chemogenetic inactivation of CA1 input significantly affects both the spatial and velocity tuning of subicular VGluT2⁺ neurons, the inhibition of EC input predominantly impacts only the

spatial tuning, highlighting the distinct and specific contributions of these hippocampal inputs to the functional dynamics of subicular neurons.

4. Discussion

As the central hub for hippocampal information processing, the SUB transforms spatially and non-spatially correlated inputs from the trisynaptic loop and other hipocampal and non-hippocampal areas into spatially tuned outputs. Subicular neurons thus compress the internal representation of the animal's environment and distribute this representation to cortical and subcortical regions as well as back to the EC. In this work, I investigated the input/output transformation of spatially tuned input to dorsal subicular neurons and elucidated the distinct contributions of CA1 and EC inputs to their spatial tuning. Specifically,

1) I demonstrated that bursting subicular neurons receive spatially- and velocity-tuned excitatory synaptic inputs during spatial navigation;

2) I confirmed earlier findings (Wozny et al., 2018) that VGluT2 serves as a molecular marker for bursting subicular neurons in our mouse line;

3) I revealed that the synapses of the two major hippocampal input streams, namely CA1 and EC, segregate in the dendritic tree of VGluT2$^+$, bursting subicular neurons;

4) I discovered that these two major hippocampal input streams differentially contribute to the spatial tuning of VGluT2$^+$ subicular neurons.

4.1. The cumulative input to dorsal subicular neurons is spatially tuned

Many neurons in the hippocampal formation show action potential output tuned to environmental properties or the animal's movement through its environment (Leutgeb et al., 2005; Moser et al., 2008; Brandon et al., 2014). As part of the hippocampal formation it seems likely that subicular neurons receive spatially tuned input from other neurons. This has only recently been shown for input of CA1 neurons using *in vivo* two-photon imaging of a postsynaptically expressed glutamate sensor (Adoff et al., 2021).

In the current study, whole-cell patch clamp recordings of subicular neurons were performed while mice navigated freely on an elevated circle. These recordings

demonstrated that somatic membrane currents of subicular neurons are tuned to the animal's position in its environment and to its locomotion speed. During the recordings, voltage clamp mode was utilized to prevent neurons from generating action potential output. As a result, the additional inward currents that are responsible for the tuning of the somatic membrane currents originated most likely from the cumulative synaptic input delivered through the dendritic tree towards the soma. Indeed, postsynaptic inward currents characterized by a sharp onset and an exponential decay were visible in the recordings (Figure 8 B)

4.1.1. Input detection in somatic voltage clamp recordings

Input tuning in CA1 pyramidal neurons was previously inferred from *in vivo* whole-cell current clamp recordings (Harvey et al., 2009; Epsztein et al., 2011). In these studies, mice navigated a linear treadmill while CA1 membrane potential was recorded. Their findings suggested that subthreshold membrane potential levels increase within the spatially tuned CA1 pyramidal cell's place field, indicating synaptic input (along with dendritic non-linearities) as a source of this subthreshold depolarization. Indeed, I observed this increase in subthreshold membrane potential in a spatially tuned subicular neuron measured in current clamp mode (Supplementary Figure 1). However, these recordings included action potential output. Action potentials were a confounding element in this case, as they are the result of regenerative activity. Since my focus was solely on input tuning the primary set of experiments was conducted in voltage clamp mode.

Whole-cell voltage clamp recordings have been used in other brain areas to identify input tuning of individual neurons (Tan et al., 2004; Arenz et al., 2008). In these recordings, control over the membrane potential was optimal at the soma. By maintaining a holding potential of -70 mV and using intracellular application of the sodium channel blocker QX-314, action potential firing was effectively prevented during recording, thus segregating input from output. However, control of the dendritic membrane potential via voltage clamping is less effective due to space clamp problems (Williams and Mitchell, 2008). Space clamp problems arise from of the neuron's morphology, because the current injected to maintain the holding potential decays over distance. Consequently, currents recorded at the soma are the sum of local somatic

currents and axial currents from dendritic locations with differing membrane potentials (Bar-Yehuda and Korngreen, 2008). Thus, the influence of dendritic voltage-gated ion channels, which could enhance or suppress dendritic postsynaptic currents at the soma, cannot be ruled out. Nonetheless, the overall current reaching the soma was spatially tuned.

Additionally, dendritic morphology influences the axial currents that reach the soma. Postsynaptic currents traversing the dendritic tree undergo passive electrical attenuation and filtering. Given the strong voltage attenuation observed along the apical dendritic tree of pyramidal neurons (Spruston, 2008), the contribution of distal dendritic input to the somatic voltage may be minimal and might not be detectable (Williams and Stuart, 2002). Modeling studies suggest a 50% decrease in synaptic potentials over approximately 250 µm in CA1 pyramidal neurons (Spruston et al., 1994; Golding et al., 2005). Therefore, the contribution of apical dendritic synaptic conductances originating from EC is expected to be small, unless dendritic non-linearities cause stronger dendritic depolarization that do not escape somatic detection. My experiments in acute slices (CRACM) detected distal dendritic inputs with the highest density around 250 µm from the soma, implying a small but detectable contribution of distal dendritic (presumably EC) input. I conclude that the presented *in vivo* recordings include spatially tuned input from CA1 and underestimated the input from EC. The pathway-specific reduction experiments using DREADDs further support the contribution of EC input to cellular tuning properties.

4.1.2. Origin of spatially and movement speed tuned inputs to dorsal subicular neurons

I was able to directly detect spatial tuning in the cumulative synaptic inputs of dorsal subicular pyramidal neurons. There are two possible mechanisms for this tuning of the cumulative synaptic input: either there is an over-representation of spatial or speed-related synaptic input, or there is a postsynaptic modulation by voltage gated ion channels of specific inputs that tunes the whole postsynaptic membrane potential to a particular location or to the speed of the animal's movement.

An over-representation of spatial tuning in dorsal subicular pyramidal neurons could be

mediated by a non-equal distribution of CA1 place cells tuned to a specific location. Input tuning of dorsal subicular neurons would result from an increased number of excitatory synapses that are tuned to a specific place in the animal's environment. Indeed, over-representation of spatial locations in the CA1 place cell population was described for reward locations (Gauthier and Tank, 2018), task-related locations (Hollup et al., 2001) and other landmarks (Sato et al., 2020). In this case, a pyramidal neuron in the dorsal SUB passively collects the tuning of the CA1 region. The spatial tuning of subicular neurons would result from the number of presynaptically connected CA1 neurons that are tuned to a specific place in the animal's environment or the animals movement speed. Thus, subicular neurons' spatial tuning would represent the spatial population code of a presynaptic neuronal ensemble of CA1 spatial tunings.

Another potential mechanism for the tuning of cumulative input in dorsal subicular pyramidal neurons involves postsynaptic plasticity and amplification or suppression by voltage-gated ion-channels. Voltage-gated ion channels within the postsynaptic neuron's dendritic tree can modify the impact of a given synaptic input, potentially enhancing or suppressing individual postsynaptic potentials. Furthermore, plasticity processes within the dendritic tree can change the strength of synapses relative to the somatic membrane potential (Remy and Spruston, 2007). Dorsal subicular neurons are known to respond to their input through LTP and LTD of their synapses (Behr et al., 2009), thereby directly linking individual synaptic weights to the neuron's output. Consequently, synaptic plasticity is likely to augment synaptic input that coincides with the place-tuned activity of dorsal subicular neurons, thus reinforcing the tuning of the cumulative input in these neurons. It is noteworthy that synaptic plasticity in dorsal subicular neurons seems to vary depending on the presynaptic partner. CA1-SUB synapses demonstrate a presynaptic form of LTP that relies on N-methyl-D-aspartate (NMDA) receptors (Wozny et al., 2008), whereas EC-SUB synapses show a high threshold, NMDA- and calcium-dependent form of LTP (Fidzinski et al., 2011). Notably, the conditions for LTP at EC synapses align with those involved in behavioral time-scale plasticity. This form of synaptic plasticity, recently identified in CA1 pyramidal neurons, is driven by prolonged dendritic voltage signals and a substantial influx of Ca^{2+} ions, leading to a Ca^{2+} plateau potential in the dendritic tuft region of these neurons (Bittner et al., 2017; Grienberger and Magee, 2022). Future research should investigate whether behavioral time-scale

plasticity also occurs in subicular pyramidal neurons.

The most likely explanation for the observed tuning of the cumulative input in dorsal subicular pyramidal neurons is a combination of both mechanisms. First, dorsal subicular neurons receive input from neuronal ensembles of different input streams. They respond and modulate this input through dendritic voltage-gated channels and/or synaptic plasticity, ultimately altering the synaptic strength within their presynaptic neuronal ensemble. The weights of the presynaptic neuronal ensembles can change by the strengthening and weakening of individual synapses, leading to a consistent tuning of synaptic input in dorsal subicular neurons. Additionally, the presynaptic neuronal ensemble can change through multiple iterations of synaptic formation and pruning (Sheffield and Dombeck, 2019), leading to varying tunings of subicular pyramidal neurons.

4.2. CA1 and EC inputs contribution to the tuning of dorsal subicular neurons

I demonstrated that the cumulative input in dorsal subicular neurons is tuned both to the animal's position in its environment and to the animal's locomotion speed. Furthermore, the two major hippocampal input paths to dorsal subicular pyramidal neurons originate from CA1 and the EC (Gigg et al., 2000; Cappaert et al., 2007). Both regions show action potential output which is tuned to various aspects of the animal's spatial navigation. Dendritic synaptic integration of subicular neurons *in vivo* is poorly understood. The anatomical segregation of these input regions presents a unique opportunity to understand the basic principles of synaptic integration during the animal's behavior by investigating the contribution of each input path to the output tuning of dorsal subicular neurons. I selectively reduced either CA1 or EC input by chemogenetic inactivation of their specific synapses while assessing the tuning of subicular neurons using *in vivo* two-photon calcium imaging as mice were running on a linear treadmill.

4.2.1. Spatial precision of DREADD-mediated pathway reduction

Previous studies have investigated the separate contributions of different inputs to the spatial tuning of postsynaptic hippocampal neurons, focusing particularly on CA1

pyramidal neurons. In this context, various types of lesions were performed on either CA3 (Brun et al., 2002) or EC (Van Cauter et al., 2008; Schlesiger et al., 2015), and the resulting neuronal activity in CA1 was correlated with the animal's spatial navigation. However, it is important to note that lesioning an entire subregion of the hippocampal formation may alter the overall hippocampal information processing. This is especially true when the EC is lesioned, impacting both the tri-synaptic and monosynaptic pathways to CA1 neurons. Consequently, differentiating the effects of both pathways on spatial tuning in CA1 neurons becomes challenging.

The development of genetically encoded opsins has mitigated these limitations. For example, by viral transduction of an inhibitory opsin in CA3, neuronal activity in their axons and synapses can be precisely reduced using spatially targeted laser light at the CA1 target area (Davoudi and Foster, 2019). Another approach involves the use of a retrograde virus infection strategy to express an inhibitory opsin exclusively in the subset of EC neurons projecting to CA1. Consequently, only EC neurons projecting to CA1 were inhibited when laser light was applied to the EC, minimizing -but not fully excluding- the effect on overall EC activity (Grienberger and Magee, 2022).

To address these challenges, my study investigated the contributions of CA1 and EC to the spatial tuning of subicular neurons using a chemogenetic approach. For target specificity, I stereotactically injected the DREADD virus into either CA1 or EC. After viral transduction, axons and synapses in the targeted region express the DREADD receptor, which inhibits presynaptic neurotransmitter release (Stachniak et al., 2014; Vardy et al., 2015) by activating intracellular Gi/o signaling pathways (Roth, 2016). The agonist CNO activates the DREADD receptor. This activation was further constrained by micro-infusion (Mahler et al., 2014; Stachniak et al., 2014; Gremel et al., 2016; Franklin et al., 2017; Ye et al., 2017) of CNO through a miniaturized hole in the imaging window. Consequently, this approach specifically and selectively silenced the terminal projections of CA1 or EC within the SUB, with minimal impact on the activity of the input region or its synapses in other brain areas.

In addition to location specificity, another advantage of the DREADD approach is its relatively precise timing. The activation of the inhibitory DREADD receptor by CNO leads to a reduction in synaptic transmitter release within minutes to an hour. In the

study presented, CNO was administered after initially imaging VGluT2$^+$ subicular neurons. Then, CNO was given 30 minutes to activate the inhibitory DREADD receptor (Yamawaki et al., 2019), followed by another round of imaging. During this 30-minute period, the animal remained under the microscope where it was able to run on the treadmill. This approach allowed for a direct comparison of the tuning of individual VGluT2$^+$ subicular neurons between conditions of intact and reduced input.

An alternative method for synaptic silencing would have been optogenetics (Wiegert et al., 2017; Rost et al., 2022). Opsins can be activated within millisecond time range and are more precise over the region of stimulation. The most commonly used opsins for suppressing neuronal activity are halorhodopsin (eNpHR3.0) (Zhang et al., 2007), a light-driven chloride pumping protein, and archaerhodopsin (eArch3.0) (Chow et al., 2010), a light-driven proton pump. However, it is important to note that both opsins may have off-target effects. Excessive activation of halorhodopsin can shift the cellular chloride reversal potential, leading to GABA-mediated excitation (Raimondo et al., 2012). Similarly, archaerhodopsin can increase intracellular pH, resulting in elevated spontaneous neurotransmitter release (Mahn et al., 2016). Both inhibitory opsins require continuous delivery of high blue light power to sustain their ion pumping activity. To monitor the activity of dorsal subicular neurons using two-photon imaging of a calcium sensor, a red-shifted inhibitory opsin such as Jaws (Chuong et al., 2014) should be used to avoid simultaneous activation of the opsin via the two-photon excitation. Recent developments in optogenetic silencing of neurotransmitter release (Mahn et al., 2021) have overcome the limitations of halorhodopsin and archaerhodopsin. However, there are currently no red-shifted variants available for simultaneous use with two-photon calcium imaging. While optogenetic silencing would have been more precise in timing and location, I chose chemogenetic synaptic silencing due to the potential interference between optical monitoring of neuronal activity and optical input manipulation.

4.2.2. Unspecific effects of the chemogenetic silencing experiments

The DREADD-mediated pathway reduction showed different effects of CA1 and EC inputs on the tuning of subicular VGluT2$^+$ neurons. During the 30-minute period between the Pre- and Post-CNO imaging sessions of subicular calcium activity, there was a decrease in the tuning of subicular VGluT2$^+$ neurons, even under the control

condition. It is important to consider the effects of time and/or CNO on the tuning of subicular neurons.

Regarding the time effect, each experiment lasted at least 50 minutes. The mouse was head-fixed under the microscope and could move voluntarily on the linear treadmill during this period. This approach was chosen to minimize changes in the field of view, from which the neuronal activity was imaged. However, there is still a possibility that the field of view slightly changed during the 30-minute waiting period for the perfusion of the CNO in the imaging window. Furthermore, it is possible that the calcium indicator underwent bleaching during the imaging process. Both changes in the field of view and bleaching of the calcium indicator could explain the observed decrease in the total sum of the $\Delta F/F$ values (Figure 17C), which could be due to a decrease in activity-based fluorescence change (ΔF) or an increase in background fluorescence (F). Since neuronal tunings were calculated based on correlations with the raw $\Delta F/F$ values, these changes can account for the decrease in the tuning parameters in the control condition.

The relatively long duration of the experiment may have affected the animals' performance on the linear treadmill. To ensure comparable performance, I food-restricted the mice and trained them to run an average of ten rounds in ten minutes per day. On average, all mice ran similar amounts of rounds on the linear treadmill with comparable mean velocities in both Pre- and Post-CNO imaging rounds (Supplementary Figure 5). Their licking behavior was also similar (see Supplementary Figure 5). However, there was high variability among the animals. It cannot be ruled out that individual animal performance, independent of the experimental group, had an influence on the tunings of dorsal subicular VGluT2$^+$ neurons, as the engagement of the animal can affect the spatial tunings of CA1 pyramidal neurons (Pettit et al., 2022). The food-restriction, in particular, could have influenced individual task engagement. In the Pre-CNO condition, the animals were hungry and received a milk reward every round. As mice became increasingly more sated as they obtained more rewards in the task, their engagement may have progressively decreased in the Post-CNO condition. However, their average licking behavior remained unchanged (Supplementary Figure 5).

Although being used as an agonist to activate the DREADD receptor, CNO *per se* can have an effect on brain circuits and behavior. CNO is metabolized into clozapine and

can bind to endogenous histamine H1, serotonin 5-HT2A, muscarinic M1, M3, M4, and dopaminergic D1 and D2 receptors in the brain (Gomez et al., 2017). It has been shown that CNO administration in the absence of any DREADD expression affects locomotion and acoustic startle reflex (MacLaren et al., 2016). These results were obtained from experiments in which CNO was administered systemically via intraperitoneal injections. To address these concerns, I administered the DREADD agonist CNO directly through a miniature hole into the SUB. However, it is not possible to exclude any effect of CNO in the control condition.

Taken together, there are several possible reasons for the decrease in the tuning of subicular VGluT2$^+$ neurons in the control condition. I was able to show that there was bleaching between the two imaging sessions In addition, I can rule out that behavioral engagement could be a reason for the observed decrease in the tuning of subicular VGluT2$^+$ neuron in the control condition. Furthermore, and the field of view may have changed slightly between imaging sessions and CNO might have influenced the tuning of subicular neurons in the control condition. However, it is crucial to mention that the effect of CNO was compared between DREADD-expressing and non-DREADD-expressing subicular VGluT2$^+$ neurons. Therefore, these changes in the control condition were taken into account.

4.2.3. CA1 and EC inputs are necessary for spatial tuning of dorsal subicular neurons

The DREADD-mediated pathway reduction demonstrated distinct impacts of CA1 and EC inputs on the spatial tuning of subicular neurons. The reduction in spatial tuning was significantly greater in the DREADD mediated pathway reduction compared to the control condition. The additional decrease was also validated through estimation statistics.

The reason these effects are not more pronounced could lie in the spatial limitations of the approach. CNO was administered through a miniature hole in the imaging window, resulting in a time-dependent concentration gradient of CNO in the SUB. It is likely that not all synapses from one input region expressed the DREADD receptor, and not all synapses with the DREADD receptor were activated by CNO. As a result, the

population of VGluT2$^+$ neurons experienced various effects based on which specific place input was eliminated. For example, removing a CA1 input that is tuned to the same place as the subicular neurons would lead to a decline in subicular place tuning. In contrast, eradicating a CA1 place input not represented in the subicular neuron's place field could enhance place tuning in the subicular neuron. Nonetheless, on average, I found that input reduction from both pathways led to decreased place tuning in subicular neurons. Consequently, I conclude that spatial tuning is transmitted from presynaptic neuronal populations in both the CA1 and EC areas to subicular VGluT2$^+$ neurons. These results align with the role of tri-synaptic and monosynaptic hippocampal pathways in the spatial tuning of CA1 pyramidal neurons. Reduction of CA3 input (Brun et al., 2002; Nakashiba et al., 2008; Davoudi and Foster, 2019) as well as EC input (Schlesiger et al., 2015) has been reported to result in a decrease of the Place Score in CA1 pyramidal neurons.

Spatial tuning properties of subicular VGluT2$^+$ neurons were quantified using two different approaches. Firstly, the Place Score was calculated. Originating from information theory (Skaggs et al., 1993), the Place Score quantifies the contrast between spatial bins with high and low neuronal activity, irrespective of whether the spatial bins with high or low activity are next to each other (Equation 6). Secondly, the spatial vector strength Rho was calculated. Rho essentially assesses the bulk of neuronal activity across the entire belt, taking into account the locations of the spatial bins on the treadmill belt (Danielson et al., 2016; Sharif et al., 2021).

Interestingly, I demonstrated that CA1 input influences both the Place Score and the spatial vector strength Rho, while EC input only contributes to the Place Score. These observations can be explained by the numerical summation of spatially tuned inputs (Target not found!). CA1 input is place tuned to specific locations on the linear track. Additionally, grid-like input from EC on a linear track is phasic, exhibiting different spacings. The numerical summation of both inputs produces a subicular place field with maximum activity at a distinct position (Target not found! B). When only integrating CA1 place input, the activity is concentrated in a particular location, but with decreased Place Score and Rho (Target not found! C left). Interestingly, exclusively summing the EC input numerically results in a place field with an increased Place Score and a

moderately decreased Rho (Target not found! C right). Assuming that the reduction of the DREADD-mediated pathway only partially inactivated the different input streams, I only summed some of the inputs. Similar to the DREADD-mediated pathway reduction of CA1 input, summing EC input with partial CA1 input (Target not found!D right) results in a place field with a lower Place Score and Rho. Additionally, when CA1 input is combined with only partial EC input (Target not found! D left) in a manner similar to the DREADD-mediated pathway reduction of EC input, a place field emerges with a decreased Place Score and a moderately decreased Rho, which is consistent with the results of the experiments.

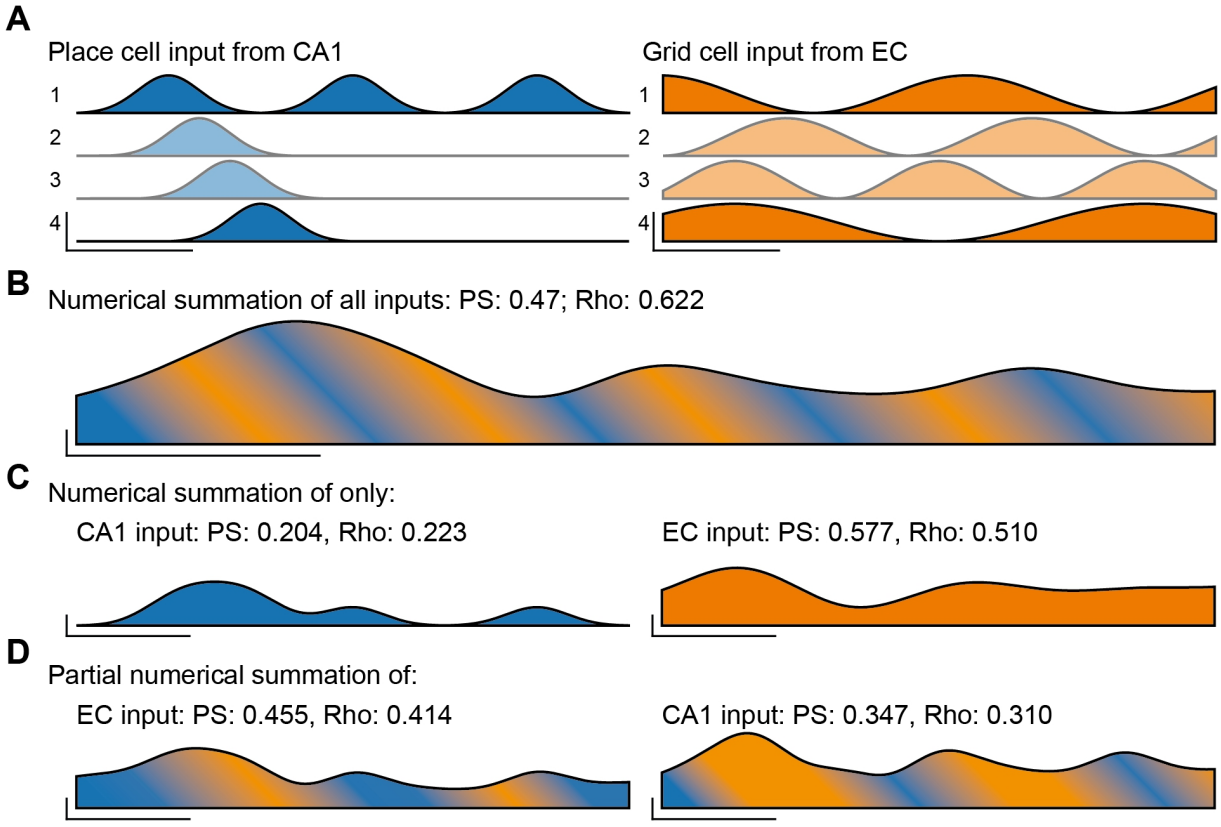

Figure 22: Numerical summation of CA1 and EC inputs to dorsal subicular neurons

A: Numerical summation of spatially tuned input from CA1 and EC in subicular neurons. Blue: Place cell input with one general place input (multiple CA1 neurons) along the linear track and from three CA1 neurons with place fields in specific locations of a linear track. Orange: Grid cell input from EC on a linear track as phasic activity with different spacings. B: Numerical summation of all inputs results in a pronounced place field with a high Place Score and a high Rho. C left: Numerical summation of only CA1 input (DREADD EC) shows a small place field with reduced Place Score and Rho. C right:

Numerical summation of only EC input (DREADD CA1) results in a place field with increased Place Score and reduced Rho. D left: Numerical summation of CA1 input and partial EC input (input 1 and 4; DREADD EC) shows a place field with decreased Place Score and moderate decrease in Rho. D right: Numerical summation of EC input and partial CA1 (inputs 1 and 4, DREADD CA1) input results and a Place field with decreased Place Score and Rho.

4.2.4. CA1 is necessary for the speed tuning of dorsal subicular neurons

In addition to providing spatially tuned inputs, CA1 and the EC convey information about the animal's locomotion speed (Kropff et al., 2015; Góis and Tort, 2018). Speed cells have first been observed in the EC and are modulated by the animal's locomotion speed (Sargolini et al., 2006; Kropff et al., 2015; Hinman et al., 2016). Moreover, neuronal activity of CA1 is correlated to an animal`s locomotion speed (McNaughton et al., 1983; Ekstrom et al., 2001; Góis and Tort, 2018; Iwase et al., 2020). Both input components could therefore contribute in similar or different ways to the velocity tuned output of subicular neurons. Subicular neurons either relay this speed input to other brain areas (Kitanishi et al., 2021; Ledergerber et al., 2021).

Notably, I discovered that only the reduction of the CA1 pathway through DREADDs leads to a decrease in velocity tuning among subicular VGluT2^{+} neurons. These findings suggest that while direct place-related input from both CA1 and EC is necessary for subicular spatial output tuning, only direct CA1 speed input is transformed into the animal's locomotion speed-associated output in subicular neurons. Thus, information regarding the locomotion speed of animals is conveyed to dorsal subicular pyramidal neurons predominantly through the trisynaptic loop (via DG-CA3-CA1), rather than via direct monosynaptic projections from the EC. Notably, two-photon calcium imaging of EC boutons in various subfields of the hippocampus revealed diverse spatial coding properties of EC inputs based, on their location within the hippocampal subfield (Cholvin et al., 2021). These results suggest that the EC provides various types of information to different subfields of the hippocampus, and that the SUB might not receive information about the animal's movement speed from the EC. It remains to be determined whether other hippocampal subfields receive speed-tuned input from EC, or if EC speed tuning is mainly necessary for the EC internal computation of path integration and other

mnemonic functions (Mcnaughton, 2006).

Another example of area-specific integration of speed tuned input comes from the medial septum / diagonal band of broca (MSDB). Glutamatergic neurons in this area are tuned to the animal's movement speed (Fuhrmann et al., 2015; Justus et al., 2017). Pyramidal neurons of CA3 receive direct glutamatergic input from the MSDB (Huh et al., 2010), whereas CA1 neuronal activity is modulated by MSDB activity via a disinhibitory interneuron-interneuron circuit (Fuhrmann et al., 2015). It has not yet been demonstrated that subicular neurons receive monosynaptic speed-tuned input from the MSDB.

4.3. Input–output transformation in dorsal SUB pyramidal neurons

To fulfill its role in neuronal circuits, a crucial function of any neuron is to receive inputs from its presynaptic partners and transform these inputs into its own action potential output. Understanding how neurons integrate their diverse synaptic inputs is thus a major focus of neuroscience. The work presented here illuminates the integrative properties of subicular pyramidal neurons.

The degree of functional compartmentalization of the dendritic tree, in conjunction with the synaptic location of specific information, is a major contributing factor to the synaptic integration of various inputs. Numerous studies have examined the dendritic integration of pyramidal neurons in the neighboring CA1 region (Spruston et al., 1995; Migliore et al., 2005; Losonczy and Magee, 2006; Spruston, 2008; Masurkar et al., 2020). In these neurons, EC synapses are located exclusively in the distal tuft region. These inputs are integrated first and depending on their depolarizing effect can lead to dendritic calcium spikes that are further integrated with proximal CA3 input. Thus, CA1 pyramidal neurons integrate these inputs more independently, based on their spatial separation in the dendritic tree. This supralinear integration strategy is sensitive to clustering (Tran-Van-Minh et al., 2015): If the localized EC input fails to elicit a dendritic calcium spike, their contribution to the somatic membrane potential and therefore the neuron's output is

minimal. To investigate the synaptic distribution in dorsal subicular pyramidal neurons, I performed subcellular CRACM. I revealed that the synapses of CA1 and EC target distinct regions of the dendritic tree of subicular VGluT2^{+} bursting pyramidal neurons. CA1 synapses are located on the proximal basal dendrites of subicular neurons, while EC synapses target more distal regions. The hot spots of synaptic input are separated by about 250 µm. In addition, EC synapses in the dendritic tree of subicular neurons are more widely dispersed. This results in greater overlap between CA1 and EC synapses, particularly in the proximal dendrites of subicular neurons (Figure 16). This synaptic distribution suggests that EC input is integrated locally together with CA1 input in the proximal dendrites of subicular neurons, resulting in a more linear integration strategy with a single, final integration point at the action potential initiation zone in these neurons (Figure 3). Further experiments focusing on dendritic non-linearities need to determine whether distal EC inputs are integrated separably in dorsal subicular neurons.

While supralinear integration is sensitive to clustering, the proposed linear integration strategy would be more sensitive to scatter. In linear integration, PSPs sum linearly, ultimately reaching the reversal potential of the ions involved (Magee, 2000). In addition, summed or single PSPSs are attenuated and filtered on their way towards the soma. Therefore, the maximum depolarization at the final integration point, the soma, is optimized by distributing synapses with identical tuning across various dendritic branches (Tran-Van-Minh et al., 2015). A linear integration strategy would support the stability of spatial tuning in subicular neurons when receiving rapidly changing input from CA1 place cells. Additionally, a linear integration approach could explain the operational mode of subicular pyramidal neurons:

Subicular place tuning seems to generalize over different geometric environments (Sharp, 1997) as well as during light-dark transitions (Brotons-Mas et al., 2010). In contrast, the upstream spatial representation in area CA1 is highly dynamic and remaps in different environments (Muller and Kubie, 1987; Leutgeb et al., 2005). A linear integration strategy would assist dorsal subicular neurons in maintaining stable spatial tuning despite receiving inputs with varying tunings. If all inputs sum linearly and contribute to the spatially tuned action potential output of subicular neurons, then

changes in a subset of CA1 inputs would be less impactful on the overall spatial tuning of subicular neurons. Conversely, in scenarios where clustered CA1 and EC spatial inputs are augmented by dendritic nonlinear events, even slight alterations in just a few CA1 synapses could significantly affect the spatial tuning of subicular neurons.

Importantly, the differences in remapping between CA1 and SUB may explain the operation mode of subicular pyramidal neurons. Spatial tuning can be attributed to the coincidence detection between place preferences of both input streams. If input from CA1 alone were sufficient to trigger action potential firing in dorsal subicular pyramidal neurons, then alterations in CA1 input would directly lead to changes in the spatial tuning of these neurons. Conversely, spatially tuned input from the EC, in conjunction with spatially tuned input from CA1, might be necessary to elicit spatially tuned output in dorsal subicular neurons. In this framework, the EC provides spatial information in form of a grid that spans the entirety of a given environment and provides a global, more static signal of the animal's current location (Fyhn et al., 2007). Thus, the spatially tuned output of dorsal subicular neurons is achieved through coincident detection of stable grid input from the EC and specific place-tuned input from CA1 (Target not found!) (Jacobs and Schenk, 2003).

This coincidence detection, combined with a global integration strategy, enhances the stability of the spatial tuning in the output of subicular neurons. The linear summation of all inputs determines the final output of the subicular neuron, and with constant EC input, changes in CA1 input groups become less influential on the overall spatial tuning of subicular neurons. This operational mode is corroborated by our DREADD-mediated pathway-dependent reduction experiments, which demonstrated that inputs from both CA1 and EC affect the spatial tuning of dorsal subicular pyramidal neurons.

Importantly, a linear integration strategy does not rule out the presence of voltage-dependent modulation of synaptic input arriving at dorsal subicular pyramidal neurons. Indeed, glutamatergic CA1 and EC synapses on subicular pyramidal neurons have NMDA receptors (Wozny et al., 2008; Behr et al., 2009; Fidzinski et al., 2011). Thus, co-active or repetitive synaptic activity can lead to NMDA-dependent nonlinear events (NMDA spikes) with local amplification of this synaptic input. These NMDA spikes are highly localized and attenuate on their way towards the soma (Larkum and Nevian,

2008; Major et al., 2008). Multiple NMDA spikes can sum linearly at the soma and initiate action potential firing (Poleg-Polsky, 2015).

NMDA spikes represent just one form of local dendritic regenerative spiking events. Particularly, those dendritic spikes involving calcium play a crucial role in synaptic plasticity (Behr et al., 2009; Bittner et al., 2017). Although the distribution of CA1 and EC synapses suggests a linear integration strategy, further research focusing on dendritic spiking events and synaptic plasticity is necessary. Such studies are essential to conclusively determine the integration strategy employed by dorsal subicular neurons.

4.4. Excitatory and inhibitory neurons in the SUB

As many other areas of the brain, the SUB contains both excitatory pyramidal neurons and inhibitory interneurons. Researchers have classified neurons into various cell types based on their electrophysiological and histochemical properties (Sosulina et al., 2010; Ferrante et al., 2016; Justus et al., 2017). Furthermore, neurons are differentiated based on their projection targets (Hattox and Nelson, 2007; Unal et al., 2015), specifically in the SUB region (Kim and Spruston, 2012; Cembrowski et al., 2018a). Additionally, single-cell mRNA sequencing has provided a recent method for classifying cell types based on their RNA expression patterns (Zeisel et al., 2015; Harris et al., 2017; Tasic et al., 2018). While various interneuron cell types have been identified over many years, recent evidence strongly suggests that excitatory neurons can also be further categorized into different subtypes (Zeng and Sanes, 2017; Cembrowski and Spruston, 2019; Shepherd et al., 2019; Kim et al., 2020; Yuste et al., 2020).

4.4.1. Internal structure of excitatory pyramidal neurons in the SUB

Emerging evidence delineates a division of the SUB along a proximo-distal axis, with the proximal end adjacent to CA1 (Cembrowski et al., 2018b). Furthermore, this division seems to generalize over the whole tri-synaptic loop of the hippocampus. The primary inputs to the hippocampus from the lateral and medial EC project to the proximal and distal CA1 regions, respectively. In turn, the proximal CA1 primarily projects to the distal SUB, while the distal CA1 predominantly targets the proximal SUB. Therefore, specific subregions of the SUB receive information from distinct subregions of the hippocampal

formation, suggesting parallel streams of information within the hippocampal formation (Witter, 2006). The findings of this study corroborate the functional topographical organization of the SUB.

I identified two clusters of subicular pyramidal neurons: regular spiking and bursting neurons (Taube, 1993; Prida, 2003; Graves et al., 2012). Notably, these two clusters differ not only by the number of action potentials fired at rheobase stimulation but also by various subthreshold and suprathreshold parameters (Figure 13). Sag indices were higher in bursting subicular neurons, indicating different forms of hyperpolarization-activated cation currents (h-currents) in these neurons (Van Welie et al., 2006; Fei et al., 2022). In addition, action potential peaks were higher, and action potential thresholds were lower for bursting subicular neurons, which suggests that differences in inward currents (mainly sodium and calcium currents) may underlie the observed differences in action potential firing (Mattia et al., 1997; Jung et al., 2001). Finally, an increase mean firing frequency at stimulation with three times rheobase stimulation indicates a faster action potential repolarisation in bursting subicular neurons, probably based on a difference in high threshold or calcium-activated potassium channels (Golding et al., 1999). Taken together, these results suggest that these two electrophysiological clusters differ in their main ion channel composition indicating that these neuronal populations are stable cell types with distinct identities.

VGluT2 has been previously established as a molecular marker for the distal part of the dorsal SUB (Ishihara and Fukuda, 2016). The distribution of VGluT2 in the two electrophysiological clusters is in line with previous reports (Wozny et al., 2018). Notably, in their and my data, around 80 % of VGluT2 positive subicular neurons show bursting in my experiments. Thus, VGluT2 does not capture all, but the vast majority of bursting neurons in the distal dorsal SUB. Another marker for the distal dorsal subiulum is NTS that correlates with VGluT2 expression and shows the same distribution among bursting neurons (Cembrowski et al., 2018a). Remarkably, NTS positive neurons target distinct brain regions mainly involved in spatial navigation and memory. Thus, these brain regions receive more input from bursting neurons (Kim and Spruston, 2012), indicating a functional and anatomical distinction between regular spiking proximal and bursting distal subicular neurons.

The idea of parallel streams of information within the hippocampal formation (Ciocchi et al., 2015; Kitanishi et al., 2021) is further strengthened by the finding that only the distal dorsal SUB is involved in a spatial memory task (Cembrowski et al., 2018a). Thus, while the functional role of the proximal dorsal SUB remains elusive, the distal dorsal SUB seems to be involved in spatial navigation. Notably, I found spatially and velocity-tuned input only in bursting subicular neurons indicating their participation in spatial navigation. Further studies will be needed to investigate the role of the proximal SUB.

4.4.2. Inhibitory circuits in the SUB

This study focused on the canonical input to dorsal subicular neurons, which is excitatory (glutamatergic). It is important to recognize that the SUB also contains interneurons that are well known for their role in inhibitory functions within the SUB, especially in relation to epileptic seizures (Knopp et al., 2005). However, although different immunohistochemical types of interneurons have been described for the CA1 region (Hernández-Frausto et al., 2023), interneurons in the SUB are poorly characterized. In the SUB, fast-spiking parvalbumin-positive basket cells have been observed in the pyramidal layer (Greene and Totterdell, 1997; Prida, 2003; Böhm et al., 2015), and chandelier cells are present in the molecular layer (Soriano et al., 1993). Additionally, calbindin-positive interneurons are found in both the pyramidal cell and molecular layers of the SUB (Knopp et al., 2008). Moreover, interneurons expressing somatostatin (SOM) and the nicotinic acetylcholine receptor alpha2 subunit (Chrna2) are located in the polymorphic layer, with axons extending into the molecular layer. These neurons are similar to oriens-lacunosum moleculare (OLM) interneurons found in CA1 (Nichol et al., 2018).

Even less is known about the connectivity between and among interneurons and pyramidal neurons in the SUB. Regarding local excitatory connections onto fast-spiking presumably PV+ basket cells, regular spiking subicular neurons have a higher connection probability than bursting subicular neurons (Böhm et al., 2015), indicating that regular spiking neurons are more strongly involved in recruiting local inhibition. In addition, PV^+ basket cells form synaptic connections around the soma (Prida, 2003) and therefore limit action potential firing. They are involved in a feedback inhibition circuit motive where the same neuron that gives input to an interneuron is inhibited by the

same interneuron. When the inhibitory neuron receives excitatory input from neighboring pyramidal neurons, this feedback inhibition is known as lateral inhibition. Both circuit motives can be responsible for synchronizing pyramidal cell populations during network oscillations (Miles et al., 1996) or might sharpen the tuning properties of neurons (Hangya et al., 2010; Isaacson and Scanziani, 2011; Jeong and Singer, 2022). OLM interneurons form synapses in the dendritic tree of CA1 pyramidal neurons (Müller et al., 2012). These neurons directly influence the dendritc integration of excitatory synaptic inputs by shunting inhibition (London and Häusser, 2005) and strongly reduce local excitation in dendrites (Müller et al., 2012). In addition, OLM interneurons target other interneurons in the CA1 region (Leão et al., 2012; Fuhrmann et al., 2015), thus participating in another circuit motif, namely disinhibition, where the activity of one interneuron is reduced by the inhibition of another interneuron. Finally, all interneurons can be activated by excitatory input from outside the SUB, making them a part of feed-forward inhibition. In this circuit motif, a presynaptic partner of a pyramidal neuron also connects to an inhibitory interneuron, which then projects to the same pyramidal neuron. This leads to initial excitation of the postsynaptic pyramidal neuron, followed by delayed inhibition from the interneuron, effectively sharpening the post-synaptic response.

In the presented experiments, the influence of inhibition was kept minimal. Voltage clamp recordings were performed at a holding potential of - 70 mV. Thus, near their reversal potential, these ions could not add an outward current to the somatic current recording, although shunting inhibition was not perturbed. For slice experiments, GABAergic transmission was blocked by the bath-application of the appropriate antagonists. In the DREADD-mediated pathway reduction experiments, two possible circuit motifs could be affected. First, feed-forward inhibition could be decreased by reduction of either CA1 or EC excitatory input to subicular inhibitory interneurons. Second, a DREADD-mediated reduction of inhibitory input from CA1 or EC input to subicular interneurons could lead to decreased disynaptic inhibition. Notably, inhibitory connections from CA1 project mainly to local inhibitory neurons in the SUB (Jinno et al., 2007; Fuentealba et al., 2008; Francavilla et al., 2018). The same is true for inhibitory projections from EC to CA1(Melzer et al., 2012; Basu et al., 2016), but evidence for an EC inhibitory projection to SUB is missing. Therefore, while my research provides substantial evidence for a canonical excitatory information flow to subicular neurons, the

potential involvement of interneurons in the input-output transformation of these neurons cannot be disregarded. A reduction in either monosynaptic or disynaptic inhibition could have diverse effects on the integration of spatially tuned input into the spatially tuned output of subicular neurons. This aspect warrants further investigation in future studies.

4.5. Further tunings within the animal's spatial navigation

The SUB must integrate far more information beyond the previously described spatially- and speed-tuned input. Indeed, the output of subicular neurons combines multiple spatial variables (Ledergerber et al., 2021). In my experiments, the animals ran on a linear track, which allowed me to examine the integration of just two spatial variables: place and the animal's locomotion speed. I demonstrated that these spatial variables are integrated differently by dorsal subicular pyramidal neurons.

Moreover, the SUB receives a variety of spatially tuned inputs from other brain regions. A notable example is the neuronal representation of the animal's head direction. Subicular pyramidal neurons likely receive head-direction input from the EC (Giocomo et al., 2014), from the anterior thalamic nuclei (Taube, 1995; Frost et al., 2021), and from the nucleus reuniens of the thalamus (Jankowski et al., 2014). Conversely, subicular output is tuned to the animal's head direction (Olson et al., 2017; Kitanishi et al., 2021), and the input it receives regarding head direction is suggested to be essential for path integration and egocentric spatial navigation (Valerio and Taube, 2012), as performed by boundary vector cells (Lever et al., 2009) or subicular pyramidal neurons whose activity correlates with the animal's axis of travel (Olson et al., 2017). However, since my DREADD-mediated pathway reduction experiments were conducted while the mice were head-fixed, the influence of CA1 and EC inputs on the head-direction tuning of subicular neurons could not be determined. Future experiments with freely moving animals are needed to explore the input-output transformation of head-direction information.

Neurons in the hippocampal formation encode a wealth of information about the animal's environment. For instance, there are neurons tuned to odors (Taxidis et al., 2020), time (Eichenbaum, 2014), reward (Gauthier and Tank, 2018), objects (Burke et al., 2011; Vandrey et al., 2021), and novelty (Cohen et al., 2017). As a multi-integrative

structure with high baseline activity (Kitanishi et al., 2021) and heterogeneous information representation (Kim et al., 2012), subicular neurons are likely to integrate this information into a comprehensive code that is disseminated throughout the brain.

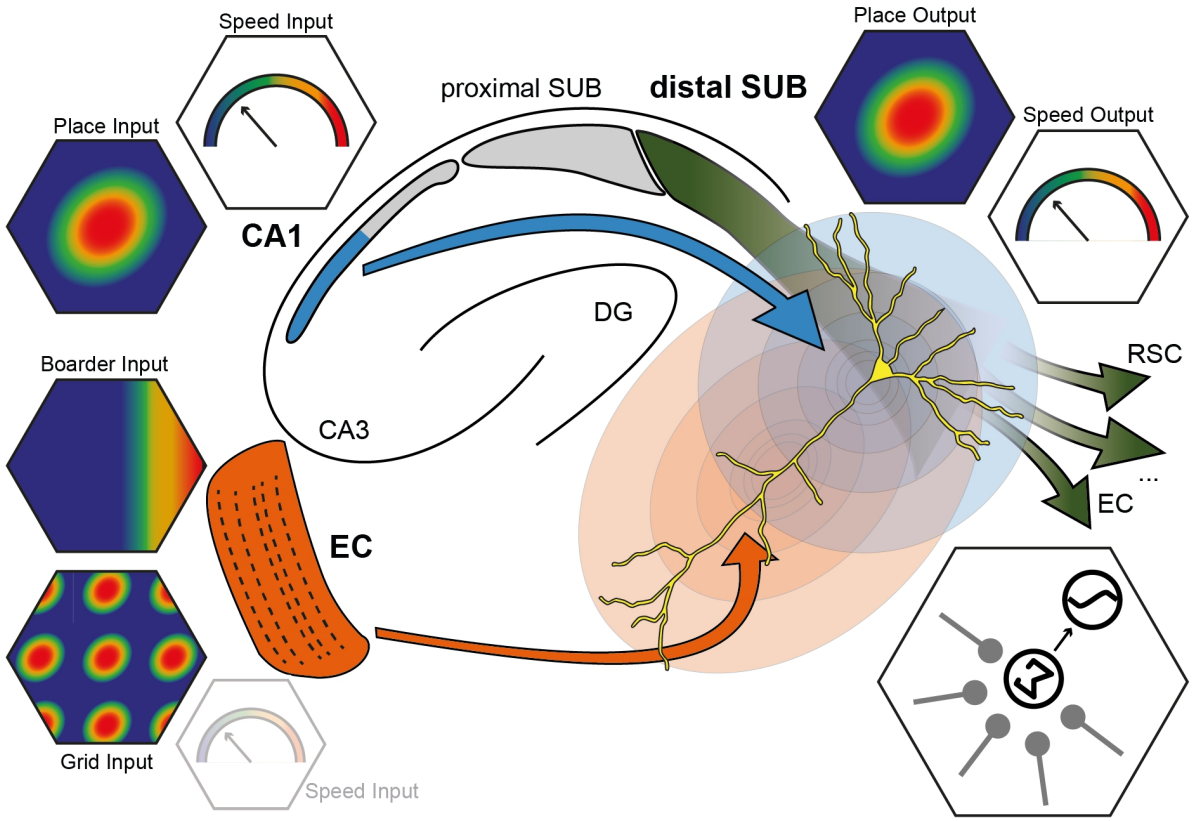

Figure 23: Functional integration of spatial and speed tuned input in dorsal subicular neurons

This schematic depicts the hippocampal formation, illustrating the two main hippocampal input streams to the dorsal SUB, which is subdivided into a proximal and a distal part. All three regions exhibit output tuning to different aspects of animal spatial navigation. In CA1, place and speed tuning are described, while in EC, activity can be tuned to the animal's position in a grid-like pattern, borders in the animal's environment, as well as the animal's locomotion speed. The distal dorsal region of the SUB receives input that is tuned to both place and speed, and neurons in this region show action potential output tuned to these aspects during an animal's spatial navigation. Thus, conceptionally, both input paths might convey their tuning to neurons in dorsal subicular neurons. My research indicates that although CA1 and EC inputs play a crucial role for place tuning, only direct CA1 speed input is responsible for the subicular neuron's output related to the animal's locomotion speed. In addition, there are two major input paths that target specific regions of the dendritic tree of dorsal subicular neurons. The synapse distribution in the dendritic tree reveals significant overlap in both input pathways, suggesting that CA1 and EC synapses converge on the same proximal dendrites in

dorsal subicular neurons. This synapse distribution implies a linear integration strategy that satisfactorily integrates spatial information in a compressed code that is distributed in parallel output pathways throughout the brain (eg. EC, RSC, green arrows).

5. Conclusion

The SUB constitutes the final segment in the sequential connectivity of hippocampal subregions, serving as a pivotal hub for hippocampal information processing. The role of the SUB in hippocampal information processing has been proposed to range from acting as a hub that disseminates neuronal representations to various brain regions (McNaughton, 2006) to functioning as a distinct computational unit in spatial navigation (Matsumoto et al., 2019). The SUB can be segmented along its ventral-dorsal axis as well as its proximo-distal axis, with these subdivisions participating in distinct brain functions. It establishes parallel output pathways that selectively relay hippocampally-processed information to various brain regions. This study concentrated on the input-output transformation of the distal dorsal part, which is primarily involved in the animal's spatial navigation. Notably, I observed spatially tuned input exclusively in distal-dorsal bursting subicular neurons. The two principal hippocampal input streams are the adjacent CA1 region and the EC. Excitatory inputs from CA1 target the proximal dendritic tree of dorsal subicular bursting neurons, while those from EC target the more distal dendrites. However, a significant overlap of these inputs in the proximal regions suggests a more linear dendritic integration strategy in these neurons. Functionally, I demonstrated that while CA1 and EC input are essential for the spatial tuning of dorsal subicular neurons, only CA1 contributes to their speed tuning in relation to the animal's locomotion speed. Therefore, although this study investigated the functional integration of the two major inputs to the SUB, it should be viewed as an initial step for further research. As previously suggested (Matsumoto et al., 2019), a comprehensive understanding of the SUB's functional role in hippocampal information processing requires an appreciation of all the diverse types of information integrated within subicular neurons. However, this study highlights the importance of what individual neurons are listening to, rather than what other brain regions may be communicating to them.

6. Appendix

6.1. Supplementary Figures

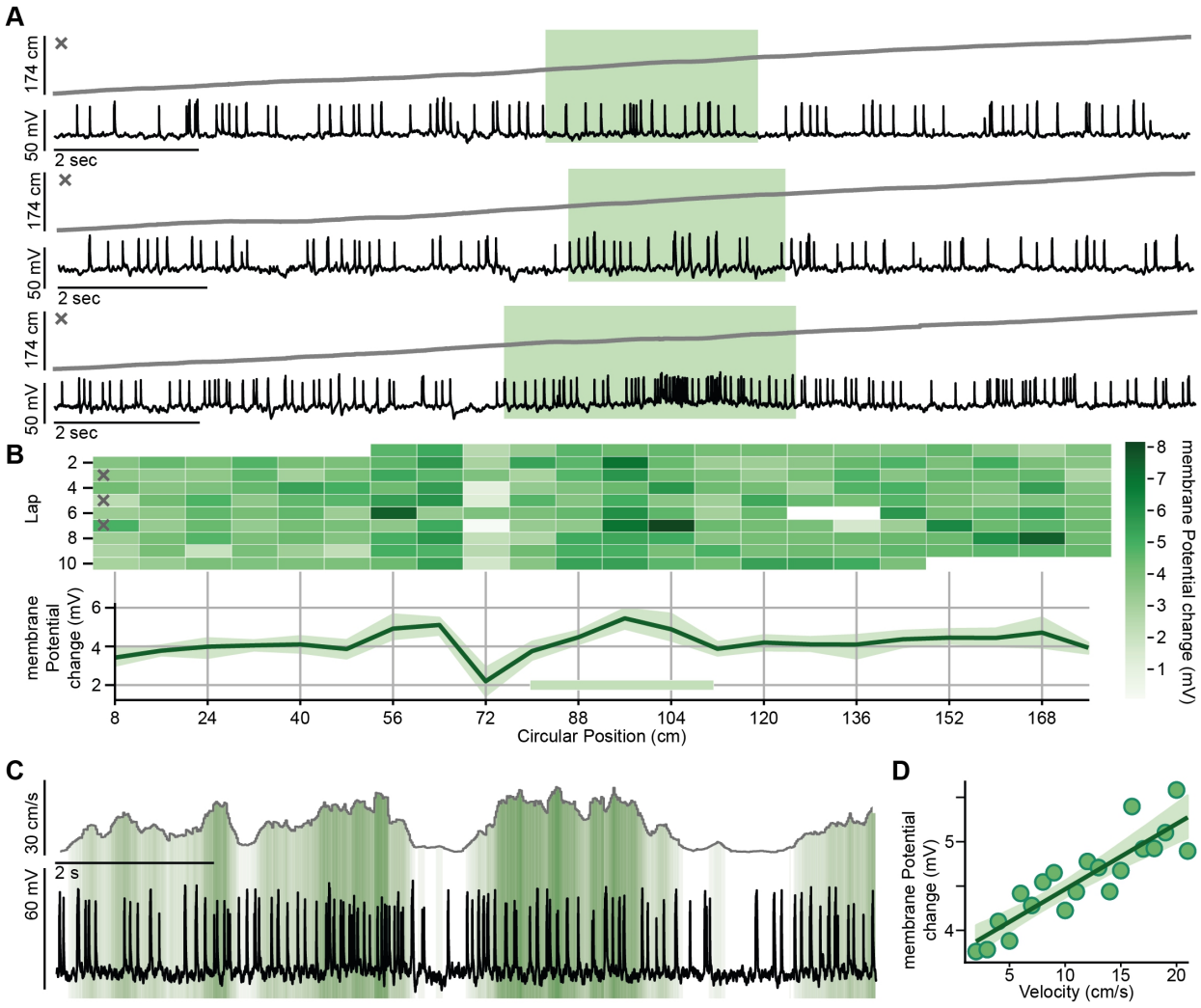

Supplementary Figure 1: Membrane potential of dorsal subicular pyramidal neurons is tuned to place and velocity

A-B: Spatial tuning of subicular output from one sample neuron. A: Whole cell membrane potential correlated to the animal's position on the circular track for three individual laps. Fields with strongest excitatory input are indicated in green. B: Color-coded mean membrane potential change for each spatial bin of the circular track for 10 rounds (top). Mean membrane potential change across laps for each bin showing place preference of subicular output from 82 to 112 cm (bottom). C-D: Velocity tuning of subicular output. C: Exemplary whole cell membrane potential recording correlated to the

animal’s velocity. Green bars indicate velocity bins with same velocity. D: Median membrane potential as function of the velocity bin. Linear regression indicates velocity tuning of this subicular neurons output ($p = 0.0001$).

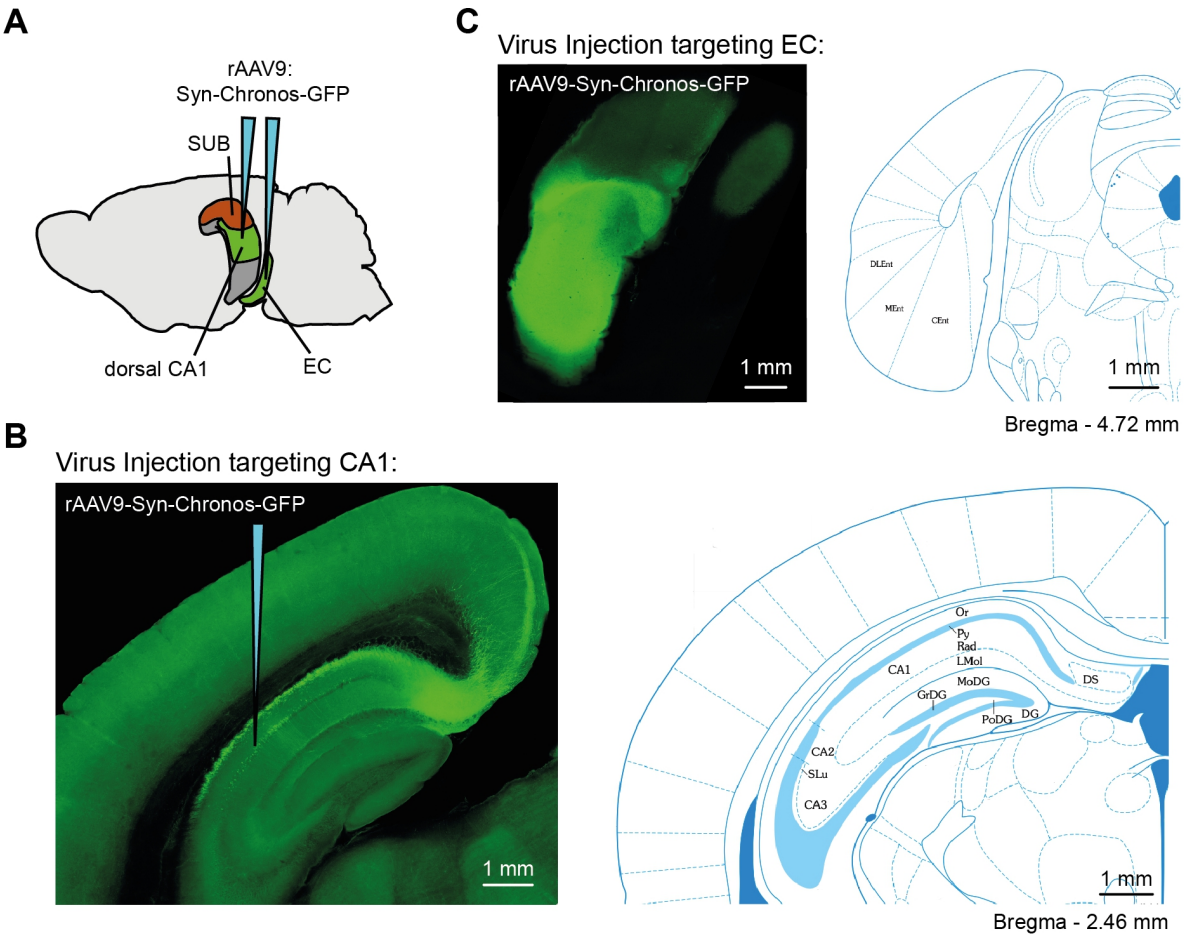

Supplementary Figure 2: Viral injection strategy for sub-cellular input mapping in dorsal SUB VGluT2^{+} bursting neurons

A: I injected the excitatory opsin Chronos with a GFP fluorescence tag in either CA1 (B) or EC (C) using stereotactic coordinates from Paxinos & Franklin 2006. B: Exemplary confocal image of the expression of Chronos-GFP by neurons in Stratum pyramidal of the CA1 region. Note the dense projection to the SUB. C: Exemplary confocal image of the expression of Chronos-GFP in the EC. Injections sites were compared to the mouse brain atlas (right schematics; adapted from Paxinos & Franklin 2006).

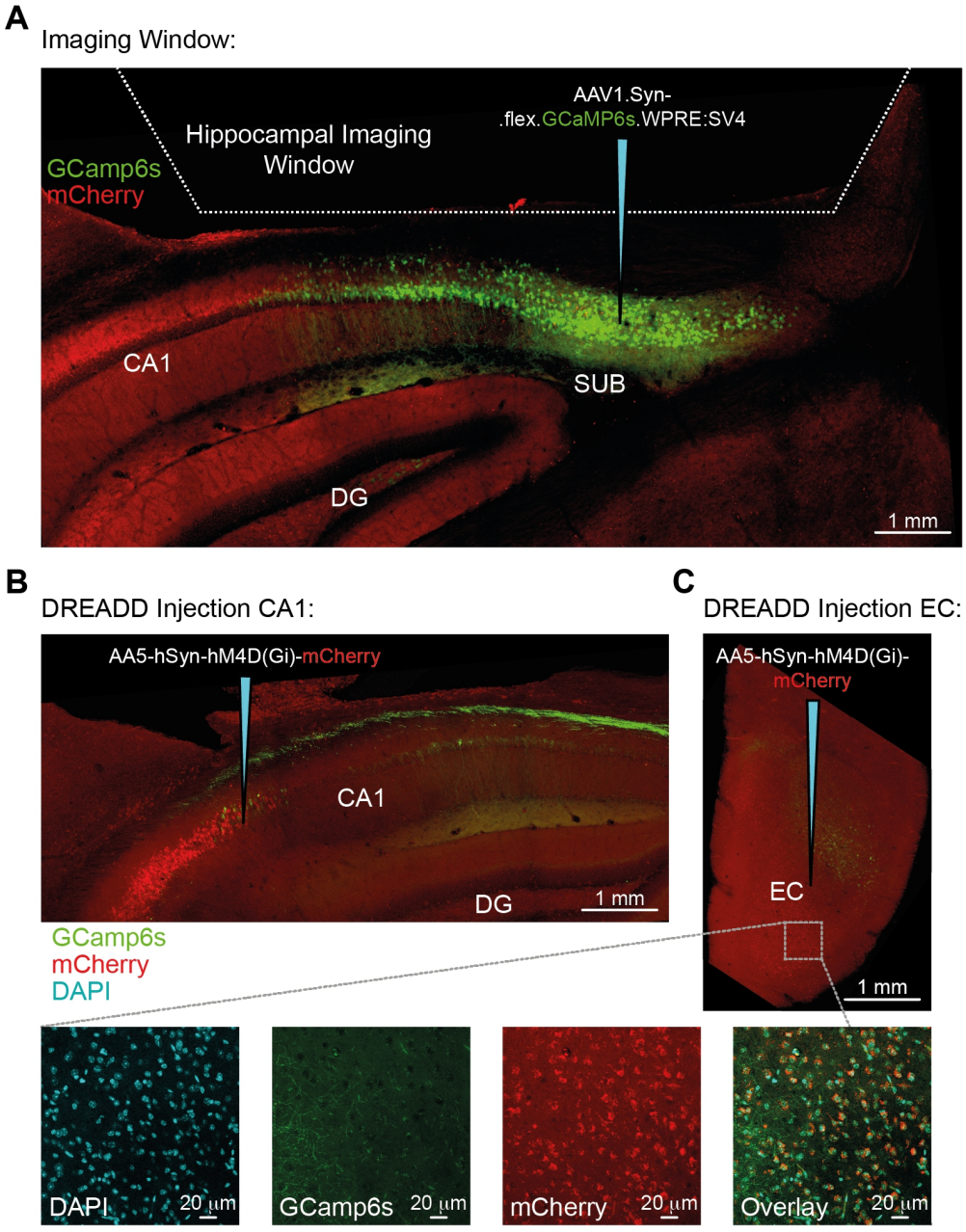

Supplementary Figure 3: Viral injection strategy for two photon calcium imaging with DREADD mediated pathway reduction

A: Coronal slice of dorsal hippocampus, injected with floxed GCamp6s in the dorsal SUB of VGluT2-Cre mice. To access the dorsal hippocampus for 2 photon imaging, the cortex above was remove and a hippocampal window was placed inside the skull of the animal. B: Viral transduction of the inhibitory DREADD in proximal CA1. C: Viral transduction of the inhibitory DREADD in the EC. Inlet shows a magnification of the area The overlay shows, that the inhibitory DREADD co-localizes with DAPI indicating a sucessfull transfection of EC neurons with the inhibitory DREADD.

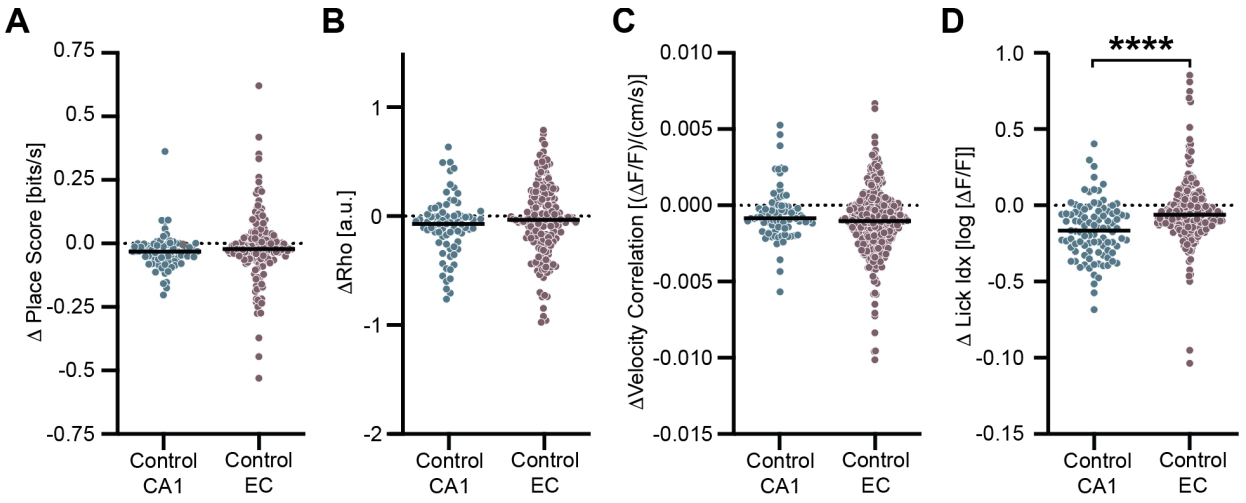

Supplementary Figure 4: Comparable changes of tuning parameters of VGluT2⁺ subicular neurons of between mice injected with the control virus in either CA1 or EC

Four animals each were injected with the AAV5-hSyn-mCherry control virus in either CA1 or EC. Spatial tuning was observed in 75 and 173 VGluT2⁺ subicular neurons from animals injected into CA1 (Control CA1) or EC (Control EC), respectively. A: Changes in Place Score between Pre- and Post-Imaging for the VGluT2⁺ subicular neurons for Control CA1 and Control EC showed no differences (Mann-Whitney U-Tests: p = 0.0979). B: Changes in Rho between Pre- and Post-Imaging for the VGluT2⁺ subicular neurons for Contral CA1 and Control EC did not differ (Mann-Whitney U-Tests: p = 0.1754). C: Velocity tuning was found in 72 and 318 VGluT2⁺ subicular neurons from Control CA1 and Control EC, respectively. There was no difference between both controls in the change of Velocity correlation between Pre- and Post-Imaging (Mann-Whitney U-Tests: p = 0.3360). D: Lick tuning was found in 97 and 219 VGluT2⁺ subicular neurons from Control CA1 and Control EC, respectively.The change of Lick Idx between Pre- and Post-Imaging differed between both control groups (Mann-Whitney U-Tests: p <0.0001).

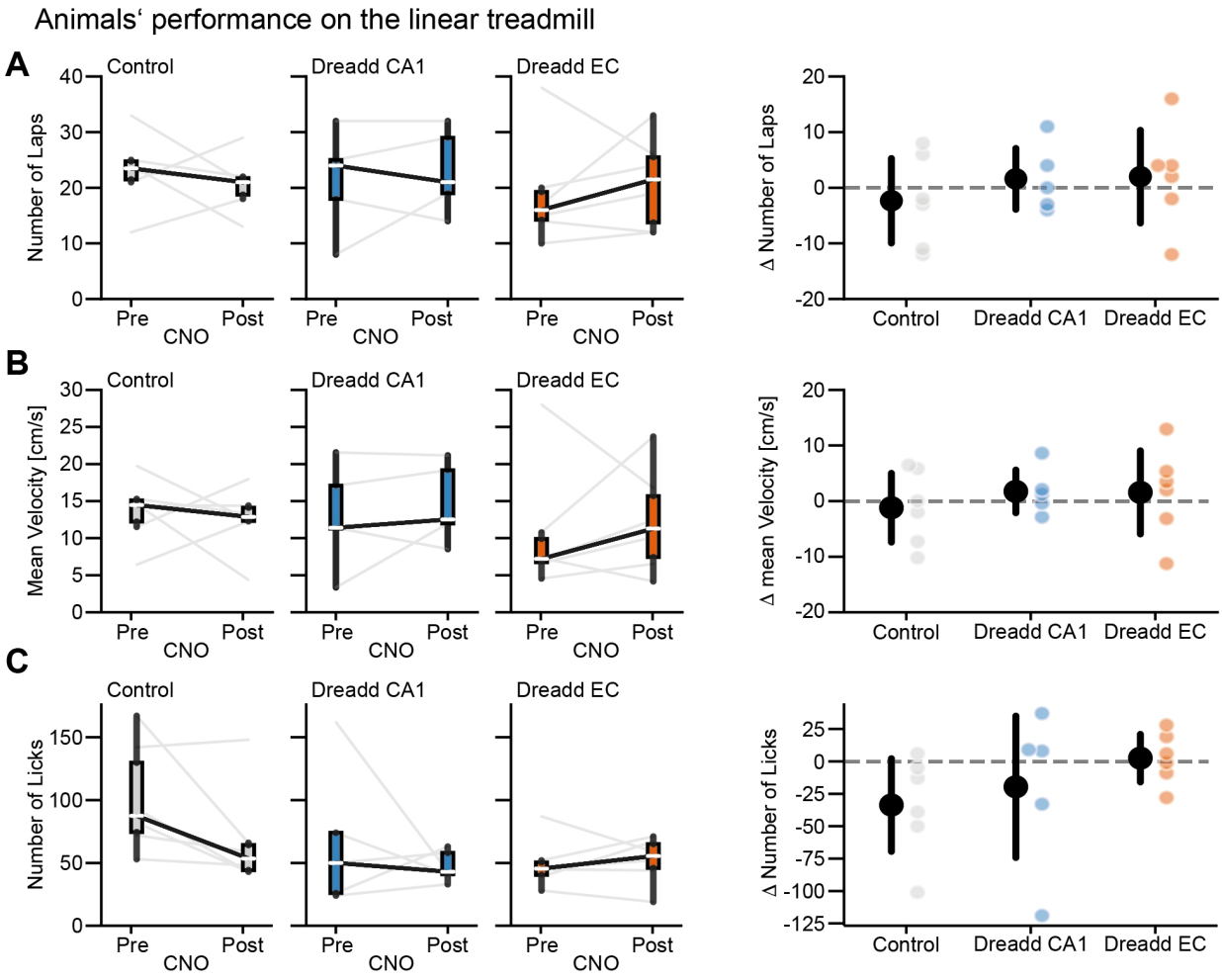

Supplementary Figure 5: Comparable performance of mice running on the linear treadmill

A: Number of Laps during Pre- and Post-Imaging for the control animals (grey; $n_{Control} = 6$) and the animals injected with the inhibitory DREADD either in CA1 (blue; $n_{DREADD\ CA1} = 5$) or EC (blue; $n_{DREADD\ EC} = 6$). Animals ran a similar distance during the experiment (RM two-way ANOVA: Pre/Post CNO x Experiment interaction, $F(2, 14) = 0.5178$, $p = 0.6068$) which is confirmed by the change in the Number of laps between Pre- and Post-CNO (right; one-way ANOVA $F(2, 14) = 0.5178$, $p = 0.6068$). B: Mean velocity between Pre- and Post-CNO for the three experimental groups (RM two-way ANOVA: Pre/Post CNO x Experiment interaction, $F(2, 14) = 0.3440$, $p = 0.7147$). The change in mean velocity was not different (right; one-way ANOVA $F(2, 14) = 0.3440$, $p = 0.7147$). C: Number of Licks between Pre- and Post-CNO for the three experimental groups (RM two-way ANOVA: Pre/Post CNO x Experiment interaction, $F(2, 14) = 1.137$, $p = 0.3486$). The change in number of licks was not different (right; one-way ANOVA $F(2, 14) = 1.137$), $p = 0.3486$).

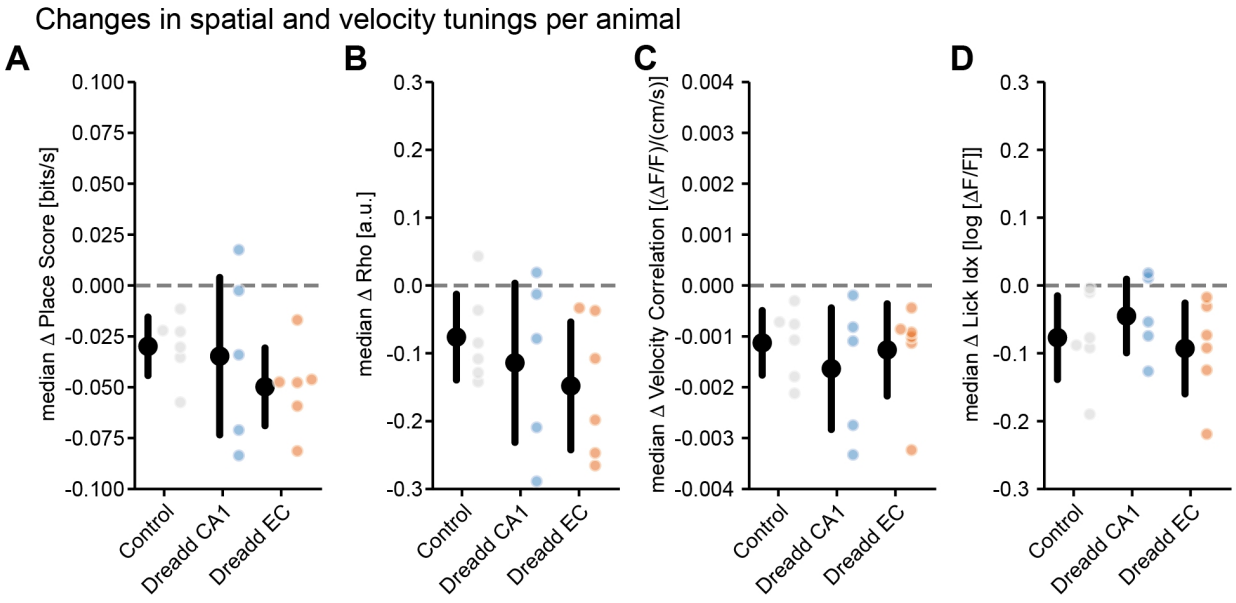

Supplementary Figure 6: Changes in tunings per animal

There were no differences in the median changes between the pre- and post-CNO conditions of the tuning parameters per animal. A: The median changes in Place Score per animal were comparable between the control and chemogenetic inactivation of either CA1 or EC (one-way ANOVA $F(2, 14) = 0.8240$, $p = 0.4589$). B: Changes in Rho per animal were not different between the experimental and the control group (one-way ANOVA $F(2, 14) = 0.7455$, $p = 0.4924$). C: The median changes in velocity tuning were similar among all groups (Kruskal-Wallis test: $H(3,14) = 0.4379$, $p = 0.8185$). D: The median changes in Lick Idx did not differ between the three groups (one-way ANOVA $F(2, 14) = 0.6932$, $p = 0.5163$).

6.2. Abbreviations

4-AP	4-amynopyridin
ΔF/F	Change of fluorescence over baseline fluorescence
µg	Microgramm
µl	Microliter
µm	Micrometer
µM	Micromolar
τ	Tau, membrane time constant
AAV	Adeno-associated virus
ACSF	Artificial cerebrospinal fluid
AMPA	α-amino-3-hydroxy-5-methyl-4-isoxazolepropionic acid
AP	Action potential
Ca^{2+}	Calcium^{2+}-Ion
CA	Cornus ammonis
CA1	Cornu ammonis region 1
CA3	Cornu ammonis region 3
CGP-52432	3-[[(3,4-Dichlorophenyl)methyl]amino]propyl]diethoxymethyl)phosphinic acid
CNO	Clozapine *N*-oxide
COM	Center of Mass
CRACM	Channelrodopsin assisted circuit mapping
DAP-5	D-2-amino-5-phosphonopentanoate
DNA	Deoxyribonucleic acid
DG	Denate gyrus

DREADD	Designer Receptors Exclusively Activated by Designer Drugs
EC	Entorhinal cortex
EPSP	excitatory post synaptic potential
GABA	γ-aminobutyric-acid
GCaMP6s	Genetically encoded calcium indicator isoform 6s
GFP	Green fluorescent protein
IR	Input resistance
Klk8	Kallikrein Related Peptidase 8
LTD	Long-term depression
LTP	Long-term potentiation
mg	Milligramm
mM	Millimolar
ms	Millisecond
MSDB	Medial septum / diagonal band of Broca
mV	Millivolt
NBQX	2,3-dioxo-6-nitro-7-sulfamoyl-benzo[f]quinoxaline
nm	Nanometer
NMDA	*N*-methyl-D-aspartate receptor
Nts	Neurotensin
pA	Picoampere
PSP	Postsynaptic potential
SUB	Subiculum
SR-95531	Gabazine, $GABA_A$ receptor antagonist
TTX	Tetrodotoxin
VGluT2$^+$	Vesicular glutamate transporter isoform 2-positive

6.3. Contributions

I am very thankfull for the help I received for this thesis: *In vivo* electrophysiological recordings were performed by Dr. Hiroshi Kaneko. I did the analysis of these recordings as well as the correlation of the recordings to the animals position and movement velocity. In addition, Dr. Oliver Barnstedt helped with the analysis of the calcium imaging data. He did the cell segmentation, registration and the cell pairing over both imaging sessions, while I did the manual inspection of the resulting $\Delta F/F$ traces as well as the cell pairing and the correlation of the $\Delta F/F$ traces with the animals behavior on the linear treadmill.

7. Bibliography

Adoff, M.D., Climer, J.R., Davoudi, H., Marvin, J.S., Looger, L.L., Dombeck, D.A., 2021. The functional organization of excitatory synaptic input to place cells. Nat. Commun. 12, 3558. https://doi.org/10.1038/s41467-021-23829-y

Alexander, A.S., Tung, J.C., Chapman, G.W., Conner, A.M., Shelley, L.E., Hasselmo, M.E., Nitz, D.A., 2022. Adaptive integration of self-motion and goals in posterior parietal cortex. Cell Rep. 38, 110504. https://doi.org/10.1016/j.celrep.2022.110504

Amaral, D.G., Dolorfo, C., Alvarez-Royo, P., 1991. Organization of CA1 projections to the subiculum: A PHA-L analysis in the rat. Hippocampus 1, 415–435. https://doi.org/10.1002/hipo.450010410

Amaral, D.G., Witter, M.P., 1989. The three-dimensional organization of the hippocampal formation: A review of anatomical data. Neuroscience 31, 571–591. https://doi.org/10.1016/0306-4522(89)90424-7

Anderson, M.I., O'Mara, S.M., 2003. Analysis of Recordings of Single-Unit Firing and Population Activity in the Dorsal Subiculum of Unrestrained, Freely Moving Rats. J. Neurophysiol. 90, 655–665. https://doi.org/10.1152/jn.00723.2002

Arenz, A., Silver, R.A., Schaefer, A.T., Margrie, T.W., 2008. The Contribution of Single Synapses to Sensory Representation in Vivo. Science 321, 977–980. https://doi.org/10.1126/science.1158391

Barnes, C.A., McNaughton, B.L., Mizumori, S.J., Leonard, B.W., Lin, L.H., 1990. Comparison of spatial and temporal characteristics of neuronal activity in sequential stages of hippocampal processing. Prog. Brain Res. 83, 287–300. https://doi.org/10.1016/s0079-6123(08)61257-1

Bar-Yehuda, D., Korngreen, A., 2008. Space-Clamp Problems When Voltage Clamping Neurons Expressing Voltage-Gated Conductances. J. Neurophysiol. 99, 1127–1136. https://doi.org/10.1152/jn.01232.2007

Basu, J., Zaremba, J.D., Cheung, S.K., Hitti, F.L., Zemelman, B.V., Losonczy, A.,

Siegelbaum, S.A., 2016. Gating of hippocampal activity, plasticity, and memory by entorhinal cortex long-range inhibition. Science 351, aaa5694. https://doi.org/10.1126/science.aaa5694

Behr, J., Empson, R.M., Schmitz, D., Gloveli, T., Heinemann, U., 1996. Electrophysiological properties of rat subicular neurons in vitro. Neurosci. Lett. 220, 41–44. https://doi.org/10.1016/S0304-3940(96)13242-0

Behr, J., Gloveli, T., Heinemann, U., 1998. The perforant path projection from the medial entorhinal cortex layer III to the subiculum in the rat combined hippocampal-entorhinal cortex slice: Perforant path in a hippocampal-entorhinal cortex slice preparation. Eur. J. Neurosci. 10, 1011–1018. https://doi.org/10.1046/j.1460-9568.1998.00111.x

Behr, J., Wozny, C., Fidzinski, P., Schmitz, D., 2009. Synaptic plasticity in the subiculum. Prog. Neurobiol. 89, 334–342. https://doi.org/10.1016/j.pneurobio.2009.09.002

Bienkowski, M.S., Bowman, I., Song, M.Y., Gou, L., Ard, T., Cotter, K., Zhu, M., Benavidez, N.L., Yamashita, S., Abu-Jaber, J., Azam, S., Lo, D., Foster, N.N., Hintiryan, H., Dong, H.-W., 2018. Integration of gene expression and brain-wide connectivity reveals the multiscale organization of mouse hippocampal networks. Nat. Neurosci. 21, 1628–1643. https://doi.org/10.1038/s41593-018-0241-y

Bittner, K.C., Milstein, A.D., Grienberger, C., Romani, S., Magee, J.C., 2017. Behavioral time scale synaptic plasticity underlies CA1 place fields. Science 357, 1033–1036. https://doi.org/10.1126/science.aan3846

Boccara, C.N., Sargolini, F., Thoresen, V.H., Solstad, T., Witter, M.P., Moser, E.I., Moser, M.-B., 2010. Grid cells in pre- and parasubiculum. Nat. Neurosci. 13, 987–994. https://doi.org/10.1038/nn.2602

Böhm, C., Peng, Y., Maier, N., Winterer, J., Poulet, J.F.A., Geiger, J.R.P., Schmitz, D., 2015. Functional Diversity of Subicular Principal Cells during Hippocampal Ripples. J. Neurosci. 35, 13608–13618. https://doi.org/10.1523/JNEUROSCI.5034-14.2015

Branco, T., Häusser, M., 2010. The single dendritic branch as a fundamental functional

unit in the nervous system. Curr. Opin. Neurobiol. 20, 494–502. https://doi.org/10.1016/j.conb.2010.07.009

Brandon, M.P., Koenig, J., Leutgeb, S., 2014. Parallel and convergent processing in grid cell, head-direction cell, boundary cell, and place cell networks. WIREs Cogn. Sci. 5, 207–219. https://doi.org/10.1002/wcs.1272

Brotons-Mas, J.R., Montejo, N., O'Mara, S.M., Sanchez-Vives, M.V., 2010. Stability of subicular place fields across multiple light and dark transitions: Stability of subicular place fields. Eur. J. Neurosci. 32, 648–658. https://doi.org/10.1111/j.1460-9568.2010.07308.x

Brun, V.H., Otnæss, M.K., Molden, S., Steffenach, H.-A., Witter, M.P., Moser, M.-B., Moser, E.I., 2002. Place Cells and Place Recognition Maintained by Direct Entorhinal-Hippocampal Circuitry. Science 296, 2243–2246. https://doi.org/10.1126/science.1071089

Burke, S.N., Maurer, A.P., Nematollahi, S., Uprety, A.R., Wallace, J.L., Barnes, C.A., 2011. The influence of objects on place field expression and size in distal hippocampal CA1. Hippocampus 21, 783–801. https://doi.org/10.1002/hipo.20929

Cappaert, N.L.M., Wadman, W.J., Witter, M.P., 2007. Spatiotemporal analyses of interactions between entorhinal and CA1 projections to the subiculum in rat brain slices. Hippocampus 17, 909–921. https://doi.org/10.1002/hipo.20309

Cea-del Rio, C.A., Lawrence, J.J., Erdelyi, F., Szabo, G., McBain, C.J., 2011. Cholinergic modulation amplifies the intrinsic oscillatory properties of CA1 hippocampal cholecystokinin-positive interneurons. J. Physiol. 589, 609–627. https://doi.org/10.1113/jphysiol.2010.199422

Cembrowski, M.S., Phillips, M.G., DiLisio, S.F., Shields, B.C., Winnubst, J., Chandrashekar, J., Bas, E., Spruston, N., 2018a. Dissociable Structural and Functional Hippocampal Outputs via Distinct Subiculum Cell Classes. Cell 173, 1280-1292.e18. https://doi.org/10.1016/j.cell.2018.03.031

Cembrowski, M.S., Spruston, N., 2019. Heterogeneity within classical cell types is the rule: lessons from hippocampal pyramidal neurons. Nat. Rev. Neurosci. 20, 193–204. https://doi.org/10.1038/s41583-019-0125-5

Cembrowski, M.S., Wang, L., Lemire, A.L., Copeland, M., DiLisio, S.F., Clements, J., Spruston, N., 2018b. The subiculum is a patchwork of discrete subregions. eLife 7, e37701. https://doi.org/10.7554/eLife.37701

Cenquizca, L.A., Swanson, L.W., 2007. Spatial organization of direct hippocampal field CA1 axonal projections to the rest of the cerebral cortex. Brain Res. Rev. 56, 1–26. https://doi.org/10.1016/j.brainresrev.2007.05.002

Chew, K.C.M., Kumar, V., Tan, A.Y.Y., 2022. Different Excitation-Inhibition Correlations Between Spontaneous and Tone-evoked Activity in Primary Auditory Cortex Neurons. Neuroscience 496, 205–218. https://doi.org/10.1016/j.neuroscience.2022.06.022

Cho, J., Sharp, P.E., 2001. Head direction, place, and movement correlates for cells in the rat retrosplenial cortex. Behav. Neurosci. 115, 3–25. https://doi.org/10.1037/0735-7044.115.1.3

Cholvin, T., Hainmueller, T., Bartos, M., 2021. The hippocampus converts dynamic entorhinal inputs into stable spatial maps. Neuron 109, 3135-3148.e7. https://doi.org/10.1016/j.neuron.2021.09.019

Chow, B.Y., Han, X., Dobry, A.S., Qian, X., Chuong, A.S., Li, M., Henninger, M.A., Belfort, G.M., Lin, Y., Monahan, P.E., Boyden, E.S., 2010. High-performance genetically targetable optical neural silencing by light-driven proton pumps. Nature 463, 98–102. https://doi.org/10.1038/nature08652

Chuong, A.S., Miri, M.L., Busskamp, V., Matthews, G.A.C., Acker, L.C., Sørensen, A.T., Young, A., Klapoetke, N.C., Henninger, M.A., Kodandaramaiah, S.B., Ogawa, M., Ramanlal, S.B., Bandler, R.C., Allen, B.D., Forest, C.R., Chow, B.Y., Han, X., Lin, Y., Tye, K.M., Roska, B., Cardin, J.A., Boyden, E.S., 2014. Noninvasive optical inhibition with a red-shifted microbial rhodopsin. Nat. Neurosci. 17, 1123–1129. https://doi.org/10.1038/nn.3752

Ciocchi, S., Passecker, J., Malagon-Vina, H., Mikus, N., Klausberger, T., 2015. Selective information routing by ventral hippocampal CA1 projection neurons. Science 348, 560–563. https://doi.org/10.1126/science.aaa3245

Cohen, J.D., Bolstad, M., Lee, A.K., 2017. Experience-dependent shaping of

hippocampal CA1 intracellular activity in novel and familiar environments. eLife 6, e23040. https://doi.org/10.7554/eLife.23040

Commins, S., Aggleton, J.P., O'Mara, S.M., 2002. Physiological evidence for a possible projection from dorsal subiculum to hippocampal area CA1. Exp. Brain Res. 146, 155–160. https://doi.org/10.1007/s00221-002-1158-x

Danielson, N.B., Zaremba, J.D., Kaifosh, P., Bowler, J., Ladow, M., Losonczy, A., 2016. Sublayer-Specific Coding Dynamics during Spatial Navigation and Learning in Hippocampal Area CA1. Neuron 91, 652–665. https://doi.org/10.1016/j.neuron.2016.06.020

Davoudi, H., Foster, D.J., 2019. Acute silencing of hippocampal CA3 reveals a dominant role in place field responses. Nat. Neurosci. 22, 337–342. https://doi.org/10.1038/s41593-018-0321-z

DeBello, W.M., McBride, T.J., Nichols, G.S., Pannoni, K.E., Sanculi, D., Totten, D.J., 2014. Input clustering and the microscale structure of local circuits. Front. Neural Circuits 8. https://doi.org/10.3389/fncir.2014.00112

Ding, S.-L., 2013. Comparative anatomy of the prosubiculum, subiculum, presubiculum, postsubiculum, and parasubiculum in human, monkey, and rodent: Comparative Neuroanatomy of the Subicular Cortices. J. Comp. Neurol. 521, 4145–4162. https://doi.org/10.1002/cne.23416

Dupret, D., O'Neill, J., Pleydell-Bouverie, B., Csicsvari, J., 2010. The reorganization and reactivation of hippocampal maps predict spatial memory performance. Nat. Neurosci. 13, 995–1002. https://doi.org/10.1038/nn.2599

Eichenbaum, H., 2014. Time cells in the hippocampus: a new dimension for mapping memories. Nat. Rev. Neurosci. 15, 732–744. https://doi.org/10.1038/nrn3827

Eichenbaum, H., Dudchenko, P., Wood, E., Shapiro, M., Tanila, H., 1999. The Hippocampus, Memory, and Place Cells. Neuron 23, 209–226. https://doi.org/10.1016/S0896-6273(00)80773-4

Ekstrom, A.D., Meltzer, J., McNaughton, B.L., Barnes, C.A., 2001. NMDA Receptor Antagonism Blocks Experience-Dependent Expansion of Hippocampal "Place

Fields.” Neuron 31, 631–638. https://doi.org/10.1016/S0896-6273(01)00401-9

Engel, J., 2001. Mesial Temporal Lobe Epilepsy: What Have We Learned? The Neuroscientist 7, 340–352. https://doi.org/10.1177/107385840100700410

Epsztein, J., Brecht, M., Lee, A.K., 2011. Intracellular Determinants of Hippocampal CA1 Place and Silent Cell Activity in a Novel Environment. Neuron 70, 109–120. https://doi.org/10.1016/j.neuron.2011.03.006

Fanselow, M.S., Dong, H.-W., 2010. Are the Dorsal and Ventral Hippocampus Functionally Distinct Structures? Neuron 65, 7–19. https://doi.org/10.1016/j.neuron.2009.11.031

Fei, F., Wang, X., Xu, C., Shi, J., Gong, Y., Cheng, H., Lai, N., Ruan, Y., Ding, Y., Wang, S., Chen, Z., Wang, Y., 2022. Discrete subicular circuits control generalization of hippocampal seizures. Nat. Commun. 13, 5010. https://doi.org/10.1038/s41467-022-32742-x

Ferrante, M., Tahvildari, B., Duque, A., Hadzipasic, M., Salkoff, D., Zagha, E.W., Hasselmo, M.E., McCormick, D.A., 2016. Distinct Functional Groups Emerge from the Intrinsic Properties of Molecularly Identified Entorhinal Interneurons and Principal Cells. Cereb. Cortex bhw143. https://doi.org/10.1093/cercor/bhw143

Fidzinski, P., Shor, O., Behr, J., 2008. Target-cell-specific bidirectional synaptic plasticity at hippocampal output synapses. Eur. J. Neurosci. 27, 1111–1118. https://doi.org/10.1111/j.1460-9568.2008.06089.x

Fidzinski, P., Wawra, M., Bartsch, J., Heinemann, U., Behr, J., 2012. High-frequency stimulation of the temporoammonic pathway induces input-specific long-term potentiation in subicular bursting cells. Brain Res. 1430, 1–7. https://doi.org/10.1016/j.brainres.2011.10.040

Fidzinski, P., Wawra, M., Dugladze, T., Gloveli, T., Heinemann, U., Behr, J., 2011. Low-frequency stimulation of the temporoammonic pathway induces heterosynaptic disinhibition in the subiculum. Hippocampus 21, 733–743. https://doi.org/10.1002/hipo.20791

Francavilla, R., Villette, V., Luo, X., Chamberland, S., Muñoz-Pino, E., Camiré, O.,

Wagner, K., Kis, V., Somogyi, P., Topolnik, L., 2018. Connectivity and network state-dependent recruitment of long-range VIP-GABAergic neurons in the mouse hippocampus. Nat. Commun. 9, 5043. https://doi.org/10.1038/s41467-018-07162-5

Franklin, K.B.J., Paxinos, G., 2008. The mouse brain in stereotaxic coordinates, 3. ed. ed. Elsevier, AP, Amsterdam.

Franklin, T.B., Silva, B.A., Perova, Z., Marrone, L., Masferrer, M.E., Zhan, Y., Kaplan, A., Greetham, L., Verrechia, V., Halman, A., Pagella, S., Vyssotski, A.L., Illarionova, A., Grinevich, V., Branco, T., Gross, C.T., 2017. Prefrontal cortical control of a brainstem social behavior circuit. Nat. Neurosci. 20, 260–270. https://doi.org/10.1038/nn.4470

Frost, B.E., Martin, S.K., Cafalchio, M., Islam, M.N., Aggleton, J.P., O'Mara, S.M., 2021. Anterior Thalamic Inputs Are Required for Subiculum Spatial Coding, with Associated Consequences for Hippocampal Spatial Memory. J. Neurosci. 41, 6511–6525. https://doi.org/10.1523/JNEUROSCI.2868-20.2021

Fuentealba, P., Tomioka, R., Dalezios, Y., Márton, L.F., Studer, M., Rockland, K., Klausberger, T., Somogyi, P., 2008. Rhythmically Active Enkephalin-Expressing GABAergic Cells in the CA1 Area of the Hippocampus Project to the Subiculum and Preferentially Innervate Interneurons. J. Neurosci. 28, 10017–10022. https://doi.org/10.1523/JNEUROSCI.2052-08.2008

Fuhrmann, F., Justus, D., Sosulina, L., Kaneko, H., Beutel, T., Friedrichs, D., Schoch, S., Schwarz, M.K., Fuhrmann, M., Remy, S., 2015. Locomotion, Theta Oscillations, and the Speed-Correlated Firing of Hippocampal Neurons Are Controlled by a Medial Septal Glutamatergic Circuit. Neuron 86, 1253–1264. https://doi.org/10.1016/j.neuron.2015.05.001

Fyhn, M., Hafting, T., Treves, A., Moser, M.-B., Moser, E.I., 2007. Hippocampal remapping and grid realignment in entorhinal cortex. Nature 446, 190–194. https://doi.org/10.1038/nature05601

Galani, R., Weiss, I., Cassel, J.-C., Kelche, C., 1998. Spatial memory, habituation, and reactions to spatial and nonspatial changes in rats with selective lesions of the hippocampus, the entorhinal cortex or the subiculum. Behav. Brain Res. 96, 1–12.

https://doi.org/10.1016/S0166-4328(97)00197-6

Gauthier, J.L., Tank, D.W., 2018. A Dedicated Population for Reward Coding in the Hippocampus. Neuron 99, 179-193.e7. https://doi.org/10.1016/j.neuron.2018.06.008

Geisler, C., Robbe, D., Zugaro, M., Sirota, A., Buzsáki, G., 2007. Hippocampal place cell assemblies are speed-controlled oscillators. Proc. Natl. Acad. Sci. 104, 8149–8154. https://doi.org/10.1073/pnas.0610121104

Gigg, J., Finch, D.M., O'Mara, S.M., 2000. Responses of rat subicular neurons to convergent stimulation of lateral entorhinal cortex and CA1 in vivo. Brain Res. 884, 35–50. https://doi.org/10.1016/S0006-8993(00)02878-X

Giocomo, L.M., Stensola, T., Bonnevie, T., Van Cauter, T., Moser, M.-B., Moser, E.I., 2014. Topography of Head Direction Cells in Medial Entorhinal Cortex. Curr. Biol. 24, 252–262. https://doi.org/10.1016/j.cub.2013.12.002

Giovannucci, A., Friedrich, J., Gunn, P., Kalfon, J., Brown, B.L., Koay, S.A., Taxidis, J., Najafi, F., Gauthier, J.L., Zhou, P., Khakh, B.S., Tank, D.W., Chklovskii, D.B., Pnevmatikakis, E.A., 2019. CaImAn an open source tool for scalable calcium imaging data analysis. eLife 8, e38173. https://doi.org/10.7554/eLife.38173

Góis, Z.H.T.D., Tort, A.B.L., 2018. Characterizing Speed Cells in the Rat Hippocampus. Cell Rep. 25, 1872-1884.e4. https://doi.org/10.1016/j.celrep.2018.10.054

Golding, N.L., Jung, H., Mickus, T., Spruston, N., 1999. Dendritic Calcium Spike Initiation and Repolarization Are Controlled by Distinct Potassium Channel Subtypes in CA1 Pyramidal Neurons. J. Neurosci. 19, 8789–8798. https://doi.org/10.1523/JNEUROSCI.19-20-08789.1999

Golding, N.L., Mickus, T.J., Katz, Y., Kath, W.L., Spruston, N., 2005. Factors mediating powerful voltage attenuation along CA1 pyramidal neuron dendrites: Voltage attenuation in CA1 dendrites. J. Physiol. 568, 69–82. https://doi.org/10.1113/jphysiol.2005.086793

Gomez, J.L., Bonaventura, J., Lesniak, W., Mathews, W.B., Sysa-Shah, P., Rodriguez, L.A., Ellis, R.J., Richie, C.T., Harvey, B.K., Dannals, R.F., Pomper, M.G., Bonci, A.,

Michaelides, M., 2017. Chemogenetics revealed: DREADD occupancy and activation via converted clozapine. Science 357, 503–507. https://doi.org/10.1126/science.aan2475

Graves, A.R., Moore, S.J., Bloss, E.B., Mensh, B.D., Kath, W.L., Spruston, N., 2012. Hippocampal Pyramidal Neurons Comprise Two Distinct Cell Types that Are Countermodulated by Metabotropic Receptors. Neuron 76, 776–789. https://doi.org/10.1016/j.neuron.2012.09.036

Greene, J.R.T., Totterdell, S., 1997. Morphology and distribution of electrophysiologically defined classes of pyramidal and nonpyramidal neurons in rat ventral subiculum in vitro. J. Comp. Neurol. 380, 395–408. https://doi.org/10.1002/(SICI)1096-9861(19970414)380:3<395::AID-CNE8>3.0.CO;2-Y

Gremel, C.M., Chancey, J.H., Atwood, B.K., Luo, G., Neve, R., Ramakrishnan, C., Deisseroth, K., Lovinger, D.M., Costa, R.M., 2016. Endocannabinoid Modulation of Orbitostriatal Circuits Gates Habit Formation. Neuron 90, 1312–1324. https://doi.org/10.1016/j.neuron.2016.04.043

Grienberger, C., Magee, J.C., 2022. Entorhinal cortex directs learning-related changes in CA1 representations. Nature 611, 554–562. https://doi.org/10.1038/s41586-022-05378-6

Hafting, T., Fyhn, M., Molden, S., Moser, M.-B., Moser, E.I., 2005. Microstructure of a spatial map in the entorhinal cortex. Nature 436, 801–806. https://doi.org/10.1038/nature03721

Halabisky, B., Shen, F., Huguenard, J.R., Prince, D.A., 2006. Electrophysiological Classification of Somatostatin-Positive Interneurons in Mouse Sensorimotor Cortex. J. Neurophysiol. 96, 834–845. https://doi.org/10.1152/jn.01079.2005

Hangya, B., Li, Y., Muller, R.U., Czurkó, A., 2010. Complementary spatial firing in place cell-interneuron pairs: Place cell-interneuron spatial correlation. J. Physiol. 588, 4165–4175. https://doi.org/10.1113/jphysiol.2010.194274

Harris, E., Witter, M.P., Weinstein, G., Stewart, M., 2001. Intrinsic connectivity of the rat subiculum: I. Dendritic morphology and patterns of axonal arborization by pyramidal neurons. J. Comp. Neurol. 435, 490–505.

https://doi.org/10.1002/cne.1046

Harris, K.D., Hochgerner, H., Skene, N.G., Magno, L., Katona, L., Gonzales, C.B., Somogyi, P., Kessaris, N., Linnarsson, S., Hjerling-Leffler, J., 2017. Classes and continua of hippocampal CA1 inhibitory neurons revealed by single-cell transcriptomics (preprint). Neuroscience. https://doi.org/10.1101/143354

Harvey, C.D., Collman, F., Dombeck, D.A., Tank, D.W., 2009. Intracellular dynamics of hippocampal place cells during virtual navigation. Nature 461, 941–946. https://doi.org/10.1038/nature08499

Hattox, A.M., Nelson, S.B., 2007. Layer V Neurons in Mouse Cortex Projecting to Different Targets Have Distinct Physiological Properties. J. Neurophysiol. 98, 3330–3340. https://doi.org/10.1152/jn.00397.2007

Henriksen, E.J., Colgin, L.L., Barnes, C.A., Witter, M.P., Moser, M.-B., Moser, E.I., 2010. Spatial Representation along the Proximodistal Axis of CA1. Neuron 68, 127–137. https://doi.org/10.1016/j.neuron.2010.08.042

Hernández-Frausto, M., Bilash, O.M., Masurkar, A.V., Basu, J., 2023. Local and long-range GABAergic circuits in hippocampal area CA1 and their link to Alzheimer's disease. Front. Neural Circuits 17, 1223891. https://doi.org/10.3389/fncir.2023.1223891

Hinman, J.R., Brandon, M.P., Climer, J.R., Chapman, G.W., Hasselmo, M.E., 2016. Multiple Running Speed Signals in Medial Entorhinal Cortex. Neuron 91, 666–679. https://doi.org/10.1016/j.neuron.2016.06.027

Ho, J., Tumkaya, T., Aryal, S., Choi, H., Claridge-Chang, A., 2019. Moving beyond P values: data analysis with estimation graphics. Nat. Methods 16, 565–566. https://doi.org/10.1038/s41592-019-0470-3

Hollup, S.A., Molden, S., Donnett, J.G., Moser, M.-B., Moser, E.I., 2001. Accumulation of Hippocampal Place Fields at the Goal Location in an Annular Watermaze Task. J. Neurosci. 21, 1635–1644. https://doi.org/10.1523/JNEUROSCI.21-05-01635.2001

Huh, C.Y.L., Goutagny, R., Williams, S., 2010. Glutamatergic Neurons of the Mouse

Medial Septum and Diagonal Band of Broca Synaptically Drive Hippocampal Pyramidal Cells: Relevance for Hippocampal Theta Rhythm. J. Neurosci. 30, 15951–15961. https://doi.org/10.1523/JNEUROSCI.3663-10.2010

Isaacson, J.S., Scanziani, M., 2011. How Inhibition Shapes Cortical Activity. Neuron 72, 231–243. https://doi.org/10.1016/j.neuron.2011.09.027

Ishihara, Y., Fukuda, T., 2016. Immunohistochemical investigation of the internal structure of the mouse subiculum. Neuroscience 337, 242–266. https://doi.org/10.1016/j.neuroscience.2016.09.027

Iwase, M., Kitanishi, T., Mizuseki, K., 2020. Cell type, sub-region, and layer-specific speed representation in the hippocampal–entorhinal circuit. Sci. Rep. 10, 1407. https://doi.org/10.1038/s41598-020-58194-1

Jacobs, L.F., Schenk, F., 2003. Unpacking the cognitive map: The parallel map theory of hippocampal function. Psychol. Rev. 110, 285–315. https://doi.org/10.1037/0033-295X.110.2.285

Jankowski, M.M., Islam, M.N., Wright, N.F., Vann, S.D., Erichsen, J.T., Aggleton, J.P., O'Mara, S.M., 2014. Nucleus reuniens of the thalamus contains head direction cells. eLife 3, e03075. https://doi.org/10.7554/eLife.03075

Jarsky, T., Mady, R., Kennedy, B., Spruston, N., 2008. Distribution of bursting neurons in the CA1 region and the subiculum of the rat hippocampus. J. Comp. Neurol. 506, 535–547. https://doi.org/10.1002/cne.21564

Jeong, N., Singer, A.C., 2022. Learning from inhibition: Functional roles of hippocampal CA1 inhibition in spatial learning and memory. Curr. Opin. Neurobiol. 76, 102604. https://doi.org/10.1016/j.conb.2022.102604

Jinno, S., Klausberger, T., Marton, L.F., Dalezios, Y., Roberts, J.D.B., Fuentealba, P., Bushong, E.A., Henze, D., Buzsáki, G., Somogyi, P., 2007. Neuronal Diversity in GABAergic Long-Range Projections from the Hippocampus. J. Neurosci. 27, 8790–8804. https://doi.org/10.1523/JNEUROSCI.1847-07.2007

Jung, H., Staff, N.P., Spruston, N., 2001. Action Potential Bursting in Subicular Pyramidal Neurons Is Driven by a Calcium Tail Current. J. Neurosci. 21, 3312–

3321. https://doi.org/10.1523/JNEUROSCI.21-10-03312.2001

Justus, D., Dalügge, D., Bothe, S., Fuhrmann, F., Hannes, C., Kaneko, H., Friedrichs, D., Sosulina, L., Schwarz, I., Elliott, D.A., Schoch, S., Bradke, F., Schwarz, M.K., Remy, S., 2017. Glutamatergic synaptic integration of locomotion speed via septoentorhinal projections. Nat. Neurosci. 20, 16–19. https://doi.org/10.1038/nn.4447

Kim, E.J., Zhang, Z., Huang, L., Ito-Cole, T., Jacobs, M.W., Juavinett, A.L., Senturk, G., Hu, M., Ku, M., Ecker, J.R., Callaway, E.M., 2020. Extraction of Distinct Neuronal Cell Types from within a Genetically Continuous Population. Neuron 107, 274-282.e6. https://doi.org/10.1016/j.neuron.2020.04.018

Kim, S.M., Ganguli, S., Frank, L.M., 2012. Spatial Information Outflow from the Hippocampal Circuit: Distributed Spatial Coding and Phase Precession in the Subiculum. J. Neurosci. 32, 11539–11558. https://doi.org/10.1523/JNEUROSCI.5942-11.2012

Kim, Y., Spruston, N., 2012. Target-specific output patterns are predicted by the distribution of regular-spiking and bursting pyramidal neurons in the subiculum. Hippocampus 22, 693–706. https://doi.org/10.1002/hipo.20931

Kinnavane, L., Vann, S.D., Nelson, A.J.D., O'Mara, S.M., Aggleton, J.P., 2018. Collateral Projections Innervate the Mammillary Bodies and Retrosplenial Cortex: A New Category of Hippocampal Cells. eneuro 5, ENEURO.0383-17.2018. https://doi.org/10.1523/ENEURO.0383-17.2018

Kitanishi, T., Umaba, R., Mizuseki, K., 2021. Robust information routing by dorsal subiculum neurons. Sci. Adv. 7, eabf1913. https://doi.org/10.1126/sciadv.abf1913

Kloosterman, F., Witter, M.P., Van Haeften, T., 2003. Topographical and laminar organization of subicular projections to the parahippocampal region of the rat. J. Comp. Neurol. 455, 156–171. https://doi.org/10.1002/cne.10472

Knopp, A., Frahm, C., Fidzinski, P., Witte, O.W., Behr, J., 2008. Loss of GABAergic neurons in the subiculum and its functional implications in temporal lobe epilepsy. Brain 131, 1516–1527. https://doi.org/10.1093/brain/awn095

Knopp, A., Kivi, A., Wozny, C., Heinemann, U., Behr, J., 2005. Cellular and network properties of the subiculum in the pilocarpine model of temporal lobe epilepsy. J. Comp. Neurol. 483, 476–488. https://doi.org/10.1002/cne.20460

Komendantov, A.O., Venkadesh, S., Rees, C.L., Wheeler, D.W., Hamilton, D.J., Ascoli, G.A., 2019. Quantitative firing pattern phenotyping of hippocampal neuron types. Sci. Rep. 9, 17915. https://doi.org/10.1038/s41598-019-52611-w

Kropff, E., Carmichael, J.E., Moser, M.-B., Moser, E.I., 2015. Speed cells in the medial entorhinal cortex. Nature 523, 419–424. https://doi.org/10.1038/nature14622

Larkum, M.E., Nevian, T., 2008. Synaptic clustering by dendritic signalling mechanisms. Curr. Opin. Neurobiol. 18, 321–331. https://doi.org/10.1016/j.conb.2008.08.013

Larkum, M.E., Nevian, T., Sandler, M., Polsky, A., Schiller, J., 2009. Synaptic Integration in Tuft Dendrites of Layer 5 Pyramidal Neurons: A New Unifying Principle. Science 325, 756–760. https://doi.org/10.1126/science.1171958

Leão, R.N., Mikulovic, S., Leão, K.E., Munguba, H., Gezelius, H., Enjin, A., Patra, K., Eriksson, A., Loew, L.M., Tort, A.B.L., Kullander, K., 2012. OLM interneurons differentially modulate CA3 and entorhinal inputs to hippocampal CA1 neurons. Nat. Neurosci. 15, 1524–1530. https://doi.org/10.1038/nn.3235

Ledergerber, D., Battistin, C., Blackstad, J.S., Gardner, R.J., Witter, M.P., Moser, M.-B., Roudi, Y., Moser, E.I., 2021. Task-dependent mixed selectivity in the subiculum. Cell Rep. 35, 109175. https://doi.org/10.1016/j.celrep.2021.109175

Lee, S.-M., Seol, J.-M., Lee, I., 2022. Subicular neurons represent multiple variables of a hippocampal-dependent task by using theta rhythm. PLOS Biol. 20, e3001546. https://doi.org/10.1371/journal.pbio.3001546

Leutgeb, S., Leutgeb, J.K., Moser, M.-B., Moser, E.I., 2005. Place cells, spatial maps and the population code for memory. Curr. Opin. Neurobiol. 15, 738–746. https://doi.org/10.1016/j.conb.2005.10.002

Lever, C., Burton, S., Jeewajee, A., O'Keefe, J., Burgess, N., 2009. Boundary Vector Cells in the Subiculum of the Hippocampal Formation. J. Neurosci. 29, 9771–9777. https://doi.org/10.1523/JNEUROSCI.1319-09.2009

Lin, X., Amalraj, M., Blanton, C., Avila, B., Holmes, T.C., Nitz, D.A., Xu, X., 2021. Noncanonical projections to the hippocampal CA3 regulate spatial learning and memory by modulating the feedforward hippocampal trisynaptic pathway. PLOS Biol. 19, e3001127. https://doi.org/10.1371/journal.pbio.3001127

Logothetis, N.K., Eschenko, O., Murayama, Y., Augath, M., Steudel, T., Evrard, H.C., Besserve, M., Oeltermann, A., 2012. Hippocampal–cortical interaction during periods of subcortical silence. Nature 491, 547–553. https://doi.org/10.1038/nature11618

London, M., Häusser, M., 2005. DENDRITIC COMPUTATION.

Losonczy, A., Magee, J.C., 2006. Integrative Properties of Radial Oblique Dendrites in Hippocampal CA1 Pyramidal Neurons. Neuron 50, 291–307. https://doi.org/10.1016/j.neuron.2006.03.016

MacLaren, D.A.A., Browne, R.W., Shaw, J.K., Krishnan Radhakrishnan, S., Khare, P., España, R.A., Clark, S.D., 2016. Clozapine N-Oxide Administration Produces Behavioral Effects in Long–Evans Rats: Implications for Designing DREADD Experiments. eneuro 3, ENEURO.0219-16.2016. https://doi.org/10.1523/ENEURO.0219-16.2016

Magee, J.C., 2000. Dendritic integration of excitatory synaptic input. Nat. Rev. Neurosci. 1, 181–190. https://doi.org/10.1038/35044552

Magee, J.C., Cook, E.P., 2000. Somatic EPSP amplitude is independent of synapse location in hippocampal pyramidal neurons. Nat. Neurosci. 3, 895–903. https://doi.org/10.1038/78800

Mahler, S.V., Vazey, E.M., Beckley, J.T., Keistler, C.R., McGlinchey, E.M., Kaufling, J., Wilson, S.P., Deisseroth, K., Woodward, J.J., Aston-Jones, G., 2014. Designer receptors show role for ventral pallidum input to ventral tegmental area in cocaine seeking. Nat. Neurosci. 17, 577–585. https://doi.org/10.1038/nn.3664

Mahn, M., Prigge, M., Ron, S., Levy, R., Yizhar, O., 2016. Biophysical constraints of optogenetic inhibition at presynaptic terminals. Nat. Neurosci. 19, 554–556. https://doi.org/10.1038/nn.4266

Mahn, M., Saraf-Sinik, I., Patil, P., Pulin, M., Bitton, E., Karalis, N., Bruentgens, F., Palgi, S., Gat, A., Dine, J., Wietek, J., Davidi, I., Levy, R., Litvin, A., Zhou, F., Sauter, K., Soba, P., Schmitz, D., Lüthi, A., Rost, B.R., Wiegert, J.S., Yizhar, O., 2021. Efficient optogenetic silencing of neurotransmitter release with a mosquito rhodopsin. Neuron 109, 1621-1635.e8. https://doi.org/10.1016/j.neuron.2021.03.013

Major, G., Larkum, M.E., Schiller, J., 2013. Active Properties of Neocortical Pyramidal Neuron Dendrites. Annu. Rev. Neurosci. 36, 1–24. https://doi.org/10.1146/annurev-neuro-062111-150343

Major, G., Polsky, A., Denk, W., Schiller, J., Tank, D.W., 2008. Spatiotemporally Graded NMDA Spike/Plateau Potentials in Basal Dendrites of Neocortical Pyramidal Neurons. J. Neurophysiol. 99, 2584–2601. https://doi.org/10.1152/jn.00011.2008

Manu, M., Baccus, S.A., 2011. Disinhibitory gating of retinal output by transmission from an amacrine cell. Proc. Natl. Acad. Sci. 108, 18447–18452. https://doi.org/10.1073/pnas.1107994108

Markus, E., Qin, Y., Leonard, B., Skaggs, W., McNaughton, B., Barnes, C., 1995. Interactions between location and task affect the spatial and directional firing of hippocampal neurons. J. Neurosci. 15, 7079–7094. https://doi.org/10.1523/JNEUROSCI.15-11-07079.1995

Masurkar, A.V., Tian, C., Warren, R., Reyes, I., Lowes, D.C., Brann, D.H., Siegelbaum, S.A., 2020. Postsynaptic integrative properties of dorsal CA1 pyramidal neuron subpopulations. J. Neurophysiol. 123, 980–992. https://doi.org/10.1152/jn.00397.2019

Mathis, A., Mamidanna, P., Cury, K.M., Abe, T., Murthy, V.N., Mathis, M.W., Bethge, M., 2018. DeepLabCut: markerless pose estimation of user-defined body parts with deep learning. Nat. Neurosci. 21, 1281–1289. https://doi.org/10.1038/s41593-018-0209-y

Matsumoto, N., Kitanishi, T., Mizuseki, K., 2019. The subiculum: Unique hippocampal hub and more. Neurosci. Res. 143, 1–12. https://doi.org/10.1016/j.neures.2018.08.002

Mattia, D., Kawasaki, H., Avoli, M., 1997. In vitro electrophysiology of rat subicular bursting neurons. Hippocampus 7, 48–57. https://doi.org/10.1002/(SICI)1098-1063(1997)7:1<48::AID-HIPO5>3.0.CO;2-3

McNaughton, B.L., Barnes, C.A., O'Keefe, J., 1983. The contributions of position, direction, and velocity to single unit activity in the hippocampus of freely-moving rats. Exp. Brain Res. 52. https://doi.org/10.1007/BF00237147

Mcnaughton, N., 2006. The role of the subiculum within the behavioural inhibition system. Behav. Brain Res. 174, 232–250. https://doi.org/10.1016/j.bbr.2006.05.037

McNaughton, N., 2006. The role of the subiculum within the behavioural inhibition system. Behav. Brain Res. 174, 232–250. https://doi.org/10.1016/j.bbr.2006.05.037

Melzer, S., Michael, M., Caputi, A., Eliava, M., Fuchs, E.C., Whittington, M.A., Monyer, H., 2012. Long-Range–Projecting GABAergic Neurons Modulate Inhibition in Hippocampus and Entorhinal Cortex. Science 335, 1506–1510. https://doi.org/10.1126/science.1217139

Migliore, M., Ferrante, M., Ascoli, G.A., 2005. Signal Propagation in Oblique Dendrites of CA1 Pyramidal Cells. J. Neurophysiol. 94, 4145–4155. https://doi.org/10.1152/jn.00521.2005

Miles, R., Tóth, K., Gulyás, A.I., Hájos, N., Freund, T.F., 1996. Differences between Somatic and Dendritic Inhibition in the Hippocampus. Neuron 16, 815–823. https://doi.org/10.1016/S0896-6273(00)80101-4

Morgenstern, N.A., Bourg, J., Petreanu, L., 2016. Multilaminar networks of cortical neurons integrate common inputs from sensory thalamus. Nat. Neurosci. 19, 1034–1040. https://doi.org/10.1038/nn.4339

Morris, R.G.M., Schenk, F., Tweedie, F., Jarrard, L.E., 1990. Ibotenate Lesions of Hippocampus and/or Subiculum: Dissociating Components of Allocentric Spatial Learning. Eur. J. Neurosci. 2, 1016–1028. https://doi.org/10.1111/j.1460-9568.1990.tb00014.x

Moser, E.I., Kropff, E., Moser, M.-B., 2008. Place Cells, Grid Cells, and the Brain's Spatial Representation System. Annu. Rev. Neurosci. 31, 69–89.

https://doi.org/10.1146/annurev.neuro.31.061307.090723

Müller, C., Beck, H., Coulter, D., Remy, S., 2012. Inhibitory Control of Linear and Supralinear Dendritic Excitation in CA1 Pyramidal Neurons. Neuron 75, 851–864. https://doi.org/10.1016/j.neuron.2012.06.025

Muller, R., Kubie, J., 1987. The effects of changes in the environment on the spatial firing of hippocampal complex-spike cells. J. Neurosci. 7, 1951–1968. https://doi.org/10.1523/JNEUROSCI.07-07-01951.1987

Naber, P.A., Lopes da Silva, F.H., Witter, M.P., 2001. Reciprocal connections between the entorhinal cortex and hippocampal fields CA1 and the subiculum are in register with the projections from CA1 to the subiculum. Hippocampus 11, 99–104. https://doi.org/10.1002/hipo.1028

Naber, P.A., Witter, M.P., 1998. Subicular efferents are organized mostly as parallel projections: A double-labeling, retrograde-tracing study in the rat. J. Comp. Neurol. 393, 284–297. https://doi.org/10.1002/(SICI)1096-9861(19980413)393:3<284::AID-CNE2>3.0.CO;2-Y

Nakashiba, T., Young, J.Z., McHugh, T.J., Buhl, D.L., Tonegawa, S., 2008. Transgenic Inhibition of Synaptic Transmission Reveals Role of CA3 Output in Hippocampal Learning. Science 319, 1260–1264. https://doi.org/10.1126/science.1151120

Namura, S., Takada, M., Kikuchi, H., Mizuno, N., 1994. Topographical organization of subicular neurons projecting to subcortical regions. Brain Res. Bull. 35, 221–231. https://doi.org/10.1016/0361-9230(94)90126-0

Navratilova, Z., Hoang, L.T., Schwindel, C.D., Tatsuno, M., McNaughton, B.L., 2012. Experience-dependent firing rate remapping generates directional selectivity in hippocampal place cells. Front. Neural Circuits 6. https://doi.org/10.3389/fncir.2012.00006

Neef, J., Urban, N.T., Ohn, T.-L., Frank, T., Jean, P., Hell, S.W., Willig, K.I., Moser, T., 2018. Quantitative optical nanophysiology of Ca2+ signaling at inner hair cell active zones. Nat. Commun. 9, 290. https://doi.org/10.1038/s41467-017-02612-y

Nelson, A.J.D., Kinnavane, L., Amin, E., O'Mara, S.M., Aggleton, J.P., 2020.

Deconstructing the Direct Reciprocal Hippocampal-Anterior Thalamic Pathways for Spatial Learning. J. Neurosci. 40, 6978–6990. https://doi.org/10.1523/JNEUROSCI.0874-20.2020

Nichol, H., Amilhon, B., Manseau, F., Badrinarayanan, S., Williams, S., 2018. Electrophysiological and Morphological Characterization of Chrna2 Cells in the Subiculum and CA1 of the Hippocampus: An Optogenetic Investigation. Front. Cell. Neurosci. 12, 32. https://doi.org/10.3389/fncel.2018.00032

Nusser, Z., 2009. Variability in the subcellular distribution of ion channels increases neuronal diversity. Trends Neurosci. 32, 267–274. https://doi.org/10.1016/j.tins.2009.01.003

O'Keefe, J., Dostrovsky, J., 1971. The hippocampus as a spatial map. Preliminary evidence from unit activity in the freely-moving rat. Brain Res. 34, 171–175. https://doi.org/10.1016/0006-8993(71)90358-1

O'Keefe, J., Nadel, L., 1978. The hippocampus as a cognitive map. Clarendon Press ; Oxford University Press, Oxford : New York.

Olson, J.M., Tongprasearth, K., Nitz, D.A., 2017. Subiculum neurons map the current axis of travel. Nat. Neurosci. 20, 170–172. https://doi.org/10.1038/nn.4464

O'Mara, S., 2005. The subiculum: what it does, what it might do, and what neuroanatomy has yet to tell us. J. Anat. 207, 271–282. https://doi.org/10.1111/j.1469-7580.2005.00446.x

O'Mara, S.M., Commins, S., Anderson, M., Gigg, J., 2001. The subiculum: a review of form, physiology and function. Prog. Neurobiol. 64, 129–155. https://doi.org/10.1016/S0301-0082(00)00054-X

O'Mara, S.M., Sanchez-Vives, M.V., Brotons-Mas, J.R., O'Hare, E., 2009. Roles for the subiculum in spatial information processing, memory, motivation and the temporal control of behaviour. Prog. Neuropsychopharmacol. Biol. Psychiatry 33, 782–790. https://doi.org/10.1016/j.pnpbp.2009.03.040

Oswald, C.J., Good, M., 2000. The effects of combined lesions of the subicular complex and the entorhinal cortex on two forms of spatial navigation in the water maze.

Behav. Neurosci. 114, 211–217. https://doi.org/10.1037//0735-7044.114.1.211

Perrenoud, Q., Rossier, J., Geoffroy, H., Vitalis, T., Gallopin, T., 2013. Diversity of GABAergic Interneurons in Layer VIa and VIb of Mouse Barrel Cortex. Cereb. Cortex 23, 423–441. https://doi.org/10.1093/cercor/bhs032

Péterfi, Z., Urbán, G.M., Papp, O.I., Németh, B., Monyer, H., Szabó, G., Erdélyi, F., Mackie, K., Freund, T.F., Hájos, N., Katona, I., 2012. Endocannabinoid-Mediated Long-Term Depression of Afferent Excitatory Synapses in Hippocampal Pyramidal Cells and GABAergic Interneurons. J. Neurosci. 32, 14448–14463. https://doi.org/10.1523/JNEUROSCI.1676-12.2012

Petreanu, L., Mao, T., Sternson, S.M., Svoboda, K., 2009. The subcellular organization of neocortical excitatory connections. Nature 457, 1142–1145. https://doi.org/10.1038/nature07709

Pettit, N.L., Yuan, X.C., Harvey, C.D., 2022. Hippocampal place codes are gated by behavioral engagement. Nat. Neurosci. 25, 561–566. https://doi.org/10.1038/s41593-022-01050-4

Poleg-Polsky, A., 2015. Effects of Neural Morphology and Input Distribution on Synaptic Processing by Global and Focal NMDA-Spikes. PLOS ONE 10, e0140254. https://doi.org/10.1371/journal.pone.0140254

Potvin, O., Doré, F.Y., Goulet, S., 2009. Lesions of the dorsal subiculum and the dorsal hippocampus impaired pattern separation in a task using distinct and overlapping visual stimuli. Neurobiol. Learn. Mem. 91, 287–297. https://doi.org/10.1016/j.nlm.2008.10.003

Potvin, O., Lemay, F., Dion, M., Corado, G., Doré, F.Y., Goulet, S., 2010. Contribution of the dorsal subiculum to memory for temporal order and novelty detection using objects, odors, or spatial locations in the rat. Neurobiol. Learn. Mem. 93, 330–336. https://doi.org/10.1016/j.nlm.2009.11.007

Poulter, S., Lee, S.A., Dachtler, J., Wills, T.J., Lever, C., 2021. Vector trace cells in the subiculum of the hippocampal formation. Nat. Neurosci. 24, 266–275. https://doi.org/10.1038/s41593-020-00761-w

Prida, L.M., 2003. Control of bursting by local inhibition in the rat subiculum *in vitro*. J. Physiol. 549, 219–230. https://doi.org/10.1113/jphysiol.2003.039305

Prönneke, A., Scheuer, B., Wagener, R.J., Möck, M., Witte, M., Staiger, J.F., 2015. Characterizing VIP Neurons in the Barrel Cortex of VIPcre/tdTomato Mice Reveals Layer-Specific Differences. Cereb. Cortex 25, 4854–4868. https://doi.org/10.1093/cercor/bhv202

Qiu, S., Hu, Y., Huang, Yiming, Gao, T., Wang, Xiaofei, Wang, Danying, Ren, B., Shi, X., Chen, Y., Wang, Xinran, Wang, Dan, Han, L., Liang, Y., Liu, D., Liu, Q., Deng, L., Chen, Z., Zhan, L., Chen, T., Huang, Yuzhe, Wu, Q., Xie, T., Qian, L., Jin, C., Huang, J., Deng, W., Jiang, T., Li, X., Jia, X., Yuan, J., Li, A., Yan, J., Xu, N., Xu, L., Luo, Q., Poo, M.-M., Sun, Y., Li, C.T., Yao, H., Gong, H., Sun, Y.-G., Xu, C., 2024. Whole-brain spatial organization of hippocampal single-neuron projectomes. Science 383, eadj9198. https://doi.org/10.1126/science.adj9198

Raimondo, J.V., Kay, L., Ellender, T.J., Akerman, C.J., 2012. Optogenetic silencing strategies differ in their effects on inhibitory synaptic transmission. Nat. Neurosci. 15, 1102–1104. https://doi.org/10.1038/nn.3143

Remy, S., Spruston, N., 2007. Dendritic spikes induce single-burst long-term potentiation. Proc. Natl. Acad. Sci. 104, 17192–17197. https://doi.org/10.1073/pnas.0707919104

Rost, B.R., Wietek, J., Yizhar, O., Schmitz, D., 2022. Optogenetics at the presynapse. Nat. Neurosci. 25, 984–998. https://doi.org/10.1038/s41593-022-01113-6

Roth, B.L., 2016. DREADDs for Neuroscientists. Neuron 89, 683–694. https://doi.org/10.1016/j.neuron.2016.01.040

Roy, D.S., Kitamura, T., Okuyama, T., Ogawa, S.K., Sun, C., Obata, Y., Yoshiki, A., Tonegawa, S., 2017. Distinct Neural Circuits for the Formation and Retrieval of Episodic Memories. Cell 170, 1000-1012.e19. https://doi.org/10.1016/j.cell.2017.07.013

Sargolini, F., Fyhn, M., Hafting, T., McNaughton, B.L., Witter, M.P., Moser, M.-B., Moser, E.I., 2006. Conjunctive Representation of Position, Direction, and Velocity in Entorhinal Cortex. Science 312, 758–762. https://doi.org/10.1126/science.1125572

Sato, M., Mizuta, K., Islam, T., Kawano, M., Sekine, Y., Takekawa, T., Gomez-Dominguez, D., Schmidt, A., Wolf, F., Kim, K., Yamakawa, H., Ohkura, M., Lee, M.G., Fukai, T., Nakai, J., Hayashi, Y., 2020. Distinct Mechanisms of Over-Representation of Landmarks and Rewards in the Hippocampus. Cell Rep. 32, 107864. https://doi.org/10.1016/j.celrep.2020.107864

Scharfman, H.E., 2007. The CA3 “backprojection” to the dentate gyrus, in: Progress in Brain Research. Elsevier, pp. 627–637. https://doi.org/10.1016/S0079-6123(07)63034-9

Schlesiger, M.I., Cannova, C.C., Boublil, B.L., Hales, J.B., Mankin, E.A., Brandon, M.P., Leutgeb, J.K., Leibold, C., Leutgeb, S., 2015. The medial entorhinal cortex is necessary for temporal organization of hippocampal neuronal activity. Nat. Neurosci. 18, 1123–1132. https://doi.org/10.1038/nn.4056

Seabold, S., Perktold, J., 2010. Statsmodels: Econometric and Statistical Modeling with Python. Presented at the Python in Science Conference, Austin, Texas, pp. 92–96. https://doi.org/10.25080/Majora-92bf1922-011

Shan, K.Q., Lubenov, E.V., Papadopoulou, M., Siapas, A.G., 2016. Spatial tuning and brain state account for dorsal hippocampal CA1 activity in a non-spatial learning task. eLife 5, e14321. https://doi.org/10.7554/eLife.14321

Sharif, F., Tayebi, B., Buzsáki, G., Royer, S., Fernandez-Ruiz, A., 2021. Subcircuits of Deep and Superficial CA1 Place Cells Support Efficient Spatial Coding across Heterogeneous Environments. Neuron 109, 363-376.e6. https://doi.org/10.1016/j.neuron.2020.10.034

Sharp, P., 2006. Subicular place cells generate the same “map” for different environments: Comparison with hippocampal cells. Behav. Brain Res. 174, 206–214. https://doi.org/10.1016/j.bbr.2006.05.034

Sharp, P., Green, C., 1994. Spatial correlates of firing patterns of single cells in the subiculum of the freely moving rat. J. Neurosci. 14, 2339–2356. https://doi.org/10.1523/JNEUROSCI.14-04-02339.1994

Sharp, P.E., 1997. Subicular cells generate similar spatial firing patterns in two geometrically and visually distinctive environments: Comparison with hippocampal

place cells. Behav. Brain Res. 85, 71–92. https://doi.org/10.1016/S0166-4328(96)00165-9

Sheffield, M.E., Dombeck, D.A., 2019. Dendritic mechanisms of hippocampal place field formation. Curr. Opin. Neurobiol. 54, 1–11. https://doi.org/10.1016/j.conb.2018.07.004

Shepherd, G.M., Marenco, L., Hines, M.L., Migliore, M., McDougal, R.A., Carnevale, N.T., Newton, A.J.H., Surles-Zeigler, M., Ascoli, G.A., 2019. Neuron Names: A Gene- and Property-Based Name Format, With Special Reference to Cortical Neurons. Front. Neuroanat. 13, 25. https://doi.org/10.3389/fnana.2019.00025

Skaggs, W.E., McNaughton, B.L., Gothard, K.M., 1993. An Information-Theoretic Approach to Deciphering the Hippocampal Code.

Solstad, T., Boccara, C.N., Kropff, E., Moser, M.-B., Moser, E.I., 2008. Representation of Geometric Borders in the Entorhinal Cortex. Science 322, 1865–1868. https://doi.org/10.1126/science.1166466

Soriano, E., Martinez, A., Fariñas, I., Frotscher, M., 1993. Chandelier cells in the hippocampal formation of the rat: The entorhinal area and subicular complex. J. Comp. Neurol. 337, 151–167. https://doi.org/10.1002/cne.903370110

Sosulina, L., Graebenitz, S., Pape, H.-C., 2010. GABAergic Interneurons in the Mouse Lateral Amygdala: A Classification Study. J. Neurophysiol. 104, 617–626. https://doi.org/10.1152/jn.00207.2010

Sosulina, L., Meis, S., Seifert, G., Steinhäuser, C., Pape, H.-C., 2006. Classification of projection neurons and interneurons in the rat lateral amygdala based upon cluster analysis. Mol. Cell. Neurosci. 33, 57–67. https://doi.org/10.1016/j.mcn.2006.06.005

Spruston, N., 2008. Pyramidal neurons: dendritic structure and synaptic integration. Nat. Rev. Neurosci. 9, 206–221. https://doi.org/10.1038/nrn2286

Spruston, N., Jaffe, D.B., Johnston, D., 1994. Dendritic attenuation of synaptic potentials and currents: the role of passive membrane properties. Trends Neurosci. 17, 161–166. https://doi.org/10.1016/0166-2236(94)90094-9

Spruston, N., Schiller, Y., Stuart, G., Sakmann, B., 1995. Activity-Dependent Action

Potential Invasion and Calcium Influx into Hippocampal CA1 Dendrites. Science 268, 297–300. https://doi.org/10.1126/science.7716524

Stachniak, T.J., Ghosh, A., Sternson, S.M., 2014. Chemogenetic Synaptic Silencing of Neural Circuits Localizes a Hypothalamus→Midbrain Pathway for Feeding Behavior. Neuron 82, 797–808. https://doi.org/10.1016/j.neuron.2014.04.008

Stafstrom, C.E., 2005. The Role of the Subiculum in Epilepsy and Epileptogenesis. Epilepsy Curr. 5, 121–129. https://doi.org/10.1111/j.1535-7511.2005.00049.x

Strange, B.A., Witter, M.P., Lein, E.S., Moser, E.I., 2014. Functional organization of the hippocampal longitudinal axis. Nat. Rev. Neurosci. 15, 655–669. https://doi.org/10.1038/nrn3785

Stuart, G.J., Spruston, N., 2015. Dendritic integration: 60 years of progress. Nat. Neurosci. 18, 1713–1721. https://doi.org/10.1038/nn.4157

Sun, Y., Nguyen, A.Q., Nguyen, J.P., Le, L., Saur, D., Choi, J., Callaway, E.M., Xu, X., 2014. Cell-Type-Specific Circuit Connectivity of Hippocampal CA1 Revealed through Cre-Dependent Rabies Tracing. Cell Rep. 7, 269–280. https://doi.org/10.1016/j.celrep.2014.02.030

Takahashi, H., Magee, J.C., 2009. Pathway Interactions and Synaptic Plasticity in the Dendritic Tuft Regions of CA1 Pyramidal Neurons. Neuron 62, 102–111. https://doi.org/10.1016/j.neuron.2009.03.007

Tan, A.Y.Y., Zhang, L.I., Merzenich, M.M., Schreiner, C.E., 2004. Tone-Evoked Excitatory and Inhibitory Synaptic Conductances of Primary Auditory Cortex Neurons. J. Neurophysiol. 92, 630–643. https://doi.org/10.1152/jn.01020.2003

Tasic, B., Yao, Z., Graybuck, L.T., Smith, K.A., Nguyen, T.N., Bertagnolli, D., Goldy, J., Garren, E., Economo, M.N., Viswanathan, S., Penn, O., Bakken, T., Menon, V., Miller, J., Fong, O., Hirokawa, K.E., Lathia, K., Rimorin, C., Tieu, M., Larsen, R., Casper, T., Barkan, E., Kroll, M., Parry, S., Shapovalova, N.V., Hirschstein, D., Pendergraft, J., Sullivan, H.A., Kim, T.K., Szafer, A., Dee, N., Groblewski, P., Wickersham, I., Cetin, A., Harris, J.A., Levi, B.P., Sunkin, S.M., Madisen, L., Daigle, T.L., Looger, L., Bernard, A., Phillips, J., Lein, E., Hawrylycz, M., Svoboda, K., Jones, A.R., Koch, C., Zeng, H., 2018. Shared and distinct transcriptomic cell

types across neocortical areas. Nature 563, 72–78. https://doi.org/10.1038/s41586-018-0654-5

Taube, J., 1995. Head direction cells recorded in the anterior thalamic nuclei of freely moving rats. J. Neurosci. 15, 70–86. https://doi.org/10.1523/JNEUROSCI.15-01-00070.1995

Taube, JeffreyS., 1993. Electrophysiological properties of neurons in the rat subiculum in vitro. Exp. Brain Res. 96. https://doi.org/10.1007/BF00227110

Taxidis, J., Pnevmatikakis, E.A., Dorian, C.C., Mylavarapu, A.L., Arora, J.S., Samadian, K.D., Hoffberg, E.A., Golshani, P., 2020. Differential Emergence and Stability of Sensory and Temporal Representations in Context-Specific Hippocampal Sequences. Neuron 108, 984-998.e9. https://doi.org/10.1016/j.neuron.2020.08.028

Tran-Van-Minh, A., Cazé, R.D., Abrahamsson, T., Cathala, L., Gutkin, B.S., DiGregorio, D.A., 2015. Contribution of sublinear and supralinear dendritic integration to neuronal computations. Front. Cell. Neurosci. 9. https://doi.org/10.3389/fncel.2015.00067

Tsay, D., Dudman, J.T., Siegelbaum, S.A., 2007. HCN1 Channels Constrain Synaptically Evoked Ca2+ Spikes in Distal Dendrites of CA1 Pyramidal Neurons. Neuron 56, 1076–1089. https://doi.org/10.1016/j.neuron.2007.11.015

Unal, G., Joshi, A., Viney, T.J., Kis, V., Somogyi, P., 2015. Synaptic Targets of Medial Septal Projections in the Hippocampus and Extrahippocampal Cortices of the Mouse. J. Neurosci. 35, 15812–15826. https://doi.org/10.1523/JNEUROSCI.2639-15.2015

Valerio, S., Taube, J.S., 2012. Path integration: how the head direction signal maintains and corrects spatial orientation. Nat. Neurosci. 15, 1445–1453. https://doi.org/10.1038/nn.3215

Vallat, R., 2018. Pingouin: statistics in Python. J. Open Source Softw. 3, 1026. https://doi.org/10.21105/joss.01026

Van Cauter, T., Poucet, B., Save, E., 2008. Unstable CA1 place cell representation in rats with entorhinal cortex lesions. Eur. J. Neurosci. 27, 1933–1946.

https://doi.org/10.1111/j.1460-9568.2008.06158.x

Van Welie, I., Remme, M.W.H., Van Hooft, J.A., Wadman, W.J., 2006. Different levels of I_h determine distinct temporal integration in bursting and regular-spiking neurons in rat subiculum: Role of I_h in synaptic integration in subiculum. J. Physiol. 576, 203–214. https://doi.org/10.1113/jphysiol.2006.113944

Vandrey, B., Duncan, S., Ainge, J.A., 2021. Object and object-memory representations across the proximodistal axis of CA1. Hippocampus 31, 881–896. https://doi.org/10.1002/hipo.23331

Vardy, E., Robinson, J.E., Li, C., Olsen, R.H.J., DiBerto, J.F., Giguere, P.M., Sassano, F.M., Huang, X.-P., Zhu, H., Urban, D.J., White, K.L., Rittiner, J.E., Crowley, N.A., Pleil, K.E., Mazzone, C.M., Mosier, P.D., Song, J., Kash, T.L., Malanga, C.J., Krashes, M.J., Roth, B.L., 2015. A New DREADD Facilitates the Multiplexed Chemogenetic Interrogation of Behavior. Neuron 86, 936–946. https://doi.org/10.1016/j.neuron.2015.03.065

Wiegert, J.S., Mahn, M., Prigge, M., Printz, Y., Yizhar, O., 2017. Silencing Neurons: Tools, Applications, and Experimental Constraints. Neuron 95, 504–529. https://doi.org/10.1016/j.neuron.2017.06.050

Williams, S.R., 2004. Spatial compartmentalization and functional impact of conductance in pyramidal neurons. Nat. Neurosci. 7, 961–967. https://doi.org/10.1038/nn1305

Williams, S.R., Mitchell, S.J., 2008. Direct measurement of somatic voltage clamp errors in central neurons. Nat. Neurosci. 11, 790–798. https://doi.org/10.1038/nn.2137

Williams, S.R., Stuart, G.J., 2002. Dependence of EPSP Efficacy on Synapse Location in Neocortical Pyramidal Neurons. Science 295, 1907–1910. https://doi.org/10.1126/science.1067903

Witter, M., 2006. Connections of the subiculum of the rat: Topography in relation to columnar and laminar organization. Behav. Brain Res. 174, 251–264. https://doi.org/10.1016/j.bbr.2006.06.022

Witter, M.P., Amaral, D.G., 2004. Hippocampal Formation, in: The Rat Nervous System.

Elsevier, pp. 635–704. https://doi.org/10.1016/B978-012547638-6/50022-5

Witter, M.P., Griffioen, A.W., Jorritsma-Byham, B., Krijnen, J.L.M., 1988. Entorhinal projections to the hippocampal CA1 region in the rat: An underestimated pathway. Neurosci. Lett. 85, 193–198. https://doi.org/10.1016/0304-3940(88)90350-3

Witter, M.P., Groenewegen, H.J., 1990. Chapter 4 The subiculum: cytoarchitectonically a simple structure, but hodologically complex, in: Progress in Brain Research. Elsevier, pp. 47–58. https://doi.org/10.1016/S0079-6123(08)61240-6

Witter, M.P., Naber, P.A., van Haeften, T., Machielsen, W.C.M., Rombouts, S.A.R.B., Barkhof, F., Scheltens, P., Lopes da Silva, F.H., 2000. Cortico-hippocampal communication by way of parallel parahippocampal-subicular pathways. Hippocampus 10, 398–410. https://doi.org/10.1002/1098-1063(2000)10:4<398::AID-HIPO6>3.0.CO;2-K

Wouterlood, F.G., Saldana, E., Witter, M.P., 1990. Projection from the nucleus reuniens thalami to the hippocampal region: Light and electron microscopic tracing study in the rat with the anterograde tracer *Phaseolus vulgaris* -leucoagglutinin. J. Comp. Neurol. 296, 179–203. https://doi.org/10.1002/cne.902960202

Wozny, C., Beed, P., Nitzan, N., Pössnecker, Y., Rost, B.R., Schmitz, D., 2018. VGLUT2 Functions as a Differential Marker for Hippocampal Output Neurons. Front. Cell. Neurosci. 12, 337. https://doi.org/10.3389/fncel.2018.00337

Wozny, C., Maier, N., Schmitz, D., Behr, J., 2008. Two different forms of long-term potentiation at CA1-subiculum synapses: Target-cell specific LTP. J. Physiol. 586, 2725–2734. https://doi.org/10.1113/jphysiol.2007.149203

Wright, N.F., Erichsen, J.T., Vann, S.D., O'Mara, S.M., Aggleton, J.P., 2010. Parallel but separate inputs from limbic cortices to the mammillary bodies and anterior thalamic nuclei in the rat. J. Comp. Neurol. 518, 2334–2354. https://doi.org/10.1002/cne.22336

Yamawaki, N., Li, X., Lambot, L., Ren, L.Y., Radulovic, J., Shepherd, G.M.G., 2019. Long-range inhibitory intersection of a retrosplenial thalamocortical circuit by apical tuft-targeting CA1 neurons. Nat. Neurosci. 22, 618–626. https://doi.org/10.1038/s41593-019-0355-x

Ye, X., Kapeller-Libermann, D., Travaglia, A., Inda, M.C., Alberini, C.M., 2017. Direct dorsal hippocampal–prelimbic cortex connections strengthen fear memories. Nat. Neurosci. 20, 52–61. https://doi.org/10.1038/nn.4443

Yuste, R., Hawrylycz, M., Aalling, N., Aguilar-Valles, A., Arendt, D., Armañanzas, R., Ascoli, G.A., Bielza, C., Bokharaie, V., Bergmann, T.B., Bystron, I., Capogna, M., Chang, Y., Clemens, A., de Kock, C.P.J., DeFelipe, J., Dos Santos, S.E., Dunville, K., Feldmeyer, D., Fiáth, R., Fishell, G.J., Foggetti, A., Gao, X., Ghaderi, P., Goriounova, N.A., Güntürkün, O., Hagihara, K., Hall, V.J., Helmstaedter, M., Herculano-Houzel, S., Hilscher, M.M., Hirase, H., Hjerling-Leffler, J., Hodge, R., Huang, J., Huda, R., Khodosevich, K., Kiehn, O., Koch, H., Kuebler, E.S., Kühnemund, M., Larrañaga, P., Lelieveldt, B., Louth, E.L., Lui, J.H., Mansvelder, H.D., Marin, O., Martinez-Trujillo, J., Chameh, H.M., Mohapatra, A.N., Munguba, H., Nedergaard, M., Němec, P., Ofer, N., Pfisterer, U.G., Pontes, S., Redmond, W., Rossier, J., Sanes, J.R., Scheuermann, R.H., Serrano-Saiz, E., Staiger, J.F., Somogyi, P., Tamás, G., Tolias, A.S., Tosches, M.A., García, M.T., Wozny, C., Wuttke, T.V., Liu, Y., Yuan, J., Zeng, H., Lein, E., 2020. A community-based transcriptomics classification and nomenclature of neocortical cell types. Nat. Neurosci. 23, 1456–1468. https://doi.org/10.1038/s41593-020-0685-8

Zeisel, A., Muñoz-Manchado, A.B., Codeluppi, S., Lönnerberg, P., La Manno, G., Juréus, A., Marques, S., Munguba, H., He, L., Betsholtz, C., Rolny, C., Castelo-Branco, G., Hjerling-Leffler, J., Linnarsson, S., 2015. Cell types in the mouse cortex and hippocampus revealed by single-cell RNA-seq. Science 347, 1138–1142. https://doi.org/10.1126/science.aaa1934

Zeng, H., Sanes, J.R., 2017. Neuronal cell-type classification: challenges, opportunities and the path forward. Nat. Rev. Neurosci. 18, 530–546. https://doi.org/10.1038/nrn.2017.85

Zhang, F., Aravanis, A.M., Adamantidis, A., De Lecea, L., Deisseroth, K., 2007. Circuit-breakers: optical technologies for probing neural signals and systems. Nat. Rev. Neurosci. 8, 577–581. https://doi.org/10.1038/nrn2192

Acknowledgement

I am grateful to my advisor Professor Dr. Stefan Remy for providing me with the opportunity to work in his lab. Professor Remy was always available to help me with any issues or questions I had regarding my research. He allowed me to complete this thesis independently while providing guidance when necessary.

I would also like to express my appreciation to my thesis committee. I am grateful to Prof. Dr. Fuhrmann and Prof. Dr. Witke for their insightful comments and encouragement.

I thank my present and former colleagues from the AG Remy and the AG Fuhrmann at the DZNE / Cellular Neuroscience Group at the LIN for their friendship, support, and for creating a wonderful working environment. I would like to extend special thanks to my fellow labmates, particularly Dr. Hiroshi Kaneko, Dr. Liudmula Sosulina, Dr. Oliver Barnstedt, Dr. Rüdiger Geiß, Dr. Falko Fuhrmann and Dr. Petra Mocellin who assisted me greatly in preparing this dissertation.

Last but not least, my biggest thanks go to my family, my wife and our daughter, and to my parents, for their unwavering support, patience, understanding and always having my back.